NORTHWESTERN UNIVERSITY

Transport Processes at the Sediment-Water Interface

A DISSERTATION

SUBMITTED TO THE GRADUATE SCHOOL
IN PARTIAL FULFILLMENT OF THE REQUIREMENTS

for the degree

DOCTOR OF PHILOSOPHY

Field of Civil and Environmental Engineering

by

Kevin R. Roche

EVANSTON, ILLINOIS

September 2017

ABSTRACT

Rivers and streams are the corridors of material transport from land to sea. Solutes and particles experience a range of environments as they traverse the river network, many of which are highly reactive, and reaction rates are localized to specific regions. The interfacial region between the river and its underlying sediments, or the hyporheic zone, is particularly reactive due to the diversity of chemical environments and the abundance of life in stream sediments.

The overall transformation of reactive materials in streams and rivers is therefore closely linked to their transport to, and retention within, the hyporheic zone. However, hyporheic transport processes are difficult to elucidate because stream and rivers are highly heterogeneous. Transport mechanisms are not only active over a broad range of spatial and temporal scales in these systems, but they also co-vary. To accurately predict material movement in this environment, transport models must capture the full distribution of scales over which these processes are active, as well as the coupling between them. Such an effort requires detailed observations of the mechanisms that dominate hyporheic transport, many of which are difficult to measure within sediments.

This dissertation is motivated by the need for parsimonious, mechanistic models describing solute and particle transport at the sediment-water interface. To this end, we combine experiments and modeling to advance understanding of several transport processes that have not been observed or incorporated into current modeling frameworks. Specifically, we study the role of turbulence in regulating hyporheic transport in coarse-grained streambeds (Chapters 2-3), the

controls of microbial biomass on fine particle transport (Chapter 4), and the reworking of interfacial sediments by the aquatic worm *Lumbriculus variegatus* (Chapter 5). Together, our findings advance understanding of interfacial solute and fine particle transport by providing novel observations of several physical processes that regulate interfacial dynamics, as well as strategies for how these processes can be incorporated into multi-scale transport modeling frameworks.

Acknowledgements

The waypoints on my long path to, and through, graduate school were pointed out by more than I can name here. I am grateful to have such a diverse group of individuals who have collectively shaped my experience at Northwestern. Thanks to Darryl Carstensen and Kristin Wegner for communicating your passion for the environment and showing me that it can translate into a profession. Drs. Joseph Franses, Joseph Helble, Hugh Hillhouse, and Antonio Tillis saw a curiosity in me before I saw it in myself, and I am grateful for our early conversations that eventually drew me back to academia. I'm particularly indebted to Dr. Helble, whose sustained mentorship has guided me at many critical junctures of my career.

To my parents, Beth and Ken Roche, whose constant encouragement and support allow me to continually push my limits. To Becky, who has repeatedly shown me how to approach life with energy and passion. To Pete, Chris, and Nik, for our many conversations and chess games that served as enriching distractions. To Hannah, for your endless support, and for showing me that the pursuit of a cohesive community is as integral to a healthy world as the pursuit of clean waters.

Drs. Antoine Aubeneau, Jennifer Drummond, and Minwei Xie were invaluable graduate mentors that showed me the ropes during my early days in the Packman Lab. I'm proud to call you present and future colleagues. Conversations, constructive criticism and advice are truly appreciated from many more members of the group, including Jon Dallman, Liliana Hernandez, Angang, Li, Xiaobao Li, Nanxi Lv, Colin Phillips, Antonio Preziosi Ribero, and Vivien Rivera.

Lastly, I am deeply grateful for the mentorship of my advisor, Dr. Aaron Packman. Your skill in forging new connections, your unwavering optimism, and your kindness have helped me grow as a researcher and as a person. My graduate experience in your lab has been a true pleasure.

Table of Contents

List of Figures

List of Tables

We don't know what's going on here. If these tremendous events are random combinations of matter run amok, the yield of millions of monkeys at millions of typewriters, then what is it in us, hammered out of those same typewriters, that they ignite? We don't know. Our life is a faint tracing on the surface of mystery, like the idle, curved tunnels of leaf miners on the face of a leaf. We must somehow take a wider view, look at the whole landscape, really see it, and describe what's going on here. Then we can at least wail the right question into the swaddling band of darkness, or, if it comes to that, choir the proper praise.

from *Pilgrim at Tinker Creek*

Annie Dillard

CHAPTER 1

Introduction

Stream and river networks touch nearly all parts of continental landscapes, motivating

scientists to quantify the intimate hydrologic connectedness between land and sea. The slow

action of water balances tectonic uplift by chemically weakening and then eroding the surface of

mountains [*Leopold et al.*, 1964]. These eroded sediments join other solutes and organic matter

as they move through a network of inland waters that eventually exit to the oceans [*Anderson

and Anderson*, 2010].
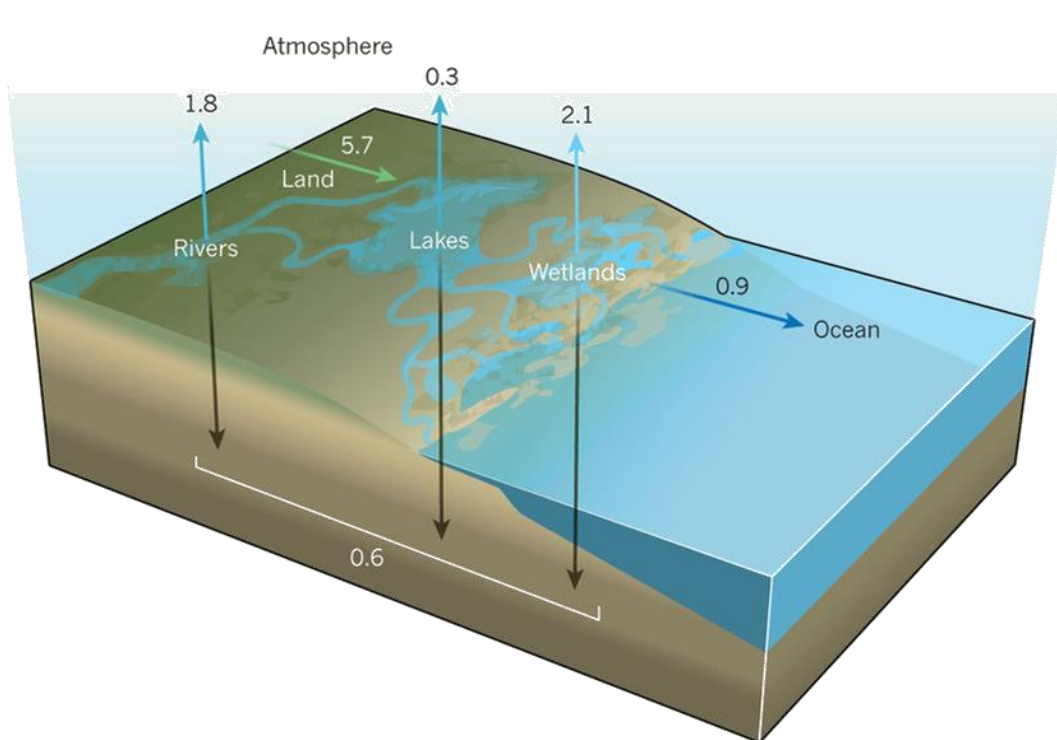
Figure 1.1. Contemporary estimates of global organic carbon fluxes (in Pg) to and from inland waters. Green arrow represents influx of terrestrial organic carbon into these waters. Figure from *Wehrli* [2013], with values provided from *Battin et al.* [2009], *Aufdenkampe et al.* [2011], and *Raymond et al.* [2013].

Materials in rivers and streams pass through a wide range of physical and chemical

environments that can result in their transformation or sequestration. For example, recent

continental-scale datasets of carbon fluxes show that only about 1/6th of terrestrially-derived

organic carbon that enters inland waters ultimately reaches the oceans (0.9 Pg of 5.7 Pg, Figure

1.1), and as much as 70% of these inputs exit as greenhouse gases within river networks [*Battin*

et al., 2009; *Aufdenkampe et al.*, 2011; *Bastviken et al.*, 2011; *Raymond et al.*, 2013; *Wehrli*,

2013]. Transformations occur for a wide range of reactive constituents, many of which can

adversely impact water quality both locally and downstream of their release [*Diaz and*

Rosenberg, 2008; *Rockstrom et al.*, 2009; *Carpenter et al.*, 2011; *Meter et al.*, 2016]. An

understanding of how rivers and streams function is therefore an essential step for predicting the

fate of reactive materials that enter them.

1.1 Hyporheic exchange across the sediment-water interface

Material transformation is highly localized in freshwater systems [*McClain et al.*, 2003], with

a large fraction of reactions occurring near the boundary between rivers and their underlying

sediments, called the sediment-water interface (SWI). The zone at the SWI, commonly termed

the benthic zone, is exposed to faster-flowing, well-mixed water in the stream. Just below the

SWI is a region where stream and groundwaters interact regularly, called the hyporheic zone

(Figure 1.3).
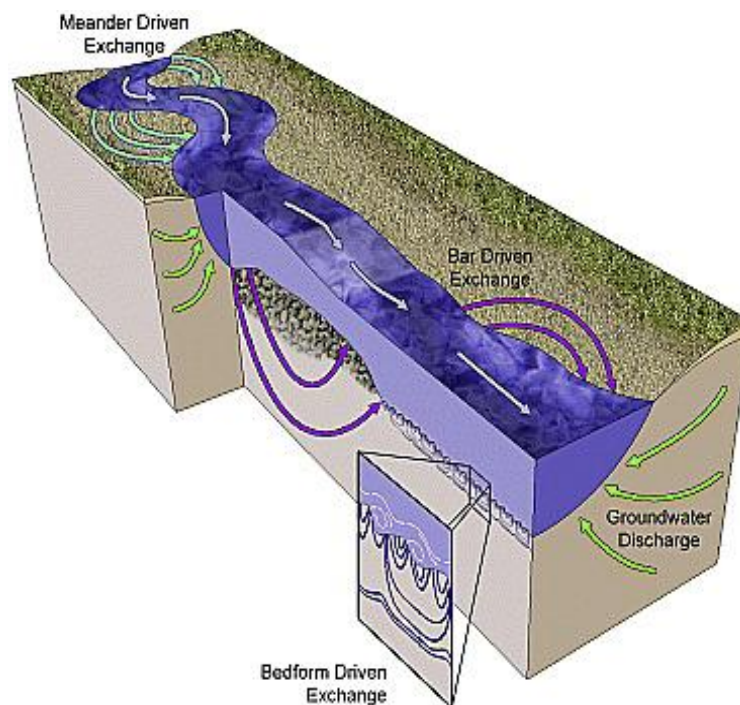
Figure 1.2. Schematic illustration of surface-subsurface interactions in a river. The benthic zone represents the region between a river's water column and underlying sediments, i.e., the sediment-water interface. Interactions between surface waters and groundwaters are defined as hyporheic exchange, and the region where these interactions occur regularly is called the hyporheic zone. Interactions exist over a broad range of scales. Figure from *Stonedahl et al.* [2010].

Higher transformation rates in the benthic and hyporheic zones can be attributed to both the abundance of life and the diversity of chemical environments found within them [*Jones and Mulholland*, 1999]. Sequestration and transformation of abiotic materials, such as stream-borne contaminants is favored in the hyporheic zone due to several factors: a transition from oxic to suboxic and anoxic conditions; sorption to sediments; and mixing with groundwater, which is chemically distinct from surface waters. Additionally, every square meter of streambed provides 100-1000 m^2 of habitable area for surface-attached microbial communities, a 'microbial skin'

that makes up the majority of microbial biomass in ecosystems [*Battin et al.*, 2016]. These

communities, called biofilms, drive chemical transformations as they metabolize organic carbon,

assimilate nutrients (e.g., ammonium, phosphate) and utilize multiple electron acceptors (e.g.,

oxygen, nitrate) [*Jones and Mulholland*, 1999; *Allan and Castillo*, 2007]. Thus, the SWI is

typically a region of high bioreactivity relative to the water column.
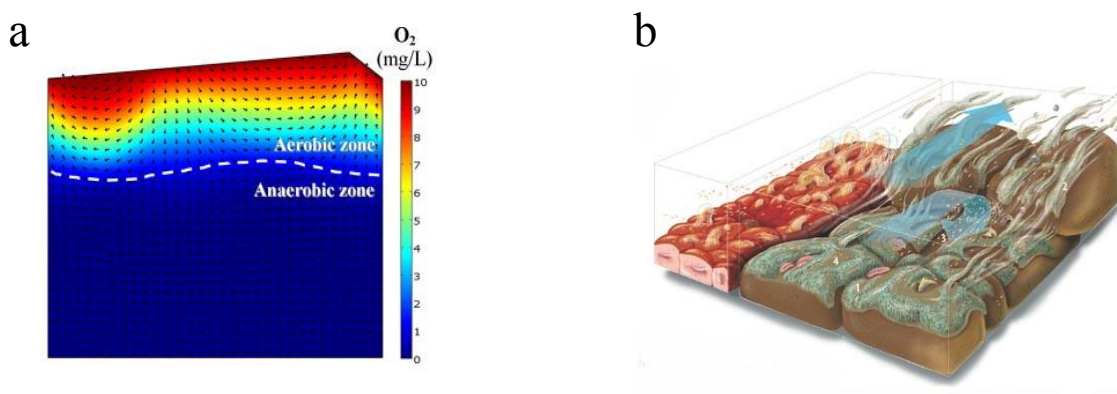
Figure 1.3. (a) Simulated hyporheic flow and oxygen concentration under a bedform [*Bardini et al.*, 2012b]. (b) Bacterial biofilms colonizing a lung epithelium (left) juxtaposed against a more complex benthic biofilm colonizing a sedimentary environment (right) [*Battin et al.*, 2007].

Delivery of reactive constituents (i.e., transport), as well as removal of reaction products, is

necessary for sustained reactivity at the SWI. Additionally, materials require adequate residence

time in reactive zones before they are transformed, and the balance between residence timescales

and reaction timescales exerts primary control of integrated transformation rates [*Zarnetske et al.*, 2011]. Water exchanged into the hyporheic zone experiences velocities many orders of

magnitude slower than in surface waters. These slow velocities often give rise to retention

timescales that are similar to or much greater than reaction timescales, favoring transformation in the hyporheic zone [*Harvey et al.*, 2013].

1.2 General challenges and approaches for predicting transformation at the SWI

Overall transformation rates in freshwater systems are commonly measured at larger scales, for example, by releasing a reactive tracer at into a stream and measuring its concentration (or its reaction products) some distance downstream [*Hauer and Lamberti*, 2011]. Such a study may accurately quantify transformation of a given reactive constituent in a given system under specific flow conditions. However, the high localization of reactions to the SWI makes it difficult to relate measured transformation rate to specific system conditions (e.g., mean stream velocity) [*Hall et al.*, 2002; *Boano et al.*, 2014]. Predictive assessments of transformation therefore require knowledge of how changing system conditions will alter transport to the benthic and hyporheic zones.

Laboratory experiments have proven extremely useful for understanding the physical drivers of hyporheic transport and reaction, thus elucidating the connection between observable properties (e.g., streamflow, bed permeability) and overall transformation. Experiments provide a controlled environment to study individual mechanisms that cannot be isolated in the field, as well as to use more sensitive instrumentation.

Because the processes at small-to-intermediate scales often dominate transformation in natural systems, any quantification of controlling mechanisms in the laboratory must be relatable to field conditions. We rely upon mathematical models to make this connection. Ideally, models should reasonably describe the mechanisms governing transport and reaction at the SWI, which is the definition for a physical or mechanistic model. Fidelity to controlling processes allows mechanistic models to be parameterized from measurable properties of the aquatic system (e.g., streambed porosity, permeability, roughness). As a result, mechanistic models are capable of predicting how the response variable will change as system properties change, either in the same system or in systems with different conditions. These models should also be parsimonious, meaning they describe the controlling process with as few parameters as possible.

Development of hyporheic exchange models is severely limited both by available technology and by the high complexity of processes near the SWI. These limitations are often addressed through semi-empirical models or scaling laws. For example, the first widely-adopted model for hyporheic exchange was the Transient Storage Model (TSM) [*Bencala and Walters*, 1983]. The TSM conceptualizes the hyporheic zone as a perfectly-mixed reservoir that uniformly exchanges mass with a stream. This representation is an obvious departure from the physics governing surface-subsurface transport in real systems because groundwaters are far from well mixed. Despite this departure, the TSM adequately captures many features of solute injection experiments observed in stream surface waters [*Harvey et al.*, 1996]. Nonetheless, the TSM's simple formulation severely limits its predictive capability. Model fits change with the timescale of stream measurements [*Zaramella et al.*, 2003], capture only a subset of all exchange processes

[*Haggerty et al.*, 2000], and cannot be transferred between streams. Most semi-empirical models suffer from similar predictive shortcomings as the TSM [*Boano et al.*, 2014]. A shift toward physically-based models is therefore essential if results from different stream conditions, or even observations in the same stream at different scales, are to be related.

Heterogeneity at the SWI also creates challenges for process interpretation. Interactions between the streambed and streamflow create static and dynamic variability at the SWI [*Packman and Brooks*, 2001; *Harvey et al.*, 2012; *M Xie et al.*, 2016]. This variability occurs at difficult-to-measure scales, as well as over across a broad range of distances and times [*Martin et al.*, 2012; *Zhang et al.*, 2012; *Aubeneau et al.*, 2015a]. For example, the permeability of hyporheic sediments can vary by as many as seven orders of magnitude in a single stream segment [*Fogg and Zhang*, 2016], and water traveling in the hyporheic zone will also experience velocities over this range of scales. How does one define a characteristic velocity in such a heterogeneous environment? A logical first step is to measure the mean displacement of a released tracer as it advects and spreads downstream. The mean velocity and other statistical properties (e.g., rate of spread) of the tracer are expected to change until all tracer mass has sampled all velocities present in the system, at which point they will transition to constant (characteristic) values [*Metzler and Klafter*, 2000; *Zhang and Meerschaert*, 2011]. The appropriate observation scale is therefore a time or distance beyond this transition. Unfortunately, measured subsurface velocity and other statistics often change over the entire observation period, meaning the appropriate measurement scale is larger than the system size [*Gelhar et al.*, 1992; *Aquino et al.*, 2015]. This poses a problem for biogeochemical models that

rely on a characteristic velocity to quantify the balance between reaction and transport timescales in subsurface sediments [*Zarnetske et al.*, 2011; *Harvey et al.*, 2013].

An additional criterion for aquatic transport models in natural systems is therefore needed: they must describe how transport processes vary over a broad range of scales. A new class of "multiscale" models has gained popularity in the last two decades, owing to their ability to parsimoniously describe scale dependency in earth surface processes [*Rodríguez-Iturbe and Rinaldo*, 2001; *Berkowitz et al.*, 2006; *Meysman et al.*, 2008a; *Schumer et al.*, 2009; *Foufoula-Georgiou and Stark*, 2010]. These models, based on stochastic representations of the underlying transport process, will be discussed further in the following section.

1.3 Specific transport mechanisms and knowledge gaps

1.3.1 Turbulent hyporheic exchange

Mass and heat are efficiently mixed within the stream water column by turbulence, but the role of turbulence in hyporheic transport remains unclear. The sharp transition from energetic surface flows to much slower subsurface flows is generally assumed to occur over a depth of only a few sediment grains [*Boudreau and Jorgensen*, 2001; *Tonina and Buffington*, 2007]. Recent studies have shown that microbial metabolism, substrate utilization, and habitat selection are all controlled by in-stream turbulence [*Cardinale et al.*, 2002; *Hondzo and Wang*, 2002; *Singer et al.*, 2010; *Niederdorfer et al.*, 2016]. Given the high bioactivity at the SWI [*Battin et al.*, 2016], these studies suggest that turbulence in the hyporheic zone plays an important role in stream ecology and biogeochemistry.

Most studies of hyporheic exchange apply the physically-based advective pumping model to predict solute concentrations observed in a stream's surface waters (Figure 1.4). This model is capable of predicting the hyporheic flow field from measurements of streamflow, sediment permeability, and streambed topography when subsurface flows are governed by Darcy's Law [*Elliott and Brooks*, 1997a; b; *Packman*, 1999]. A key performance metric for these models is their ability to predict in-stream solute concentrations at timescales slower than those related to in-stream mixing, since solute is retained in the hyporheic zone over a broad range of times. Recent laboratory experiments by *Marion et al.* [2008] and fieldwork by *Stonedahl et al.* [2012] showed that the model successfully described exchange at slow timescales ($\mathcal{O}(1\text{ h})$), but substantial deviations between model predictions and observations were observed at intermediate times. That is, retention timescales shorter than those induced by streambed topography and longer than those related to in-stream mixing were not captured by the pumping model. Two processes have been hypothesized to influence solute transport over these timescale: surface storage zones, created by flow obstructions, [*Ensign and Doyle*, 2005], benthic biomass [*Battin et al.*, 2003a; *Orr et al.*, 2009], and side pools [*Gooseff et al.*, 2005; *Jackson et al.*, 2013]; and rapid hyporheic exchange due to flow around individual sediment grains or grain clusters and turbulence penetrating into the hyporheic zone [*Nagaoka and Ohgaki*, 1990; *Packman et al.*, 2004; *Marion et al.*, 2008]. Parsing the contributions of these two zones is essential if nutrient dynamics at the scale of the river reach are to be predicted, due to the pronounced biological and chemical contrast of the surface and the subsurface [*Jones and Mulholland*, 1999].
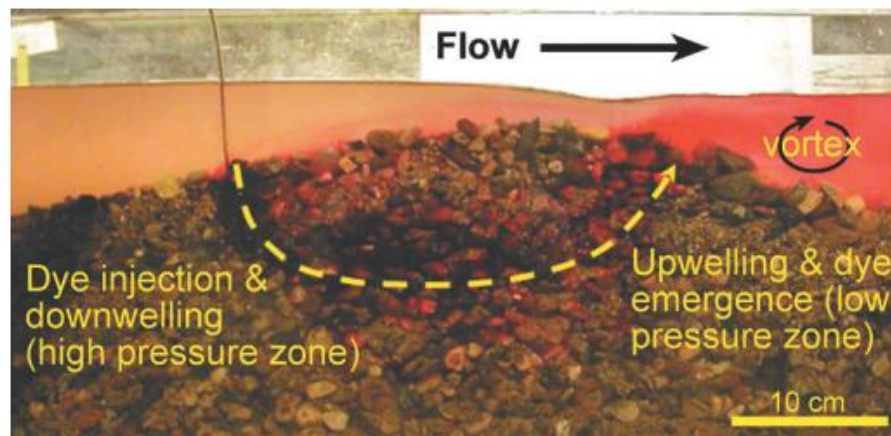
Figure 1.4. Top: Pathline of tracer migration through a dune-shaped gravel bedform. Topography-driven flows are well represented by the advective pumping model, but do not explain hyporheic solute retention over the full range of observed timescales. Short- to intermediate- timescale advection associated with streambed roughness and turbulent exchange are not captured by the advective pumping model Figure from *Tonina and Buffington* [2009].

Turbulent hyporheic exchange is expected to be more important and exert a greater influence over hyporheic transport in streams with coarser bed sediments. Measured hyporheic exchange rates for gravel- and cobble-bed streams can be orders of magnitude higher than can be explained by topography-induced advective flows or by molecular diffusion [*C P Richardson and Parr*, 1988; *Packman et al.*, 2004]. Empirical analyses show that these rates scale with bulk flow properties (e.g., Reynolds number) and with streambed properties (e.g., permeability) [*Packman et al.*, 2004; *O'Connor and Harvey*, 2008], suggesting a relationship between the turbulent flow field in the water column and streambed. Flow coupling between the surface and subsurface, particularly at high Reynolds numbers, causes substantial deviations in friction factors, stream velocities, and in-stream turbulence compared to equivalent impermeable beds [*Ruff and Gelhar*, 1972; *Zagni and Smith*, 1976; *Manes et al.*, 2009; *Blois et al.*, 2013]. These changes cannot be

explained by simply treating the stream simply driving Darcy flow in the underlying porous

medium, as is assumed by the pumping model, and instead suggests that streams with a highly

permeable substratum need to be analyzed as a flow continuum [*Manes et al.*, 2011].
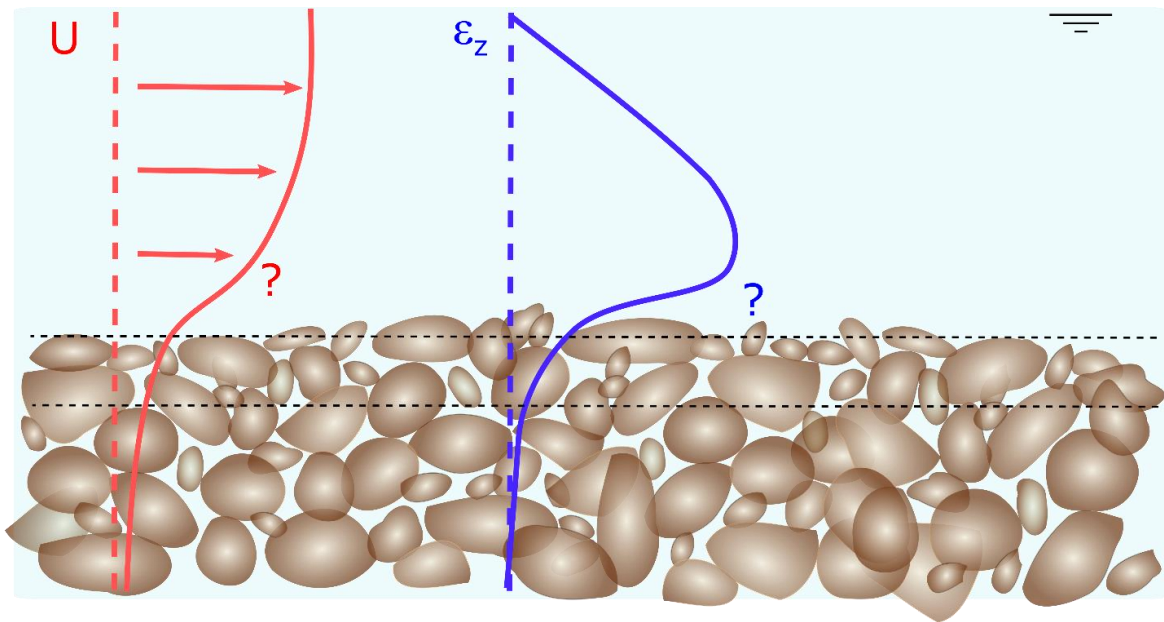
Figure 1.5. Conceptual profiles of velocity (red line) and vertical mixing (blue line) within a stream underlain by a coarse sediment bed. Dashed lines represent asymptotic values found deep within the bed. Figure adapted from *Manes, et al.* [2011].

A limited number of experimental studies show a direct correlation between streamflow and

mass transport below the SWI [*C P Richardson and Parr*, 1988; *Nagaoka and Ohgaki*, 1990;

Packman et al., 2004; *Chandler et al.*, 2016]. Unification of these experimental findings first

requires more detailed observations, below the SWI, at the spatial and temporal scales where

turbulence is expected to control mass transport.

1.3.2 Upscaled measures of turbulent hyporheic exchange

An important goal in fluvial transport research is the development of analytical models that

describe downstream mass transport. Reduced-order (1-D) equations successfully capture the

basic features of mass transport in rivers. For example, the classical advection-dispersion

equation (ADE) captures has been widely applied to predict bulk transport in rivers [*Elder*, 1959;

Fischer et al., 1979], but this model doesn't capture the long-term mass retention that is

generally seen in rivers (Figure 1.6).
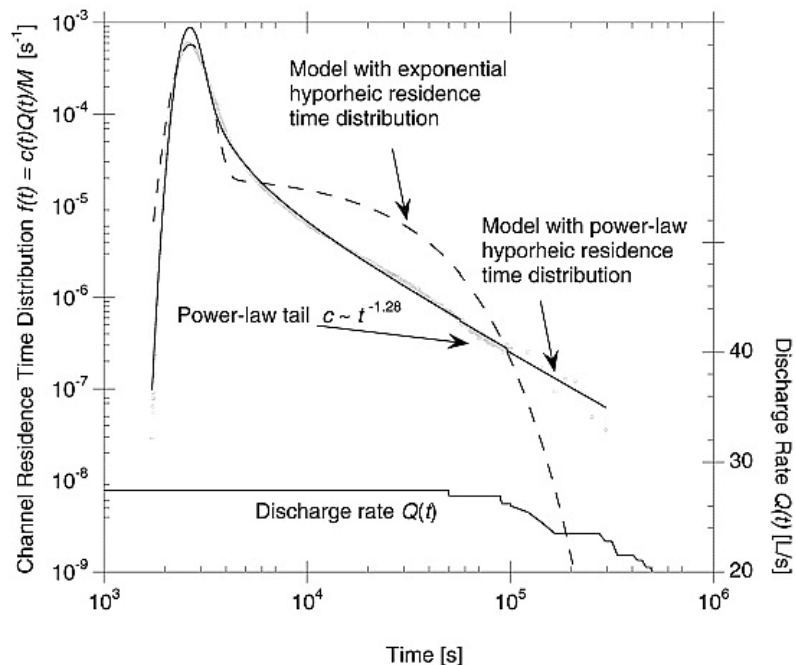
Figure 1.6. Fits of a transport model with a single storage zone with exponential residence
time distribution (dashed lien) and the multiscale, multirate mass transfer model (solid line) to
in-stream rhodamine concentrations. Figure from [*Haggerty et al.*, 2002].

Advancements in tracer sensitivity showed that the simple corrections to the ADE based on

solute storage, such as the transient storage model, do not faithfully represent all retention

timescales (see Section 1.2), spurring the continued development of 1-D multiscale (or

stochastic) models that describe the wide distribution of residence times associated with hyporheic mass transport [*Haggerty et al.*, 2002; *Schumer et al.*, 2003; *Boano et al.*, 2007]. Multiscale models account for solute retention in the hyporheic zone for anomalously long times. Anomalous transport refers to ensemble behavior that differs from basic Brownian motion diffusion, and thus is not described by the classical diffusion equation or ADE [*Berkowitz et al.*, 2006].) Such anomalous transport behavior is described by generalized stochastic transport models, such as the General Master Equation, Fokker-Planck Equation, and Continuous-Time Random Walks [*Metzler and Klafter*, 2000; *Meerschaert and Sikorskii*, 2012]. Analytical solutions for the stream-hyporheic transport problem exist when certain model constraints are imposed. Specifically, (1) motion can be described by a random variable with independent and identically distributed jumps, (2) there is sufficient separation of velocity scales between mobile (stream) and immobile (hyporheic) zones so that immobilized mass can be treated as motionless, (3) the distribution of jump lengths and wait times are independent, and (4) the jump and wait-time distributions are well-behaved, typically with the in-stream distribution described by a thin-tailed distribution (e.g., exponential) and the hyporheic wait-time distribution described by a heavy-tailed distribution (e.g., Pareto) [*Metzler and Klafter*, 2000; *Schumer et al.*, 2003]. Further, analytical solutions are generally only available for asymptotic ensemble behavior.

Streams with coarse, highly permeable sediment beds generally violate all three of these constraints. Porewater velocities immediately below the SWI generally have similar magnitude as the water column. Further, mixing rates decay sharply across the interface, causing highly solute motion to be highly correlated with location in the streambed. Finally, coherent turbulent

flow structures penetrate into the hyporheic zone [*Breugem et al.*, 2006; *Blois et al.*, 2012], generating correlated, spatially-dependent motions below the surface. It is therefore unclear if current multiscale models can be applied to coarse-bed, high-permeability streams.

1.3.3 Flow-biofilm interactions

Early studies of fluvial transport focused primarily on physical features of the stream, such as the flow field, bed roughness, and sediment permeability [*Elder*, 1959; *Fischer et al.*, 1979; *Newbold et al.*, 1981; *Bencala and Walters*, 1983; *Thibodeaux and Boyle*, 1987; *Elliott and Brooks*, 1997b]. Reactive-transport models for these systems generally parameterize physical and chemical processes independently, and thus that reactions do not alter material transport or system properties in any way [*Harvey and Fuller*, 1998; *Marzadri et al.*, 2011; *Bardini et al.*, 2012a]. However, biofilms change their physical environment as they grow.

Microbial metabolism depends on nutrient and carbon transport to regions of high microbial abundance, and microbial growth alters transport in these regions by covering sediment grains, thereby altering streambed roughness, filling pore space, and reducing streambed permeability [*Orr et al.*, 2009]. Biofilm growth above the SWI, on the order of 10 μm to 1 cm (Figure 1.3c), modulates turbulence intensity near the streambed [*Nikora et al.*, 2002; *Larned et al.*, 2011], creating a local environment that favors solute and particle retention [*Battin et al.*, 2003a; *Larned et al.*, 2004]. Biological growth therefore represents a feedback between transport and transformation of water-borne material at the SWI and within the hyporheic zone [*Biggs et al.*,

2005; *Marion et al.*, 2014]. However, few studies have directly related alterations in mass transport to biofilm growth or morphology.

1.3.4 Sediment mixing by bioturbation

Advective transport can be very slow in low-energy flows, such as in lakes and during low discharge summer months. Molecular diffusion is expected to be the controlling physical transport process in the absence of advective porewater flow. However, stream and lake sediments are rarely devoid of life, and macrofauna movements can result in rapid local mixing (biodiffusion), nonlocal transport due to burrowing and feeding at depth (conveyor feeding), and pumping of surface waters into and out of sediments [*Robbins et al.*, 1979; *Huettel and Gust*, 1992; *Boudreau and Jorgensen*, 2001; *Kristensen et al.*, 2012]. Models for transport in low-permeability sediments that do not include transport driven by macrofauna have been shown to severely underestimate surface-subsurface exchange [*Thibodeaux and Bierman*, 2003]. Densities of macrofauna can range from 10-100,000/m^2 [*Brinkhurst*, 1970; *Cook and Johnson*, 1974; *McCall and Tevesz*, 1982], and the movements of these organisms ultimately determine the rate at which solutes and sediments are mixed [*Meysman et al.*, 2006].
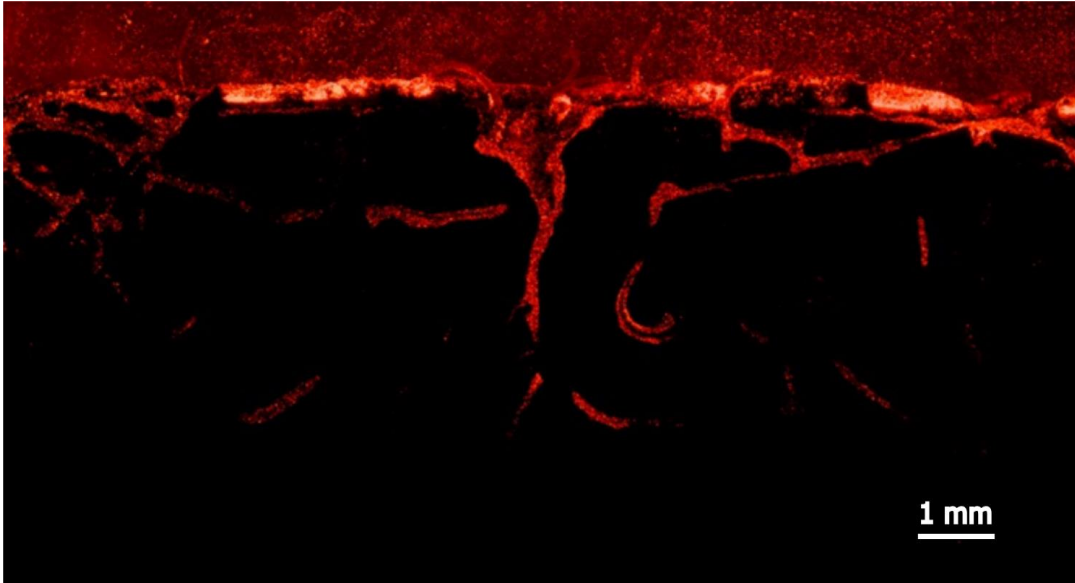
Figure 1.7. Burrow traces of the benthic oligochaete water worm *Lumbriculus variegatus*, illuminated by fluorescent tracer particles. Image is 14.0 mm W× 7.9 mm H [*Roche et al.*, 2016].

Various analytical models have been used to describe the multiple classes of organism behaviors [*Boudreau*, 2000]. By prescribing an assumed transport behavior that approximates one or several organism behaviors, models can provide reasonable fits to overall mixing patterns after calibration [*Boudreau*, 2000; *Meysman et al.*, 2010]. However, they generally use parameters that are not directly related to basic properties of the underlying mixing mechanism, such as the number of organisms present or descriptions of organism motion. Further, available analytical models are often only applicable in the asymptotic limit after a large number of transport events have occurred [*Meysman et al.*, 2008b]. Averaging times can be prohibitively long when bioturbation is heterogeneous [*Lick*, 2006]. This is likely the general case for most animals, given that their movements are episodic in nature [*François et al.*, 1997; *Klafter and Sokolov*, 2005; *Benhamou*, 2007; *Meysman et al.*, 2008b].

1.4 Objectives and scope

This dissertation is motivated by the need for parsimonious, mechanistic models describing solute and particle transport at the SWI. The mechanisms we study include both physical (i.e., hydrodynamics, Chapters 2-3) and biological (benthic biofilms, Chapter 4, and bioturbation, Chapter 5), reflecting the diversity of transport processes found in natural aquatic systems.

In Chapter 2 we present an experimental investigation of solute transport in a laboratory model of a stream with a coarse sediment bed (4 cm spheres) arranged in a regular geometry (simple cubic packing). The objectives of this study were to understand turbulent momentum and mass transport relate in the hyporheic zone. We used custom-built, high-frequency sensors to measure how subsurface concentrations vary with streambed depth and with flowrate, and related these observations of mass transport to velocity measurements (momentum transport).

We explore the upscaled implications of turbulent stream-subsurface flow coupling via a numerical particle tracking model in Chapter 3, with the goal of quantifying vertical mixing and downstream transport downstream transport and vertical mixing across the surface-subsurface continuum. We parameterize the model with two hypothesized profiles of vertical hyporheic mixing. Each profile is fit to steady-state injection results from Chapter 2, and the best fit models are then used to simulate a pulse injection for a stream with identical properties. Results from these upscaled simulations are used to understand what physical features of high-permeability streams influence breakthrough curve measurements.

We explore the linkage between biofilm growth and fine particle transport in Chapter 4. We simultaneously measured biofilm structure and fine particle dynamics in experimental streams mesocosms. We then fit a multiscale, stochastic mobile-immobile model to calculate particle immobilization rates and residence time distributions in the immobile zone from the in-stream concentration time-series. These fits were correlated against measures of biofilm structure to determine if specific biofilm features controlled fine particle deposition and retention.

Chapter 5 details an experimental and modeling study of bioturbation by the aquatic worm *Lumbriculus variegatus*. The objective of this analysis was to develop a model that directly relates sediment mixing to the underlying mechanisms of worm motion and burrow construction. We directly measured both burrow formation and the redistribution of a fluorescent sediment tracer using time-lapse photography. We then developed a random walk model that was directly parameterized from the observed burrowing statistics. Model results were evaluated using observed tracer particle redistribution to assess the model's ability to capture key features of mixing, and compared with fits from a simple advection-diffusion model to evaluate the appropriateness of simplifying assumptions commonly used in the field.

We summarize the overall findings and contribution of the dissertation and suggest future research directions in Chapter 6.

CHAPTER 2

Turbulence links momentum and solute exchange

in coarse-grained streambeds

ABSTRACT

The exchange of solutes between surface and porewaters is an important control over stream ecology and biogeochemistry in the hyporheic zone. Turbulence in the water column is known to enhance transport across the sediment-water interface (SWI). However, the link between turbulent momentum and solute transport within the hyporheic zone remains undetermined due to the lack of high-frequency *in situ* observations. Here, we relate turbulent momentum and solute transport using measurements within a streambed with 4-cm sediments. Velocities were measured using endoscopic particle imaging velocimetry and used to generate depth profiles of turbulence statistics. Solute transport was observed directly within the hyporheic zone using a custom-built microsensor array in the sediment bed. Injection experiments were used to assess both turbulent fluxes across the SWI and patterns of hyporheic mixing. Depth profiles of concentration fluctuations were compared with profiles of turbulence statistics, and profiles of mean concentration were compared to an effective dispersion model. Fluorescent visualization experiments at a stream Reynolds number of $Re = 27,000$ revealed the presence of large-scale motions that ejected tracer from porewaters. These events increased in frequency and intensity for $Re = 55,000$ but were not present at $Re = 13,000$. Turbulent shear stresses decayed greatly within the first grain diameter below the sediment-water interface for $Re = 22,000$ and $39,000$, and within two grain diameters for $Re = 75,000$. High frequency concentration fluctuations exhibited similar decay patterns as the turbulent shear stresses. Comparison with the dispersion model showed that hyporheic mixing was enhanced in regions where turbulent stresses occurred.

Together, these results show that penetration of turbulence directly controls both interfacial exchange and mixing within the hyporheic zone.

2.1 Introduction

Hyporheic exchange has long been recognized as a primary control of nutrient, carbon, and contaminant cycling in rivers and streams. Interactions between surface and hyporheic waters influence the fate of these reactive constituents by controlling their fluxes to, and residence times within, bioreactive regions of the hyporheic zone [*Jones and Mulholland*, 1999; *Lawrence et al.*, 2013; *Boano et al.*, 2014]. Assessment and prediction of overall stream function (e.g., net hyporheic metabolism, contaminant removal) therefore requires a proper description of the mechanisms governing hyporheic transport. Although physical models for hyporheic transport have advanced substantially over the past two decades, current physical models only capture transport associated with slower-moving viscous flows that are governed by Darcy's Law. They thus ignore faster exchange processes associated with fluid turbulence that can control hyporheic exchange in high permeability streambeds [*Nagaoka and Ohgaki*, 1990; *Shimizu et al.*, 1990; *Packman et al.*, 2004; *Chandler et al.*, 2016; *Voermans et al.*, 2017]. A motivating question for the current study is: where, and to what extent, does turbulent transport enhance hyporheic exchange?

Current physical models of hyporheic exchange are rooted in experimental observations of advective and dispersive transport in the subsurface [*Thibodeaux and Boyle*, 1987; *Huettel et al.*, 1996; *Bottacin-Busolin and Marion*, 2010; *Hester et al.*, 2017]. Advective transport is controlled

by a combination of energy gradients near the sediment-water interface (SWI), properties of stream sediments, and large-scale interactions with underlying aquifers [*Boano et al.*, 2014; *Fox et al.*, 2014]. Roughness elements such as surface-exposed grains, dunes, and riffles alter the near-streambed pressure field, and the resulting hydrodynamic forces drive water from high-pressure to low-pressure regions of the streambed. This process of "advective pumping" is well understood to regulate hyporheic fluxes and residence times [*Elliott and Brooks* [1997b; 1997a]; [*Cardenas*, 2015]. Turbulence is commonly assumed to influence such a thin region of the streambed that it can effectively be ignored [*Cardenas and Wilson*, 2007; *Tonina and Buffington*, 2009].

The advective pumping model predicts limited or no exchange in streambeds with very small topographic features. However, exchange rates in flat gravel beds have measured 2-4 orders of magnitude greater than those predicted by advective pumping or by basic diffusion [*Packman et al.*, 2004; *O'Connor and Harvey*, 2008], and experimental evidence suggests that turbulent velocity fluctuations are a primary driver of solute exchange [*Nagaoka and Ohgaki*, 1990]. In these instances, exchange is typically described using a dispersion model with an effective coefficient at the SWI, D_{eff}. This coefficient is determined from observations of net exchange between the water column and the streambed, based on changes in water column concentrations [*C P Richardson and Parr*, 1988; *Elliott and Brooks*, 1997a; *Packman et al.*, 2004; *O'Connor and Harvey*, 2008; *Grant et al.*, 2012]. However, it is unclear how interpretations of exchange are biased by this model choice when velocities and mixing rates vary spatially in the streambed.

Despite the absence of a mechanistic model, detailed experimental and numerical investigations of subsurface velocities have improved understanding of turbulent momentum transport within the hyporheic zone. A key finding is that both stream flow and bed permeability affect the flow structure through the entire surface-subsurface continuum [*Zagni and Smith*, 1976; *Manes et al.*, 2011; *Blois et al.*, 2013]. Flows over permeable sediment beds exhibit higher overall flow resistance, deviations from the canonical logarithmic turbulent velocity profile, and modified shapes and intensities of the turbulent kinetic energy (TKE) profile compared to flows over impermeable beds having similar boundary roughness [*Ruff and Gelhar*, 1972; *Zagni and Smith*, 1976; *Zippe and Graf*, 1983; *Breugem et al.*, 2006; *Manes et al.*, 2009; *Manes et al.*, 2011]. Further, turbulent eddies from the water column penetrate across the SWI, driving momentum below the interface [*Stoesser et al.*, 2007; *Blois et al.*, 2012]. Within the bed, momentum is dissipated by drag forces around bed sediment grains, resulting in rapid decreases in velocities, velocity fluctuations, and pressure fluctuations [*Vollmer et al.*, 2002; *Breugem et al.*, 2006]. Simulations and experiments suggest that these turbulent flow properties influence mass transport in the hyporheic zone, with velocity fluctuations inducing mixing in porewaters, and low-frequency pressure fluctuations inducing subsurface advection without appreciable mixing [*Packman et al.*, 2004; *Chandesris et al.*, 2013]. Studies of flows over sparse vegetation also suggest that transport is enhanced by larger-scale flow structures generated by shear instabilities at the SWI [*White and Nepf*, 2007; *Ghisalberti*, 2009].

A predictive understanding of turbulent solute exchange in coarse sediment beds is currently limited by a lack of high frequency observations in porewaters. Such observations are needed to

evaluate the specific flow features that control hyporheic transport. To address this need, we conducted two series of experiments in laboratory channels with a bed composed of coarse spheres, which were used to enable novel *in situ* observations of turbulent flow and solute transport. In the first set of experiments, the hyporheic flow field was measured directly within pores using an endoscopic flow visualization system. In the second set of experiments, tracer mixing was observed *in situ* using a custom-constructed sensor array. Experiments were conducted over a range of flows to assess momentum and mass transport with varying degrees of surface-subsurface flow coupling.

2.2 Methods

2.2.1 EPIV Experiments

Endoscopic particle imaging velocimetry (EPIV) was used to directly measure hyporheic porewater flow in the Ven Te Chow Hydrosystems Laboratory at the University of Illinois at Urbana-Champaign (Urbana, IL). Details of the EPIV experimental setup are provided in [*Blois et al.*, 2012]. In brief, experiments were conducted in a recirculating flume with a 4.8-m L × 0.35-m W × 0.6-m H test section. The test section was packed with 0.04-m spheres fixed in a simple cubic packing, creating a 0.24-m streambed that was 9 spheres wide and 6 spheres high. The water level was fixed at 0.16 m, and water was recirculated at three different discharge levels reported in Table 2.1.

The instantaneous flow field within the porespace was imaged with an endoscopic camera, which was illuminated by a laser endoscope that produced a thin light sheet centered in the high porosity plane of the pore throat. The experimental setup provided a 0.6-mm diameter circular field of view in the center of a pore throat that could image the 2-D flow field at 7 Hz frequency. Velocity time series were averaged over the entire 2-D field and decomposed into mean and fluctuating components using standard Reynolds decomposition [*Tennekes and Lumley*, 1972]:

$$u = \bar{u} + u'$$
$$w = \bar{w} + w'$$

(2.1)

where u is instantaneous longitudinal velocity decomposed into its mean $\bar{u}$ and fluctuating u' components, and w is instantaneous vertical velocity decomposed into its mean $\bar{w}$ and fluctuating w' components. The turbulent Reynolds stresses, $\overline{u'w'}$, and vertical stresses, $\overline{w'w'}$, are reported in this study. Time series are reported for measurements across a vertical column of pore throats over the streambed depth, at elevations of z = -0.04, -0.08, -0.12, -0.16, -0.20, and -0.24 m, where z = 0 represents the elevation of the SWI (top of uppermost sediment grains). The same setup was also used to measure velocities in the water column.

2.2.2 Solute transport experiments: Laboratory flume and sediment bed

Solute mixing experiments were conducted in a 2.5-m L × 0.2-m W × 0.5-m H recirculating flume in the Environmental and Biological Transport Processes Laboratory at Northwestern University. Water was recirculated from the downstream to the upstream end-well of the flume via a PVC pipe and pump. An in-line vortex-shedding flowmeter (Rosemont 8800) was used to measure the total flow rate. The flume slope was adjustable via a manual jack.

48

The sediment bed was constructed from PVC spheres (Figure 2.1). The bed consisted of a 1-m inlet section that was randomly packed with 3.8-cm and 6.4-cm spheres for flow conditioning, and a downstream test section filled with 3.8-cm spheres in a simple cubic packing (CP) array of 5 spheres W x 6 spheres H. The CP bed was constructed by stacking vertical columns of 6 spheres onto a threaded 0.32-cm diameter stainless steel rod. Each column was fixed to a 0.64 cm-acrylic sheet, which was installed as a false bottom in the flume. The array of spheres was fixed within the flume through insertion of two 0.64-cm thick acrylic sheets between the bed and the flume sidewalls to maintain tight cubic packing.

Results are in terms of distances normalized by the grain diameter (i.e., $L^* = L/3.8$ cm). Longitudinal distances x^* are reported relative to the solute injection location. Transverse distances are reported from the edge of the flume sidewall. $y^* = 2.5$ is the flume centerline. Depths are reported relative to the SWI, which is defined as the top of the first row of spheres comprising the bed, so that $z^* = -1$ at the bottom of the first layer of spheres.
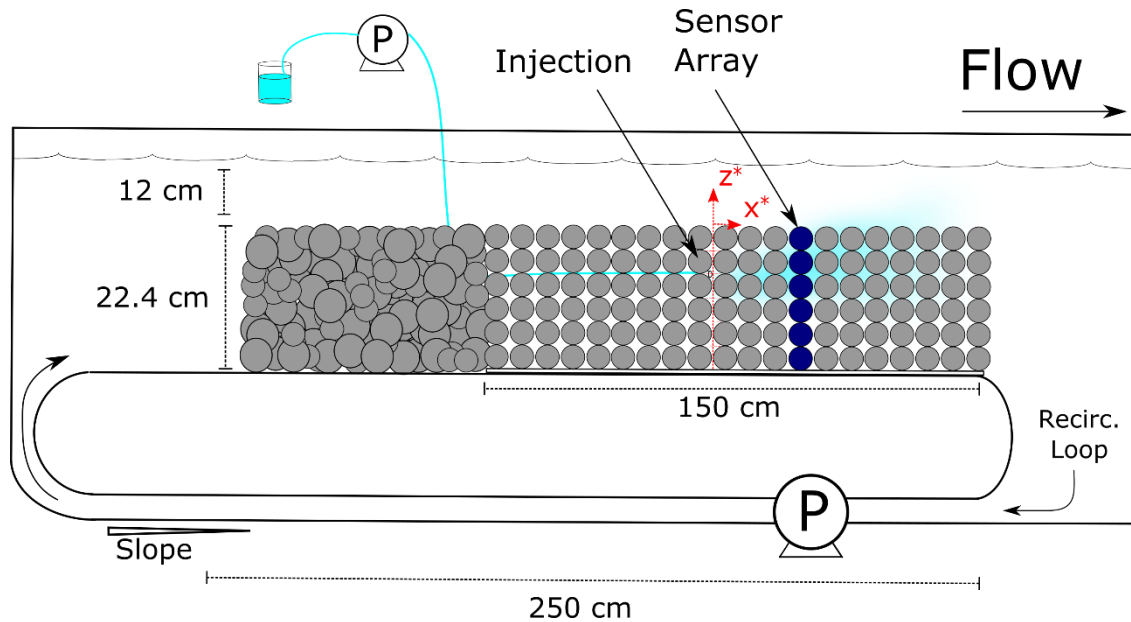
Figure 2.1. Schematic of recirculating flume with bed composed of a flow-condition region of randomly-packed spheres and a test section composed of a cubic-close-packed array of spheres.

2.2.3 Solute transport experiments: concentration microsensors

A cross-sectional array of grains in the test section was instrumented with high-frequency conductivity sensors for *in situ* observation of salt tracer concentrations. The sensors were 2.5-mm interdigitated electrodes (Synkera Technologies, Longmont, CO) with 25.4-μm spacing and gold conductors, wired into a resistor-capacitor-resistor integrated circuit. The small sensor size allowed pore waters to be sampled nearly at-a-point without significantly perturbing the porewater flow field. Sensors were surface-mounted onto the grains using high-resistivity epoxy. One sensor was implanted directly onto each of the 30 grains in a y-z cross section of the regular packed streambed, located $x^* = 14.5$ downstream of the test section inlet. Each sensor was aligned with the centerline of the spherical grain in the x-z plane and placed 0.15 grain diameters

below the top of the grains in the upstream direction (i.e., sensor depth for top layer of grains is $z^* = -0.15$). All wires were shielded and grounded to minimize noise, and unsheathed wire leads were sealed with electrically resistive wax to ensure only the sensor was exposed. Calibrations confirmed that the 3.8-cm sensor spacing in the array did not yield interference between measurements at adjacent sensors. Wires were run downstream from the sensors and along grain-to-grain contact points to minimize disturbance of the porewater flow field.

Circuits were powered and sampled with a National Instruments PCI-6229 data acquisition board. Output and input signals were controlled and recorded using LabView Signal Express 2013 software (National Instruments, Austin, TX). Circuits were powered in parallel by a 400-mV, 100-Hz AC waveform. The returning voltage was bandpass filtered and recorded in Labview, and this file was exported to Matlab version R2015a (Mathworks, Cambridge, MA) for further analysis. All waveforms were bias-corrected and sampled at the peaks, yielding a 200-Hz sample rate.
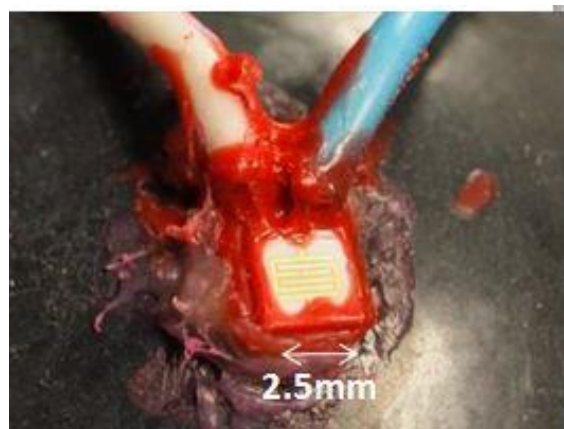
Figure 2.2. Simple-cubic-packed sediment module with sensors installed (left). Sensors were 2.5-mm square interdigitated electrodes fixed to the sediment grains with epoxy and sealed with resistive wax (right).

Sensors were calibrated *in situ*. A known volume of reverse osmosis (RO) water was first pumped into the flume from a laboratory-grade reservoir, and flow was initiated. NaCl solution was added to the flume. Once the solute was fully mixed with flume water, a one-minute conductivity time series was recorded. A three-parameter calibration curve was used of the form

$$C = \exp((V - a_3)/a_1) - a_2, \qquad R^2 \geq 0.995, \geq 9 \, dof \qquad (2.2)$$

where C is NaCl concentration, V is voltage, and a_i are constants. For all experiments, steady-state NaCl concentrations were limited to 0-200 μm, which yielded the greatest measurement sensitivity.

2.2.4 Solute transport experiments: flow conditions and measurements

Experiments were performed over a range of flow conditions reported in Table 2.1. For each flowrate the flume slope was adjusted to match the surface water slope to yield uniform flow conditions. The water surface elevation was measured with a digital point gauge attached to a rail-mounted carriage above the flume. Water column depth, H, was measured from the free surface to the tops of the sediment grains.

Table 2.1. Flow conditions for all experiments.

Re	13,000	22,000	27,000	39,000	55,000	75,000
Experiment	Solute	EPIV	Solute	EPIV	Solute	EPIV
Q (L/s)	2.2	8.0	4.4	14.0	8.8	26.0

H (cm)	12.3	16.0	12.3	16.0	12.3	16.0
Fr	0.09	0.11	0.18	0.20	0.38	0.37
$\bar{U}$ (cm/s)	10	14	20	24	41	47
$\bar{U}_p$ (cm/s)	0.7	--	1.2	--	2.8	--
d_g (cm)	3.8					
ϕ	$1 - \pi/6 \approx 0.476$					
K (cm²)	0.0321					

Free-stream velocity measurements

An acoustic Doppler velocimeter (ADV) was used to measure free-stream velocities (SonTek 16MHz MicroADV, San Diego, CA). The flume was seeded with 8-μm particles (SonTek, San Diego, CA) to increase signal-to-noise ratio for velocity measurements. Velocities were recorded at 60 Hz for a minimum of 2 min. All reported velocity statistics showed no correlation with measurement duration beyond this time. Spikes in the velocity time series were filtered using the phase-space thresholding algorithm of *Goring and Nikora* [2002] implemented in the WinADV (v2.028) software package [*Wahl*].

Three-dimensional velocities (u, v, w) were measured in vertical profiles, starting from a location 5 cm below the free surface and ending at the sediment bed. Vertical profiles were measured for six different $(x$-$y)$ positions and averaged in the x-y plane using the double-averaging method of *Nikora et al.* [2007]. The Reynolds number of the overlying (surface) flow was calculated as $Re = UH\nu^{-1}$, where U is the mean free-stream velocity, and ν is the kinematic viscosity of water, taken to be 10^{-6} m²/s. Froude number was calculated as $Fr = U(Hg)^{-1/2}$,

where g is the acceleration due to gravity. Permeability, K was estimated using the Karman-Cozeny equation [*Freeze and Cherry*, 1979; *O'Connor and Harvey*, 2008]:

$$K = 5.6 \times 10^{-3} \frac{\phi^3 d_g^2}{(1 - \phi)^2} \tag{2.3}$$

Porewater velocity measurements

Porewater velocities were measured by injecting pulses of tracer at depths $z^* = $ -0.15, -1.15, -2.15, -3.15, and -4.15. Injections were made manually for 0.5 s via narrow-gage silicon tubing that had been manually inserted into the pore space, with the tubing aligned with the y-axis and aperture located at exactly $y^* = 2$. This orientation ensured that the injection would 1) minimally affect downstream momentum transport, and 2) the injection region would include fluid volume in both the pore throat and any dead zones between sediment grains.

Injections were made at multiple locations x^* upstream of the sensor array at each depth. The concentration time series was recorded for all sensors at the injection depth, and mean fluid velocity was estimated from each sensor as $u = x/t_{peak}$, where x is the distance between the injection location and the sensor array, and t_{peak} is the time at which the peak concentration pulse was recorded by a sensor. Velocities were then averaged over all injections to obtain the overall mean porewater velocity for each row of spheres, $U_p(z)$.

2.2.5 Solute transport experiments: Steady-state solute injections

The flume was filled with RO-purified water, and then a neutrally-buoyant NaCl solution was injected into porewater via a peristaltic pump using 0.12-mm silicon tubing and a custom-

constructed pneumatic pulse dampener inserted into the injection line to reduce flow pulsation from the pump (see Supporting Information). An aquarium stone was installed onto the tubing outlet to diffuse the solution into the pore space and minimize disturbance of the porewater flow field. Each injection solution was made neutrally buoyant by heating to the appropriate temperature before injection into the flume. The injection rate was also varied with flume flowrate to ensure the injection did not alter the subsurface flow field (0.46-0.58 cm/s). Injections were performed at mid-width over a series of injection depths, z_{inj}^*. Injections were continued until salt concentrations at the sensor array reached statistical steady-state for at least 2 min. The injection concentration was adjusted in each experiment so measured concentrations were within the sensors' calibration range. A series of injections were performed until the background salt concentration reached ~10 μm, at which point the measured signal-to-background ratios became too low to fully capture tracer injection dynamics. The flume was then drained, flushed, and re-filled with RO water for subsequent experiments.

   Two sets of steady-state injections were performed at each of the 3 flowrates listed in Table 2.1. Injections near the sensor array were used to capture detailed statistics of the tracer plume before it had mixed completely with porewater ($x^* = 3.5$, $y^* = 2$, $z^* = $ -0.15,-1.15, -2.15, -3.15). A second set of injections were made at three locations upstream of the sensor array ($x^* = 3.5$, 7.5, 12.5) to capture the larger-scale plume spreading and average mass flux. All injections were performed at least $x^* = 7$ downstream of the entrance to the test section to ensure that the flow within the bed was fully developed. We confirmed experimentally that the porewater flow was

fully-developed by $x^* = 2$ (results not shown). Injections were repeated at and below the SWI (z^* = -0.15, -2.15), and at multiple transverse locations ($y^* = 2, 2.5, 3$) to obtain ensemble statistics of plume spreading.

2.2.6 Solute transport experiments: data analysis

Sensor data were background-corrected. The background concentration treated as a linear ramp to account for the steady increase in background concentration over the course of injections due to the recirculating nature of the flume. Plume spreading was analyzed over the interval when measured concentrations were at a dynamic steady state (i.e., steady except for the effects of turbulence). The resulting background-corrected time series were decomposed into their frequency content by computing power spectral densities (PSD). For a real-valued concentration time series C_n of N samples, the PSD is defined as [*Rodríguez-Iturbe and Rinaldo*, 2001]:

$$\hat{P}(f) = \frac{2\Delta t}{N} \left| \sum_{n=0}^{N-1} C_n e^{-i2\pi f n} \right|^2 \tag{2.4}$$

where Δt is the time between samples and $\hat{P}(f)$ is the spectral power at frequency f. PSDs were normalized by the signal variance, σ^2:

$$\hat{P}(f)_{norm} = \frac{\hat{P}(f)}{\sigma^2} \tag{2.5}$$

$$\sigma^2 = \int_{0.1\,Hz}^{2\,Hz} \hat{P}(f)\mathrm{d}f \tag{2.6}$$

The limits of integration in Equation (2.7) correspond to the lowest common frequency measured across all experiments, 0.1 Hz, and the frequency at which spectral power decayed beyond 1% of its maximum for all experiments, 2 Hz. To compare across experiments, PSDs were integrated to determine the range of frequencies that accounted for 95% of the signal variance, σ_{95}^2:

$$\sigma_{95}^2 = \int_{0.1\,Hz}^{f_{95}} \hat{P}(f)\mathrm{d}f \tag{2.7}$$

where f_{95} represents the frequency below which 95% of signal variance is captured. An increase in f_{95} between experiments indicates an increasing contribution from higher frequencies.

Mean concentration, $\bar{C}(z)$, was calculated for each sensor and then averaged over all sensors at each depth. Row-averaged values are reported as $\langle\bar{C}\rangle_y$ Root-mean-square concentrations, $C_{rms} = \sqrt{\sigma^2}$, were normalized by the mean concentration measured across all sensors in the injection row where a non-zero concentration was recorded.

2.2.7 Solute transport experiments: Whole streambed analysis

Mass recovery was used to quantify the amount of injected solute that exchanged from the porewater to the water column. Recovery, R, is quantified as the fraction of injected mass, m_{inj}, that was measured at the sensor array, m_{meas}:

$$R = \frac{m_{meas}}{m_{inj}} \tag{2.8}$$

$$m_{meas} = \frac{1}{\phi} \int_{z=-5.15d_g}^{0} C_{mean} \, dz \tag{2.9}$$

$$m_{inj} = \frac{C_{inj} \, Q_{inj}}{U_p \, w} \tag{2.10}$$

where C_{inj} is the injection concentration, Q_{inj} is the injection flowrate, ϕ is bed porosity, $\overline{U}_p$ is the mean porewater velocity, w is the flume width, and $z = -5.15d_g$ is the location of the lowest row of sensors. Here, m is interpreted as a measure of mass per unit area in the x-y plane [M/L^2]. Note that an implicit assumption of (2.9) is that solute is fully mixed over the unit cell comprising the pore volume surrounding each sphere. The integral in Equation (2.9) was evaluated numerically using the trapezoid rule.

Effective dispersion model

A 1-D vertical dispersion model was fit to subsurface injections ($z_{inj}^* = -2.15$) to evaluate if the observed tracer transport could be adequately represented as an effective dispersion process:

$$\frac{\partial C_{pred}}{\partial t} = D_{eff} \frac{\partial^2 C_{pred}}{\partial z^2} \tag{2.11}$$

$$C_{pred}(0, t) = 0$$

where C_{pred} is the predicted concentration of all sensors in a given row and D_{eff} is a spatially uniform dispersion coefficient. D_{eff} was obtained for each injection by fitting to the profile of $\langle \bar{C} \rangle_{y,mod}$. The analytical solution to (2.11) is:

$$\langle \bar{C} \rangle_{y,mod}(z, x) = \frac{M}{\phi \left(4\pi D_{eff} \, x/\overline{U}_p\right)^{0.5}} \left(e^{-\frac{(z-z_{inj})^2}{4D_{eff} \, x/\overline{U}_p}} - e^{-\frac{(z+z_{inj})^2}{4D_{eff} x/\overline{U}_p}} \right) \tag{2.12}$$

where erf is the error function, and M is a normalization mass. Two different normalization masses were tested:

$$M = m_{inj} \tag{2.13}$$

$$M' = \frac{2}{\phi} \int_{z=-5.15d_g}^{z_{inj}} C_{mean} dz. \tag{2.14}$$

Equation (2.13) normalizes results using the total mass using the total mass injected while Equation (2.14) normalizes results based on integration over the concentration profile. Normalization based on Equation (2.14) assumes that mixing is uniform below the injection location (i.e., mixing is not enhanced by flow coupling) and no tracer has reached the flume bottom. Fits for the dispersion coefficient based on M' are denoted by D'_{eff}.

D_{eff} fits obtained from each concentration profile were averaged to calculate ensemble-average estimates of the effective dispersion coefficient at each flowrate, D_{ens}. These values were then used to generate predictions for ensemble concentration profiles, from Equation (2.12), with D_{ens} in place of D_{eff}. Predicted mass recovery, defined as the fraction of injected mass retained in the streambed at downstream distance x, was also calculated from the analytical solution to Equations (2.11):

$$R_{pred} = \int_{-\infty}^{0} \langle C \rangle_{y,pred}(z,x) dz = -\text{erf}\left[\frac{z_{inj}}{\left(4D_{ens} \, x/\bar{U}_p\right)^{0.5}} \right]. \tag{2.15}$$

Mass retention is plotted against the dimensionless timescale associated with vertical mixing over one grain diameter:

$$t^* = \frac{(x/\overline{U}_p)D_{eff}}{d_g^2} \qquad (2.16)$$

Because the experiments were conducted under steady conditions, t^* also corresponds to the

downstream distance required for vertical mixing over one grain diameter. Normalization by t^*

collapses all model predictions into a single curve.

2.3 Results

2.3.1 Surface-porewater flow coupling

Profiles of mean longitudinal velocity and turbulent stresses, measured in EPIV experiments,

are presented in Figure 2.3. All profiles were characterized by a non-zero velocity at the SWI.

Mean porewater velocities exhibited a minimum $z^* = -1$, which is consistent with prior studies of

turbulent flows over a simple-cubic-packed bed of spheres [*Pokrajac et al.*, 2007; *Manes et al.*,

2009]. Turbulent $\overline{u'w'}$ and $\overline{w'w'}$ plots both show elevated values at the SWI and exponentially

decreasing values in the subsurface. The magnitude of peak $\overline{u'w'}$ stress was greatest at the SWI

for all Re. $\overline{u'w'}$ values decayed to 1% of their peak value by $z^* = -2$ for $Re = 75,000$ and by $z^* = -$

1 for $Re = 22,000$ and $39,000$.
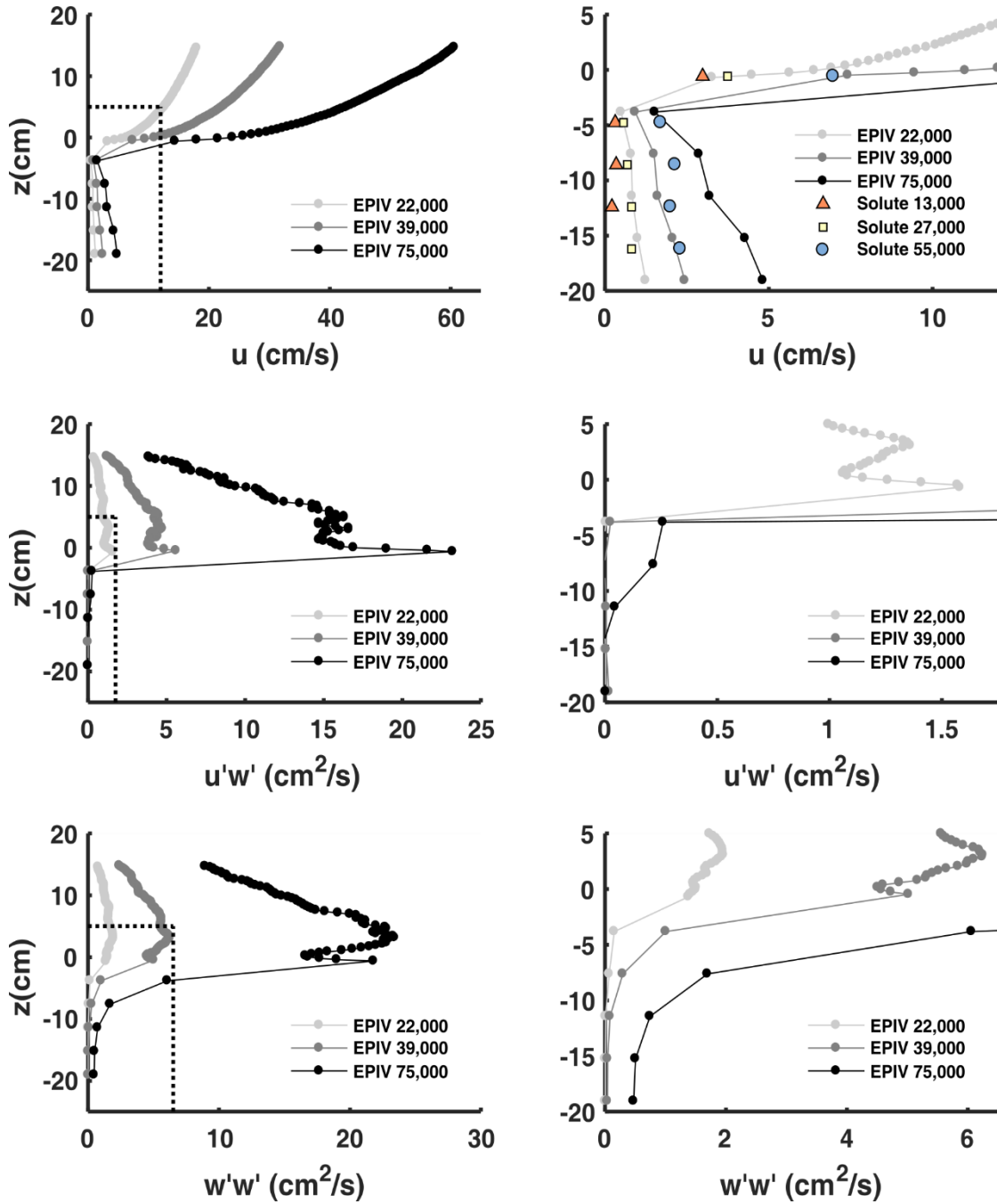
Figure 2.3. Left: Profiles of first- and second-order velocity statistics for EPIV experiments. Dotted rectangle represents region shown in adjacent plots. Right: Same profiles, with only near-bed and subsurface shown.

2.3.2 Solute transport results

Flow visualizations and **in situ** *concentration measurements*

Flow visualizations from surface and subsurface injections ($z_{inj}^* = $ -0.15 and -2.15,

respectively) show rapid mixing at the SWI (see Supporting Information). The large sediment

grains act as roughness elements that protrude into the bulk flow, recirculation cells formed

between grains and enhanced exchange with porewaters. These recirculations are most visible

and persist longest at $Re = $ 13,000. Larger-scale interactions between the water column and

porewaters are visible to a depth of at least 2 grains below the SWI for $Re = $ 27,000 and 55,000.

Interactions appear as intermittent ejections of high concentration, low velocity fluid into the

water column (Figure 2.4). These results suggest that coherent motions of size $l \geq 2d_g$ are

influencing subsurface transport. Ejection frequency and intensity increased from $Re = $ 27,000 to

$Re = $ 55,000, but they are not present at $Re = $ 13,000.

0.00 s	0.75 s	1.25 s	2.00 s
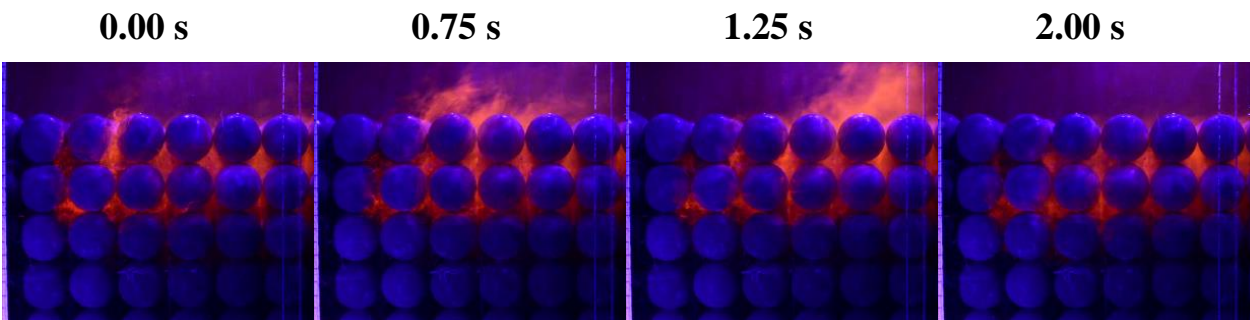
Figure 2.4. Ejection event during a subsurface injection ($z_{inj}^* = $ -2.15) at $Re = $ 55,000. Images at 0.75 s and 1.25 s show that the event is at least 2 sediment grains wide. Sediment grains are 3.8 cm in diameter.
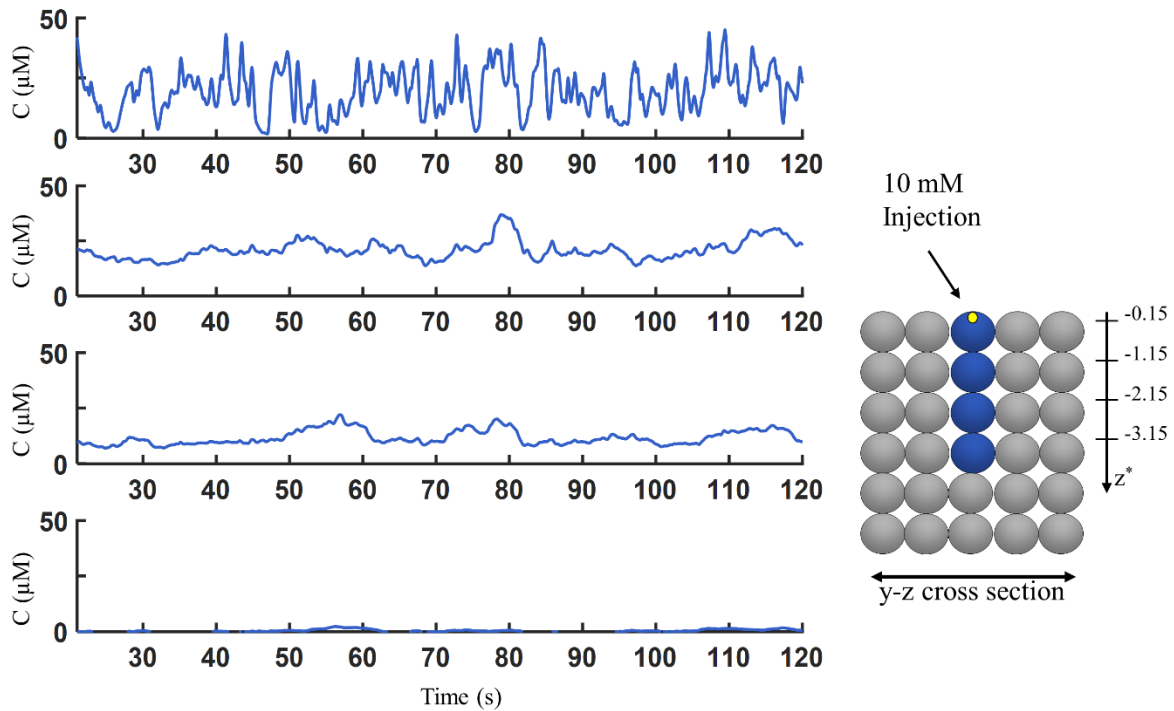
Figure 2.5. Time series observations of solute concentrations for an injection at location $(x_{inj}^*, y_{inj}^*, z_{inj}^*) = (3.5, 2.5, -0.15)$ under a flow rate of 8.8 L/s. Injection and observation locations over a cross-section of the bed are shown on the right. Flow is into the page, yellow dot indicates the injection location, and the monitoring locations are indicated with blue spheres.

In situ solute measurements show that energetic, high-frequency fluctuations dominate the time series near the SWI (Figure 2.5). Concentration fluctuations are most intense at the SWI. High frequency fluctuations decay with depth in the bed, while lower-frequency fluctuations persist at deeper locations. These trends are also observed in power spectral density and f_{95} plots (Figure 2.6a,b). An asymptotic limit in f_{95} was reached within one grain diameter for $Re = $ 13,000 and 27,000, but f_{95} decays more slowly and to a higher asymptote for $Re = 55,000$. These trends are coincident with the second-order turbulence statistics reported in Figure 2.3,

which show rapid decay of $\overline{u'w'}$ and $\overline{w'w'}$ stresses over roughly one grain diameter for $Re =$ 22,000 and 39,000, but greater turbulent penetration to a depth of ~2 grain diameters at $Re =$ 75,000.

   Overall concentration variability, quantified by normalized C_{rms} values, is presented in Figure 2.6c. These profiles differ from profiles of f_{95} and turbulence statistics by exhibiting a peak concentration below the SWI, which moves deeper into the streambed with increasing flowrate. Peak C_{rms} at $Re =$ 27,000 and 55,000 also corresponds to the position where $\overline{u'w'}$ stresses have decayed to <1% of their maximum for EPIV experiments at similar Re (39,000 and 75,000, respectively). This suggests that the location of peak C_{rms} is found below the streambed depth where turbulent shear stresses affect solute mixing. The location of peak C_{rms} was observed at the SWI for $Re =$ 13,000, which indicates that solute transport was not influenced by turbulent shear stresses beyond one grain diameter for this flowrate. This result is supported by the similarity of $\overline{u'w'}$ stress and C_{rms} profiles at $Re =$ 22,000 (Figure 2.3) and 13,000, respectively, which approach zero within the first grain diameter of the bed.
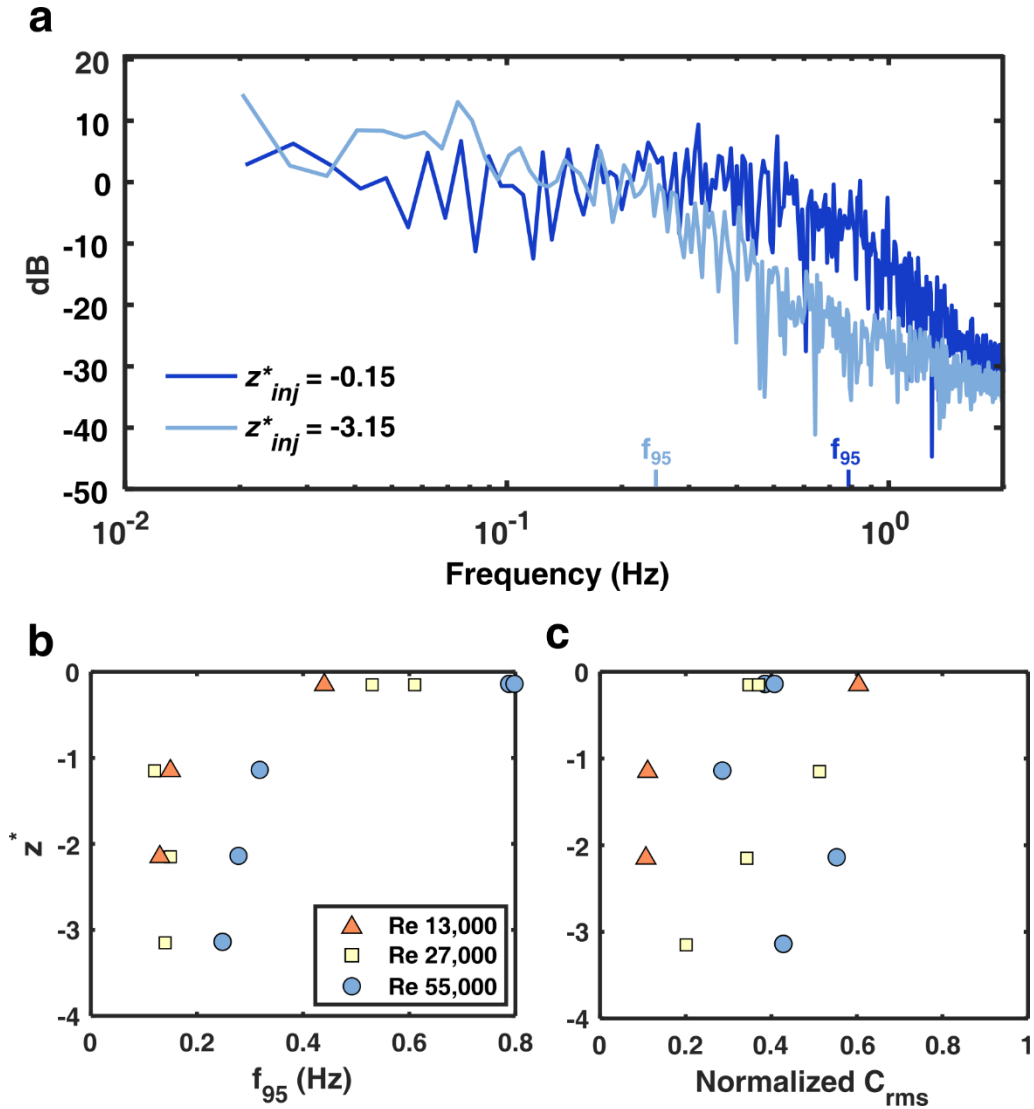
Figure 2.6. (a) Power spectral densities for two injections at $x^*_{inj} = 3.5$, $y^*_{inj} = 2$ and $Re = 55{,}000$. High-frequency power is filtered within the streambed, while power at low frequencies is similar at all depths. (b) Profiles of f_{95} for experiments at $x^*_{inj} = 3.5$, $y^*_{inj} = 2$. f_{95} values, derived from power spectral densities using Equation (2.7), capture the shift to variability dominated by lower frequencies. Higher frequencies contribute to signal variability at higher flowrates, and high frequency content decreases to asymptotic values at similar rates as the decay of turbulent stresses, shown in Figure 2.3. (c) Location of peak C_{rms} propagates deeper into the streambed as flowrate increases.

Upscaled solute transport properties

Mean concentration profiles for subsurface (z_{inj}^{*} = -2.15) injections were used to calculate an effective vertical dispersion coefficient D_{eff} for each flowrate. Example fits based on the two mass normalizations M and M' (Equations (2.13) and (2.14), respectively) are shown in Figure 2.7a. Fits based on the injection mass ($M = m_{inj}$, solid line) resulted in substantial overestimation of the effective dispersion rate, as the model attempted to compensate for the large fraction of input mass that was lost to the water column. These fits were unrealistic, since they predicted propagation of tracer several grain diameters beyond the depth of the streambed. Model performance, measured by R^2 values (see supporting information), also showed a clear dependence on overall mass recovery R (Equation (2.8)). Note that application of a reflective boundary at the flume bottom would have resulted in equally unrealistic fits, since little-to-no tracer was observed at the deepest sensors in all experiments. In contrast, model fits using normalization mass M' provided reasonable predictions at all locations below the injection point. Values of D'_{eff}, based on the normalization M'(Equation (2.14)), were therefore use to generate ensemble-averaged values of the effective dispersion coefficient, D_{ens} (Figure 2.7b). D_{ens} values show a monotonic increase with flowrate, though the estimated values are not significantly different between Re = 13,000 and 27,000.
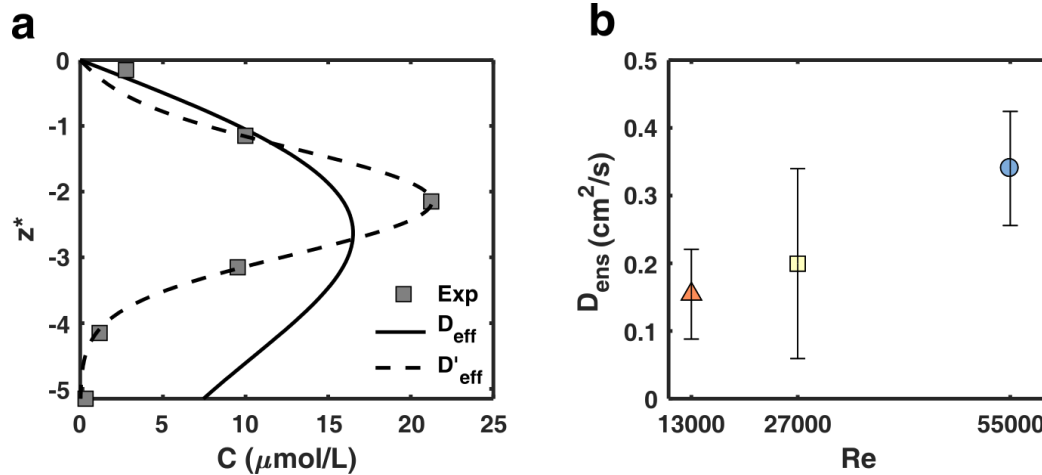
Figure 2.7. (a) Comparison of observed (squares) and fit (lines) downstream concentration profiles C(z^*) for an experiment with Re = 27,000, x^*_{inj} = 12.5, z^*_{inj} = -2.15. Fits normalized to mass below the injection point (dashed line) better represent observed concentrations at all bed depths. (b) Ensemble average of all best-fit effective dispersion coefficients at each flowrate. Error bars show 1 standard deviation.

Modeled concentration profiles based on D_{ens} are compared to ensemble-averaged observations in Figure 2.8. Enhanced mixing at depths -2.15 $\leq z^* \leq$ -0.15 is most visible at Re = 55,000, evidenced by much faster propagation away from the injection location at these depths compared to the model predictions (Figure 2.8a,b,d). Asymmetry of observed concentrations about the subsurface injection point is due to the combined effect of rapid solute propagation near the SWI, which dominates at early times (Figure 2.8a) and enhanced mass loss to the water column, which dominates at late times (Figure 2.8e). Rapid mixing at -2.15 $\leq z^* \leq$ -0.15 also results in greater mass exchange than the model predicts with uniform D_{ens}, evidenced by the lower observed mass recovery for all but one experiment in Figure 2.9.
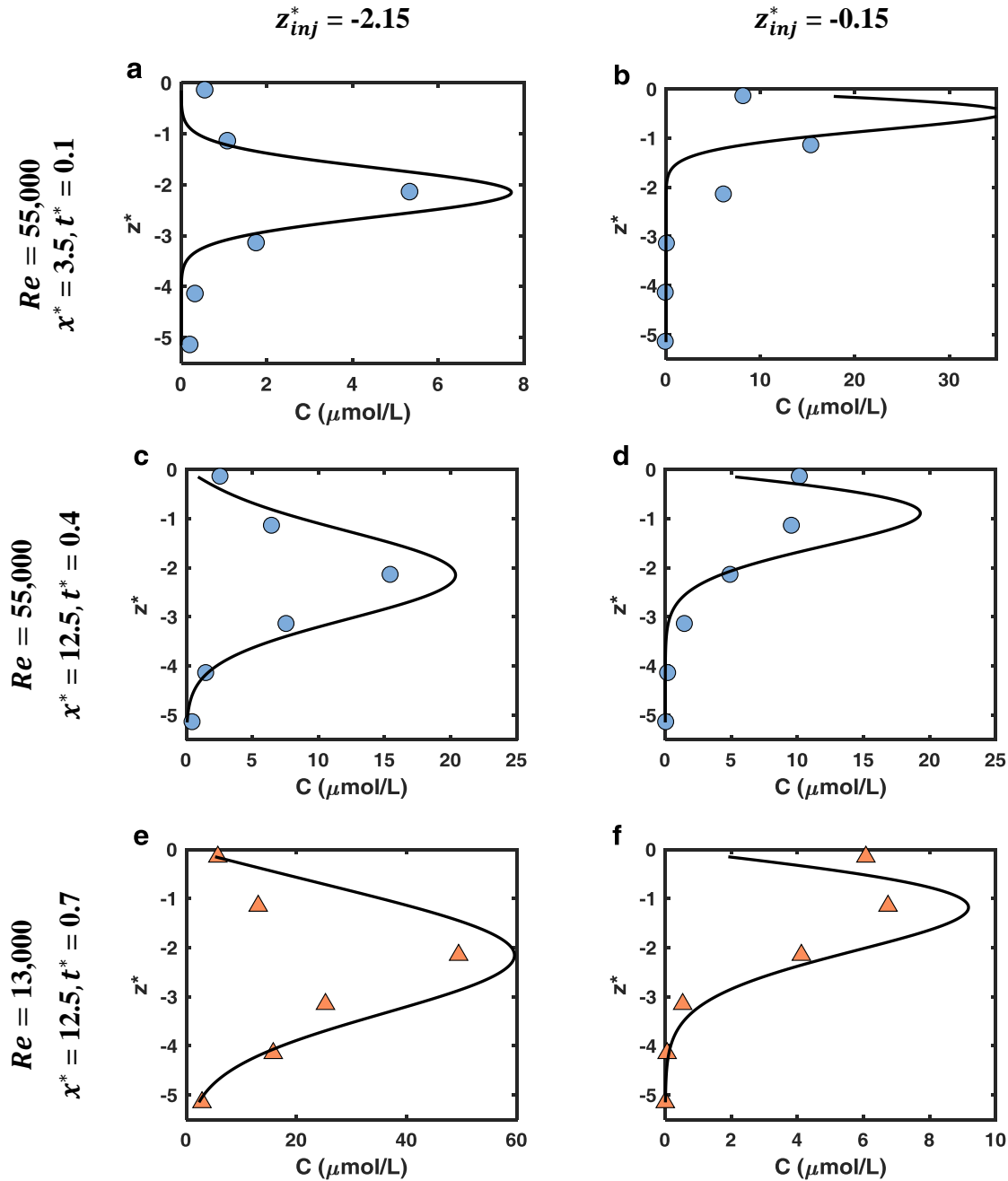
Figure 2.8. Comparison of ensemble-averaged mean concentrations profiles observed in experiments (markers) with constant-coefficient dispersion model fits (solid lines). The model best describes transport at depths below $z^* \approx -2.15$ but does not adequately describe enhanced mixing at depths $-2.15 \leq z^* \leq -0.15$.

Observed concentrations near the SWI deviated from the modeled concentration profiles approximately 75% faster at $Re = 55,000$ (Figure 2.8c,d) than at $Re = 13,000$ (Figure 2.8e,f), evidenced by the similarity of the profiles at $t^* = 0.4$ and 0.7 for the different flow conditions.

Differences between $Re = 13,000$ and higher flow experiments are also observed in plots of mass retention (Figure 2.9). Observed deviations from the model curve are expected to follow the same trend if subsurface transport scales directly with bulk Reynolds number. Trends at $Re = 27,000$ and 55,000 show similar trends, while experiments at $Re = 13,000$ show that approximately 50-100% more time was necessary to exchange the same amount of mass with the water column (e.g., mass recovery is 0.7 at $t^* \sim 0.4$ for intermediate and high flows but does not reach this value until $t^* \sim 0.7$ for low flows). This difference is likely due to the emergence of large-scale sweep and ejection events by $Re = 27,000$, which enhance mixing from $-2.15 \leq z^* \leq -0.15$ compared to flows at lower Re. Note that two values at $Re = 13,000$ ($x_{inj}^*, z_{inj}^* = 3.5, -2.15$ and 7.5, -2.15) and one value at $Re = 27,000$ ($x_{inj}^*, z_{inj}^* = 3.5, -2.15$) are not plotted due to incomplete mixing of the slowly spreading solute plume (i.e., plume width $< d_g$). Mass retention is considered equal to 1 for these experiments.
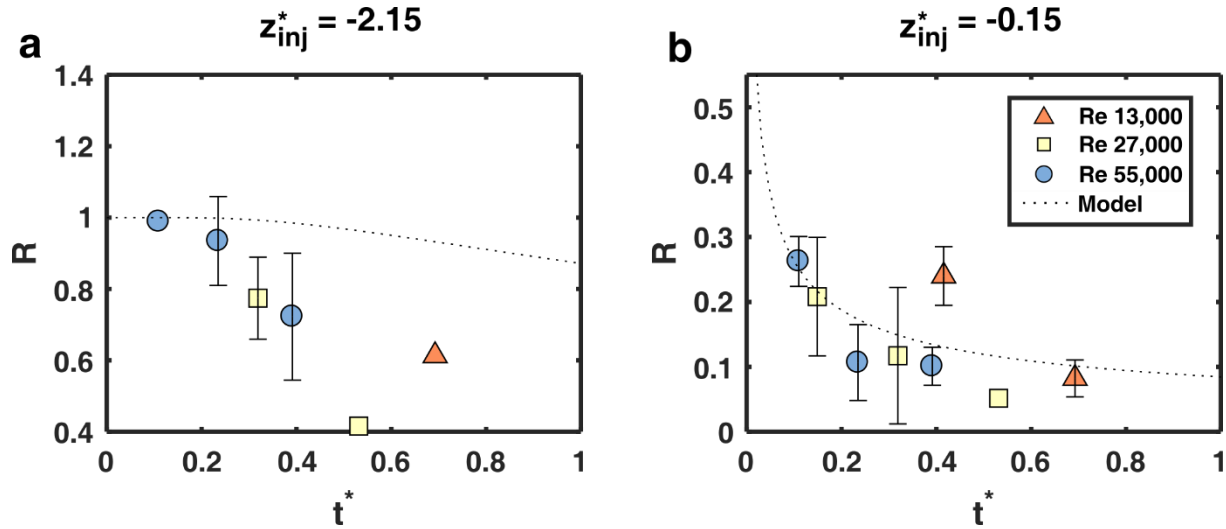
Figure 2.9. Observed mass retention in the streambed compared with upscaled best-fit effective dispersion model. (a) $z_{inj}^* = -2.15$, (b) $z_{inj}^* = -0.15$. Note the change in y-axis scales. Experiments at $Re = 13{,}000$ follow a distinct trend from experiments at higher Re.

2.4 Discussion

The open pore geometry of coarse-grained sediment beds allows turbulent transport of both momentum and mass across the SWI, thereby coupling surface and porewater flows. This coupling modifies the flow structure across the surface-subsurface continuum. Subsurface transport appears to be relatively unaffected by flow variability at the $Re = 13{,}000$, with small-scale ($<0.5d_g$) recirculations visible only on the lee side of sediment grains. In contrast, transport at $Re = 27{,}000$ and $55{,}000$ is clearly influenced by the presence of intermittent, large-scale ejections of porewater originating from depths $-2.15 \leq z^* \leq -0.15$. This behavior suggests that transport at high flows is driven by a shear instability at the SWI, which is known to control momentum and mass transport over vegetation canopies. Hyporheic exchange over coarse-

grained sediment beds may therefore fall within a single framework for shear-driven flows over porous media, as posited by *Ghisalberti* [2009].

Porewater hydrodynamics directly controlled solute transport and hyporheic exchange over the full range of flowrates tested. Flow visualizations showed that small-scale recirculations are increasingly disrupted and large-scale sweep/ejection events grow more frequent and energetic with increasing Re. Reynolds stresses and f_{95} both decreased rapidly below the interface to stable values by $z^* = -1.15$ for $Re \leq 39,000$ (Figures 2.3 and 2.6a, respectively), but both metrics decreased more gradually to $z^* \approx -2.15$ for $Re \geq 55,000$. This suggests that high frequency concentration fluctuations are controlled by velocity fluctuations near the SWI.

C_{rms} values peaked deeper in the bed under higher flow rates (Figure 2.6c). The peak corresponded to the location where the Reynolds' stresses $\overline{u'w'}$ and $\overline{w'w'}$ decayed in the bed, meaning turbulent velocity fluctuations did not directly control overall concentration variability in porewaters. The location of peak C_{rms} corresponds to the location where longer-period concentration fluctuations were observed in flow visualizations and in solute time series (Figure 2.5, Figure 2.6a). These fluctuations have been observed previously in gravel beds and are related to low-frequency pressure oscillations induced by the interaction of free-stream turbulence with the streambed [*Vollmer et al.*, 2002; *Packman et al.*, 2004]. The streambed acts as a low-pass filter for turbulent velocity and pressure fluctuations, allowing low-frequency fluctuations to propagate to greater depths than high frequencies [*Breugem et al.*, 2006]. The numerical results of *Chandesris et al.* [2013] suggest that these fluctuations contribute to

porewater advection but not to enhanced mixing within porewaters. This hypothesis is supported by flow visualizations, which show evidence of low mixing at the location of peak C_{rms}, as well as by concentration profiles (Figure 2.8), which show that observed concentrations below $z^* \approx$ -2.15 are well described by a spatially invariant dispersion coefficient.

Occurrence of maximum C_{rms} at the SWI under the lowest flow condition, $Re = 13{,}000$, suggests that turbulence did not influence mixing beyond a depth of one grain diameter under this condition. Near-zero $\overline{u'w'}$ and $\overline{w'w'}$ stresses, as well as results from dispersion model fits (Figure 2.8), provide further evidence that subsurface hydrodynamics approach uniform values by $z^* \approx$ -1.15 at the low flowrate. Collectively, these results suggest that the bed approached a uniform mixing regime in the subsurface under lower water column velocities. In contrast, enhanced subsurface mixing was observed under higher stream flowrates. For surface injections close to the sensor array, tracer propagated at least 8 cm below the SWI after just 2 s of travel ($t^* = 0.1$, Figure 2.8b). The rate of propagation slowed substantially beyond 8 cm ($z^* = $-2.15) (Figure 2.8d). A rapid transition to slower, uniform mixing therefore takes place at depth of 2-3 grain diameters for this flowrate, corresponding to the depth where $\overline{u'w'}$ and $\overline{w'w'}$ stresses decay to 1% and 8% of peak values in EPIV experiments. This finding indicates that regions of enhanced mixing directly correspond to regions of high turbulent stress.

2.5 Conclusions and implications

Our results show that high-frequency concentration variability and enhanced mixing are directly linked to penetration of turbulence into the hyporheic zone. Turbulent stresses and high-

frequency concentration fluctuations decay with depth in the bed. Turbulent momentum fluxes across the sediment-water interface control mass retention and recovery in porewater. However, turbulence also influences solute transport beyond this depth, as low-frequency oscillations penetrate deeper into the bed.

The simple cubic packing of sediments in the present study represents an endmember case, whose open geometry allows maximal penetration of coherent flow structures from the water column. Streambeds with smaller sediments or closer packing are expected to obstruct penetration of these structures, reducing turbulent surface-subsurface flow coupling. Predictive relations for turbulent hyporheic exchange must therefore account for physical aspects of the streambed in addition to the near-bed flow structure [*Ghisalberti and Nepf*, 2005; *Breugem et al.*, 2006; *O'Connor and Harvey*, 2008; *Voermans et al.*, 2017].

The link between turbulent stresses and scalar transport is system independent [*Tennekes and Lumley*, 1972], indicating that our findings are applicable to different streambed geometries and flowrates provided details. The longstanding pursuit of generalized relations for momentum transport in high-permeability streambeds will therefore have direct implications for upscaled predictions of hyporheic exchange, given the direct linkage between subsurface momentum and mass transport presented here. Our findings point to recent scaling laws that directly incorporate shear instabilities at the sediment-water interface [*Ghisalberti*, 2009; *Voermans et al.*, 2017], evidenced by the clear increases in mass exchange that emerge when large-scale ejection events are present.

Physically-based scaling relationships for turbulent hyporheic mass transport are needed for general application of upscaled hyporheic exchange models [*Workshop*, 1990; *Haggerty et al.*, 2002; *Schumer et al.*, 2003; *Boano et al.*, 2007; *Stonedahl et al.*, 2012]. A physically-based parameterization for turbulent hyporheic exchange is also needed to distinguish this process from other solute retention processes that operate at similar timescales, such as exchange with side pools, benthic biofilms, and in-stream structures [*Uijttewaal et al.*, 2001; *Battin et al.*, 2003a; *Ensign and Doyle*, 2005; *Gooseff et al.*, 2005; *Bottacin-Busolin et al.*, 2009; *Orr et al.*, 2009; *Jackson et al.*, 2013]. Independent parameterization of these mechanisms will improve assessment of biogeochemical transformation from whole-stream tracer injection experiments, since they will explicitly account for the distinct transport processes and reaction kinetics associated with each region of the stream [*Jones and Mulholland*, 1999; *Boano et al.*, 2014; *Aubeneau et al.*, 2015b; *Li et al.*, 2017].

2.6 Supporting Information

Flow visualizations for subsurface solute injections are provided.
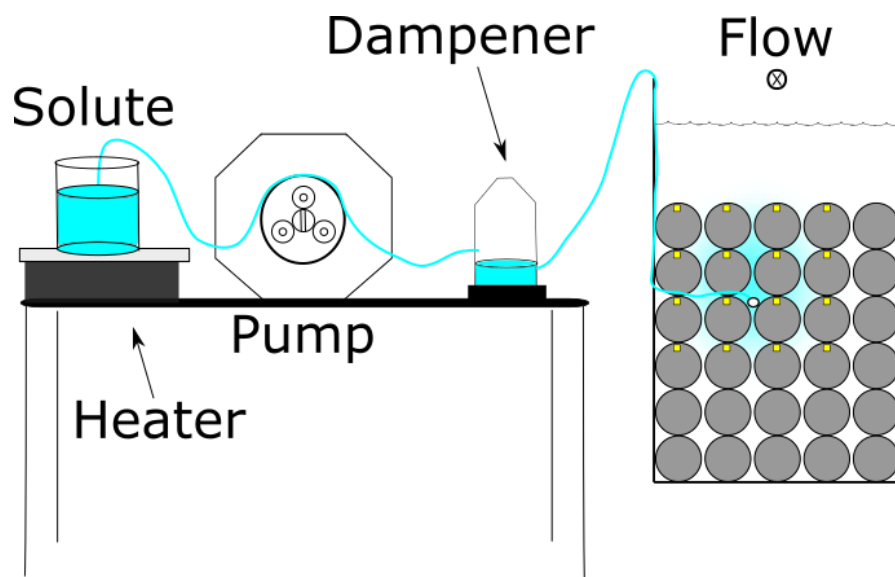
Figure 2.10. Schematic of injection setup. Solute was heated to neutral buoyancy prior to injection. A custom flow dampener (inverted vortex tube with) was installed in-line to minimize pulsation from the peristaltic pump.

CHAPTER 3

Effects of turbulent hyporheic mixing

on reach-scale solute transport

ABSTRACT

Turbulence rapidly mixes solutes and fine particles into coarse-grained streambeds. Both hyporheic exchange rates and spatial variability of hyporheic mixing are known to be controlled by turbulence, but it is unclear how turbulent mixing influences mass transport at the scale of stream reaches. We used a process-based particle-tracking model to simulate local- and reach-scale solute transport for a coarse-bed stream. Two vertical mixing profiles, one with a smooth transition from in-stream to hyporheic transport conditions and a second with enhanced turbulent transport at the sediment-water interface, were fit to steady-state subsurface concentration profiles observed in laboratory experiments. The mixing profile with enhanced interfacial transport better matched the observed concentration profiles and overall mass retention in the streambed. The best-fit mixing profiles were then used to simulate upscaled solute transport in a stream. Enhanced mixing coupled in-stream and hyporheic solute transport, causing solutes exchanged into the shallow subsurface to have travel times similar to the water column. This extended the exponential region of the in-stream solute breakthrough curve, and delayed the onset of the heavy power-law tailing induced by deeper and slower hyporheic porewater velocities. Slopes of observed power-law tails were greater than those predicted from stochastic transport theory, and also changed in time. In addition, rapid hyporheic transport velocities truncated the hyporheic residence time distribution by causing mass to exit the stream reach via subsurface advection, causing strong exponential tempering in the in-stream breakthrough curves at the timescale of advective hyporheic transport through the reach. These results show that

strong turbulent mixing across the sediment-water interface violates the conventional separation of surface and subsurface flows used in current models for solute transport in rivers. Instead, the full distribution of flow and mixing over the surface-subsurface continuum must be explicitly considered to properly interpret solute transport in coarse-bed streams. The results presented here support upscaled numerical solutions based on the particle tracking method, which directly represents solute transport in both the stream and the hyporheic zone. Field application will require detailed observations of flow and transport across the stream-hyporheic continuum, as well as development of new upscaled theory that respects the strong stream-hyporheic coupling demonstrated here.

3.1 Introduction

Transport and transformation in the hyporheic zone is closely linked both to the structure of stream sediments and to streamflow. Sediment properties such as grain size and surface chemistry influence habitat for microbial biofilms, which are a primary driver of subsurface reactions, and hyporheic residence times, and they also control the opportunity for biogeochemical transformation [*Boulton et al.*, 1998; *Battin et al.*, 2007; *Battin et al.*, 2016]. Streambed topography and permeability interact with stream and groundwater flow to set the rate and timing of solute transport in the hyporheic zone. The balance between residence timescales and reaction timescales exerts primary control over integrated transformation rates in river networks [*Zarnetske et al.*, 2011; *Harvey et al.*, 2013]. Thus, an accurate, physically-based description of hyporheic exchange rates and residence time distributions is needed to make generalized predictions of solute retention and transformation in streams and rivers.

Considerable research over the last 30 years has shown that hyporheic exchange is generally controlled by advective porewater flows induced by stream features such as dunes, bars, and meanders [*Boano et al.*, 2014]. However, nearly all available models consider the stream flow to be fully turbulent but hyporheic flows to be laminar, and all models of advective hyporheic exchange (pumping) apply Darcy flow assumptions in the subsurface [*Cardenas and Wilson*, 2007; *Marion et al.*, 2008; *Karwan and Saiers*, 2012]. A small number of studies have shown the hyporheic exchange is also induced by turbulence that propagates across the SWI [*C P Richardson and Parr*, 1988; *Nagaoka and Ohgaki*, 1990; *Packman et al.*, 2004; *Voermans et al.*,

2017]. Despite some progress integrating this information into models for upscaled hyporheic exchange and associated solute transport [*Nagaoka and Ohgaki*, 1990; *Higashino et al.*, 2009; *Boano et al.*, 2011], full integration has remained a challenge due to an incomplete understanding of turbulent interfacial momentum transport. Sediment permeability and in-stream turbulent energy together control the extent to which turbulent eddies propagate across the SWI [*Breugem et al.*, 2006; *Manes et al.*, 2012]. Surface and subsurface flows become increasingly coupled at high flowrates, particularly for flows over high-permeability sediment beds [*Manes et al.*, 2011]. Interfacial momentum coupling modifies the flow structure across the surface-subsurface continuum by increasing subsurface velocities, amplifying turbulent shear and vertical stresses, and shifting the peak in turbulent energy closer to the SWI [*Voermans et al.*, 2017]. The resulting interfacial exchange rates can increase by orders of magnitude beyond advective pumping [*O'Connor and Harvey*, 2008]. However, turbulent energy diminishes exponentially with increasing depth in the streambed, limiting the thickness of the turbulent interfacial layer to several grain diameters [*Vollmer et al.*, 2002; *Breugem et al.*, 2006; *Manes et al.*, 2009].

These processes are known to fundamentally violate assumptions of all available models for upscaled solute transport in rivers, as current models rely on separation of velocity scales and associated travel time scales between the stream and hyporheic zone [*Boano et al.*, 2007; *Boano et al.*, 2014]. In particular, the combination of rapid interfacial transport and high porewater velocities in the turbulent portion of the hyporheic zone means that the surface and surbsurface flows are fully hydrodynamically coupled [*Manes et al.*, 2009; *Blois et al.*, 2012; *Blois et al.*,

2013], and that downstream transport within the hyporheic zone will occur at velocities similar to the stream. This violates the assumption of separation of in-stream and hyporheic timescales used in both classical hyporheic transport models (e.g., Transient Storage Model) and more recent models based on stochastic transport theory (e.g., Continuous-Time Random Walk, Time-Fractional Advection-Dispersion Equations, Multirate Mass Transfer) [*Haggerty et al.*, 2000; *Schumer et al.*, 2003; *Boano et al.*, 2007]. However, it is unclear how turbulent hyporheic exchange impacts overall mass retention at the scale of stream reaches, given that the turbulent portion of the hyporheic zone is often a small fraction of the overall streambed depth. Assessment of these processes from integrated measurements of solute transport (i.e., breakthrough curves) is further confounded by the presence of retention mechanisms active at similar timescales, such as slow in-stream velocities in the benthic boundary layer, velocity variations around cobbles and other obstructions, and lateral exchange with side pools [*Uijttewaal et al.*, 2001; *Battin et al.*, 2003a; *Ensign and Doyle*, 2005; *Gooseff et al.*, 2005; *Bottacin-Busolin et al.*, 2009; *Orr et al.*, 2009; *Jackson et al.*, 2013].

Recently, controlled experimental investigations using new *in situ* measurement approaches have provided direct observations of turbulent porewater flow and associated interfacial solute transport (Chapter 2) [*Blois et al.*, 2012]. New theoretical and modeling approaches are needed to assess the effect of enhanced turbulent hyporheic exchange on integrated transport at the reach scale. To this end, we used a process-based particle tracking model to simulate mass transport in a stream with a coarse sediment bed. We identified profiles of vertical hyporheic mixing from the steady-state subsurface concentration distributions observed in Chapter 2, then used these

profiles to simulate upscaled in-stream solute transport. Upscaled results were interpreted in terms of breakthrough curves, particle residence time distributions and Lagrangian statistics of the ensemble mass transport. This information was then used to identify specific transport regimes and specific features of concentration breakthrough curves associated with turbulent exchange. These results define the range of conditions over which subsurface turbulence must be considered in upscaled transport models, and aids interpretation of field experiments that infer hyporheic residence times from in-stream breakthrough curves. Ultimately, this work will inform proper selection of reduced-order (1-D) transport models by clarifying linkages between in-stream and subsurface residence time distributions that violate the independence assumptions of current upscaled models.

3.2 Methods

We used a stochastic particle-tracking model to simulate downstream transport at the laboratory and the reach scales. The 2-D model discretizes tracer into a large number of infinitesimal mass particles, whose ensemble motion represents the evolution of the tracer plume. Particle motion at each time step is specified by a 2-D Langevin equation:

$$x(t + \Delta t) = x(t) + u_x(z)\Delta t \tag{3.1}$$

$$z(t + \Delta t) = z(t) + \frac{\partial K_z(z)}{\partial z}\Delta t + \xi\sqrt{2K_z(z)\Delta t}$$

where $x(t)$ is downstream position at time t, y is vertical position, and Δt is a unit time step. $u_x(z)$ and $K_z(z)$ represent vertically-varying fields of longitudinal velocity and vertical mixing intensity, respectively, and ξ is an independent random variable sampled from the standard

normal distribution. Equation (3.1) is a discrete stochastic representation of the 2-D advection-dispersion equation (ADE):

$$\frac{\partial C}{\partial t} + u_x \frac{\partial C}{\partial x} = \frac{\partial}{\partial z}\left(K_z \frac{\partial C}{\partial z}\right). \tag{3.2}$$

Equation (3.2) is the conventional formulation for 2D (downstream-vertical) transport in rivers but is only valid for ensemble motion under conditions where the central limit theorem applies, which is not always the case in rivers [*Boano et al.*, 2007]. In particular, Equation (3.1) provides a consistent framework for simulating the ensemble motion of solute mass subject to co-varying velocities and mixing intensities [*Li et al.*, 2017].

3.2.1 Model formulation

We simulated transport in a stream flowing over and through a coarse-grained streambed. The entire stream-subsurface domain is considered as a flow continuum. The influence of stream sediments on particle motion is captured by the vertical variability of the velocity and mixing profiles. Velocities were simulated at three different flow conditions, which are reported in Table 3.1) Velocity profiles $u_x(z)$ at each flow condition were taken directly from recent flume experiments with water column height $H = 12.3$ cm and a bed that consisted of 4-cm spherical sediments in a simple cubic packing to a depth of depth of $d_{bed} = -22.4$ cm (Chapter 2). These values vary slightly from the values reported in Chapter 2 because the values reported here are double-averaged over multiple velocity profiles in space [*Nikora et al.*, 2001]. Discharge was directly measured in flume experiments. Reynolds numbers are calculated as $Re = H\overline{U}_s/\nu$, where $\overline{U}_s$ is mean water column velocity, and the kinematic viscosity, $\nu = 10^{-6}$ m^2/s.

Vertical mixing profiles $K_z(z)$ also span the surface-subsurface continuum. Vertical mixing profiles in the water column were determined from experimental observations by invoking the Reynolds analogy, which assumes turbulent momentum transport is equivalent to local eddy diffusivity [*Tennekes and Lumley*, 1972]. Eddy diffusivities were calculated from profiles of Reynolds-decomposed velocities [*Blois et al.*, 2012] according to standard procedures [*Tennekes and Lumley*, 1972; *Fischer et al.*, 1979].

Mixing rates near the interface were determined by fitting modeled concentrations to concentrations measured experimentally from steady-state streambed injections (Chapter 2). The minimum vertical mixing rate in the streambed was assumed to be governed by dispersion in the porous medium [*Bear*, 1979]. The associated dispersion coefficient K_p was determined by fitting the 1-D advection-dispersion equation to subsurface solute injections (Chapter 2). Longitudinal mixing was assumed to be insignificant relative to downstream advection, which is a valid assumption for the flow distribution considered here [*Fischer et al.*, 1979]. Note that this model explicitly resolves longitudinal dispersion at the scale of the stream-subsurface continuum as an outcome of Equations (3.2), so only local longitudinal diffusion in the water column and dispersion in the porewater are omitted.

Table 3.1. Simulation parameters calculated from experiments in Chapter 2.

Re	42,000	21,000	11,000
H (cm)	12.3		
d_b (cm)	-22.4		
Q (L/s)	8.8	4.4	2.2
$\bar{U}_s$ (cm/s)	34.0	17.4	8.8
U_p (cm/s)	1.85	0.63	0.29
$\bar{U}_{HZ}$ (cm/s)	2.1	0.8	0.3
$\bar{U}_s/\bar{U}_{HZ}$	16.5	20.5	30.1
K_p (cm²/s)	0.34	0.20	0.15

We assessed two different hypothesized profiles for K_z in the hyporheic zone (Figure 3.1).

First, we hypothesized that profiles of vertical mixing follow the hyporheic velocity profiles

observed in high-permeability streambeds, which generally show exponential decay with depth

[*Ruff and Gelhar*, 1972; *Zagni and Smith*, 1976; *Mendoza and Zhou*, 1992]. For this model, we

assume that vertical mixing rate decays monotonically into the streambed and exponentially from

the measured eddy diffusivity at the SWI, $K_z(0)$, to the minimum value of K_p at depth:

$$K_z(z < 0) = K_p + \left(K_z(0) - K_p\right)e^{\alpha z}. \tag{3.3}$$

where α is the rate of exponential decay. Hereafter, we refer to this simulation case as

"monotonic decrease."

Second, we hypothesized that mixing is enhanced by turbulence at the SWI, consistent with

profiles of turbulent stresses measured in high-permeability streambeds [*Breugem et al.*, 2006;

Manes et al., 2009; *Manes et al.*, 2011; *Blois et al.*, 2013; *Li et al.*, 2017]. For this model, we

assume enhanced transport at the SWI, K_e, followed by an exponential decay from the SWI to

K_p:

$$K_z(z < 0) = K_p + (K_e - K_p)e^{\alpha z} \qquad (3.4)$$

We refer to this simulation case as "enhanced interfacial transport." For this case, K_e was

allowed to freely vary to fit the observed profiles.
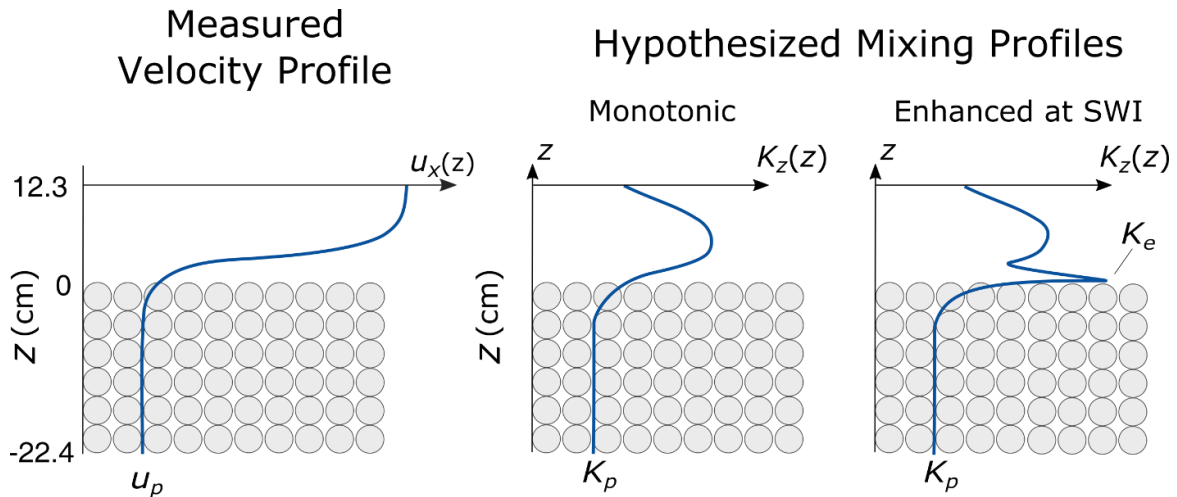
Figure 3.1. Left: Conceptual profile of average longitudinal velocity $u_x(z)$. Velocities were measured from experiments in Chapter 2. u_p is defined as the porewater velocity in streambed, where flows are not altered by surface-subsurface flow coupling. Right: Hypothesized profiles of vertical mixing, $K_z(z)$. The sediment water interface (SWI) and $z = 0$ are defined as the top of the upper-most sediment grains. Profiles decay exponentially below the SWI. K_e is the mixing rate at the SWI for profiles with enhanced mixing, and K_p is the porewater mixing rate measured from Chapter 2 experiments.

The particle tracking model was parameterized with each hypothesized profile, with the

objective of finding model parameters that best fit observations of time-averaged concentration

profiles from steady-state tracer injection experiments (Chapter 2). Two injection locations were

simulated for each profile, matching conditions used in experiments: a "surface injection" at

$(x, z) = (0,-0.6)$ cm, and a "subsurface injection" at $(x, z) = (0,-8.2)$ cm. Experimental and

simulated concentrations were measured at a downstream location $x = 47.6$ cm and at elevations

of $z = $ -0.6, -4.4, -8.2, -12.0, -15.8, and -19.6 cm.

Solute mixing was simulated with one hundred virtual particles and timesteps of $\Delta t = 0.01$s.

Simulations at smaller Δt did not alter model results. Boundary conditions at $z = d_b$ and $z = H$

were fully reflective. The objective fitting function was chosen to match both subsurface

concentrations and the overall fraction of mass retained in the bed, according to the following

equation:

$$SSE \ = \ \sum_{i=1,2} \left(\sum_z \left(C_{E,i,z} - C_{M,i,z} \right)^2 + 2 \left(f_{E,i} - f_{M,i} \right)^2 \right) \tag{3.5}$$

Here, SSE is the sum of squared errors, $C_{X,i,z}$ is the experimental (E) or modeled (M) solute

concentration measured at elevation z; and $f_{X,i}$ is the fraction of injected mass retained in the

streambed. These fits were performed for all tracer injection locations, i, used in the

experiments. Inclusion of $f_{X,i}$ in (3.5) ensured that model fits respected observed mass exchange

with the water column, and this term was given a weighting factor of 2 to ensure that mass

exchange was weighted greater than any individual concentration measurement.

Model fits were used to calculate the mixing rate in the region of enhanced turbulent

porewater transport $\overline{K}_I$, defined as the mean mixing rate between the SWI and the maximum

depth of enhanced mixing z_i. This depth was defined as the location where the mixing rate was

1% greater than the underlying porewater dispersion K_p:

$$\frac{K_z(z_i)}{K_e - K_p} = 0.01 \qquad\qquad (3.6)$$

3.2.2 Reach-scale simulations

Pulse injections of a conservative solute were simulated by particle tracking using each of the two hypothesized K_z profiles: the monotonic decrease into the bed, and the enhanced interfacial transport. Two additional simulations were performed for comparison: a uniform hyporheic mixing rate ($K_{z<0} = K_p$), and an impermeable streambed. Note that no monotonic model fit was made for the low flowrate, since interfacial mixing rates were nearly equal to K_p at this flowrate, making the monotonic decrease profile equivalent to the profile used for the uniform hyporheic mixing model.

For each simulation, 192,000 particles were released uniformly over the water column at $x = 0$ and monitored for 200,000 s. Streambed depth was set at $d_b = 1$ m to avoid depth constraints on the porewater velocity profile. Two breakthrough curves (BTCs) were determined as the temporal evolution of the average water-column concentration in a 20-m-long streambed section centered at 250 m and 1 km downstream. Lagrangian statistics of plume transport (mean and variance) were also calculated directly from the space-time distributions of virtual tracer particles.

Simulation results were used to calculate several metrics associated with solute mixing and transport. The advective hyporheic timescale was taken as the time required to traverse a characteristic longitudinal distance L while traveling at the mean porewater velocity $\bar{U}_{HZ}$:

$$\tau_T = L/\overline{U}_{HZ}. \tag{3.7}$$

The timescale of vertical hyporheic mixing, τ_{bed}, was defined as:

$$\tau_{bed} = d_b^2/\overline{K}_{HZ}. \tag{3.8}$$

A streambed depth d_b = 1 m ensured that the zone of interfacial mixing was limited to a small

proportion of the bed, and $K_p \sim \overline{K}_{HZ}$. This choice allowed for a single τ_{bed} to be used for the

analysis, chosen from the best-fit profile with enhanced interfacial transport.

An outcome of the normally-distributed noise prescribed for vertical mixing (Equation (3.2))

is that a particles entering an unconstrained streambed (i.e., infinite length and depth) will return

to the SWI at time t with probability $p(t) \sim t^{-1/2}$ [*Feller*, 2008; *Aquino et al.*, 2015]. If (1)

velocity scales and associated travel time scales between the stream and hyporheic zone are

assumed to be sufficiently separated, and (2) vertical mixing in the streambed occurs at a

uniform rate $\overline{K}_{HZ}$, the residence time distribution (RTD) for the study reach approaches this

return-time distribution. Consequently, breakthrough curves (BTCs) of in-stream concentrations

will be proportional to $t^{-1/2}$ at late times for a streambed that is dominated by a uniform mixing

regime in the subsurface (i.e., $K_p \sim \overline{K}_{HZ}$).

The timescales associated with the finite reach length and bed depth impose constraints that

modify the RTD for the reach. The advective hyporheic timescale corresponds to the longest

time a particle is expected to traverse the reach and thus represents a truncation of the RTD at τ_T.

Further, τ_{bed} represents the slowest mixing timescale in the domain and thus is a predictor of the

Gaussian setting timescale, defined as the time at which a longitudinally spreading tracer will

evolve according to Fick's Law [*Fischer et al.*, 1979; *Zhang and Meerschaert*, 2011]. The combination of these behaviors suggests that solute RTDs at the reach scale will follow $p(t) \sim t^{-1/2}$ at late times with exponential decay (tempering) after the minimum of τ_T and τ_{bed}.

Simulation results were compared with predictions from both the fractional-order mobile-immobile model (FMIM) [*Schumer et al.*, 2003] and the ADE. The FMIM is a reduced-order (1-D in space) analytical model that parses the stream into a mobile (water column) zone and an immobile (hyporheic) zone where mass is assumed to be motionless. Immobile mass also is assumed to randomly and independently sample a wait-time from a power-law distribution $p(t) \sim t^{-\gamma}$ before it returns to the mobile domain. Asymptotic solutions for the FMIM predict that concentrations in the water column at late times will follow a power law with $C(t) \propto t^{-(1+\gamma)}$, or $C(t) \propto t^{-3/2}$. To compare to this expected BTC slope, simulated concentrations were calculated as:

$$m = \Delta(\log C)/\Delta(\log t) \qquad (3.9)$$

Calculated values of m were then smoothed using a 40-point moving average algorithm.

ADE model predictions were used to evaluate the rate at which the plume transitioned to a Fickian transport regime, in which the mean plume distance scales linearly with time. Additionally, the coefficient of longitudinal Taylor dispersion K_L scales with longitudinal plume variance, σ^2, as [*Elder*, 1959]:

$$K_L = \sigma^2 / 2t, \tag{3.10}$$

meaning the variance also scales linearly with time according to ADE theory. Values for K_L were estimated in each simulation after the trends had transitioned to a regime of linear scaling.

3.3 Results

3.3.1 Hyporheic mixing profiles

Experimental and modeled concentration profiles are shown for each flowrate and mixing profile in hyporheic mixing profiles for each each flowrate and mixing profile in Figure 3.2. The monotonic profile did not capture the enhanced mass exchange across the SWI. Attempts to better match concentrations near the SWI resulted in under-predictions of overal mass retention. As a result, best fits for this model only reasonably described porewater solute concentrations at depth in the bed ($z >$-8 cm, and over-predicted concentrations near the SWI.

Results improved substantially in simulations using the enhanced interfacial transport profile Model simulations better matched the observed concentration profiles (Figure 3.2), particularly near the SWI. The decay rate of mixing in the bed, α, was similar for Re = 21,000 and 42,000, but increased for the Re = 11,000 case, indicating a thinner zone of enhanced mixing under the lowest flowrate.
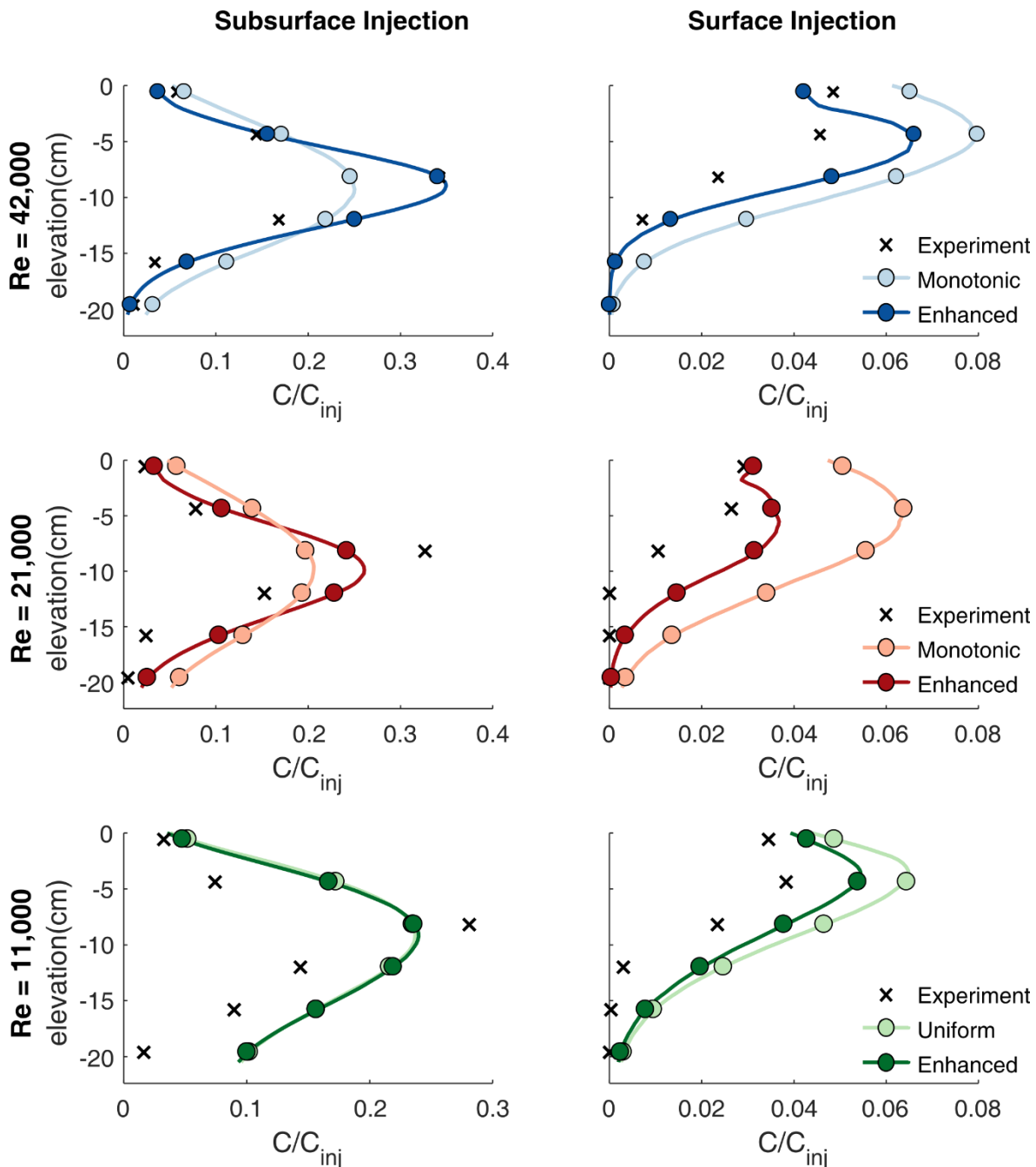
Figure 3.2. Observed and simulated steady-state tracer injection concentration profiles in the hyporheic zone.

Table 3.2. Model fits of K_e and α to experimental results. Additional parameters calculated from these fits are also reported. Experimental results are from Chapter 2.

Re	--	42,000	21,000	11,000
SSE	Monotonic	0.082	.157	--
	Enhanced	0.047	0.064	0.156
α	Monotonic	0.11	0.09	--
(1/cm)	Enhanced	0.74	0.75	2.00
$K_{z=0}$	Monotonic, $K_z(0)$	1.55	0.71	--
(cm²/s)	Enhanced, K_e	9.66	5.00	3.75
	Experiment	0.10	0.05	0.08
$f_{surface}$	Monotonic	0.23	0.21	--
	Enhanced	0.15	0.10	0.10
	Experiment	0.72	0.78	0.61
$f_{subsurface}$	Monotonic	0.84	0.60	--
	Enhanced	0.85	0.73	0.87
z_i (cm)	Monotonic	-41.9	-51.2	--
	Enhanced	-6.2	-6.1	-2.3
	Monotonic	0.60	0.31	--
$\bar{K}_i$ (cm²/s)	Enhanced	2.04	1.06	0.42
	Uniform	0.34	0.20	0.16
	Monotonic	0.45	0.26	--
$\bar{K}_{HZ}$ (cm²/s)	Enhanced	0.47	0.27	0.17
	Uniform	0.34	0.20	0.15
$\tau_{bed} = d_b^2/\bar{K}_{HZ}$ (×10⁴ s)	--	2.1	3.8	5.7
$\tau_T = L\bar{U}_{HZ}$	$L = 250$ m	1.4	4.0	11.9
(×10⁴ s)	$L = 1$ km	5.4	15.9	47.6

3.3.2 Reach-scale simulations

Simulated breakthrough curves (BTCs) for the monotonic and enhanced interfacial transport

mixing models are shown for downstream distances of 250 m and 1 km in Figure 3.3. Several

similar features are observed in each BTC.

1. Distinct tracer peak.
2. Exponential decrease in tracer concentration after the peak (note that these appear as a convex curve in the log-log plots).
3. Power law tailing over a finite interval (appear as straight lines in the log-log plot).
4. Exponential tempering of the power-law at late time.
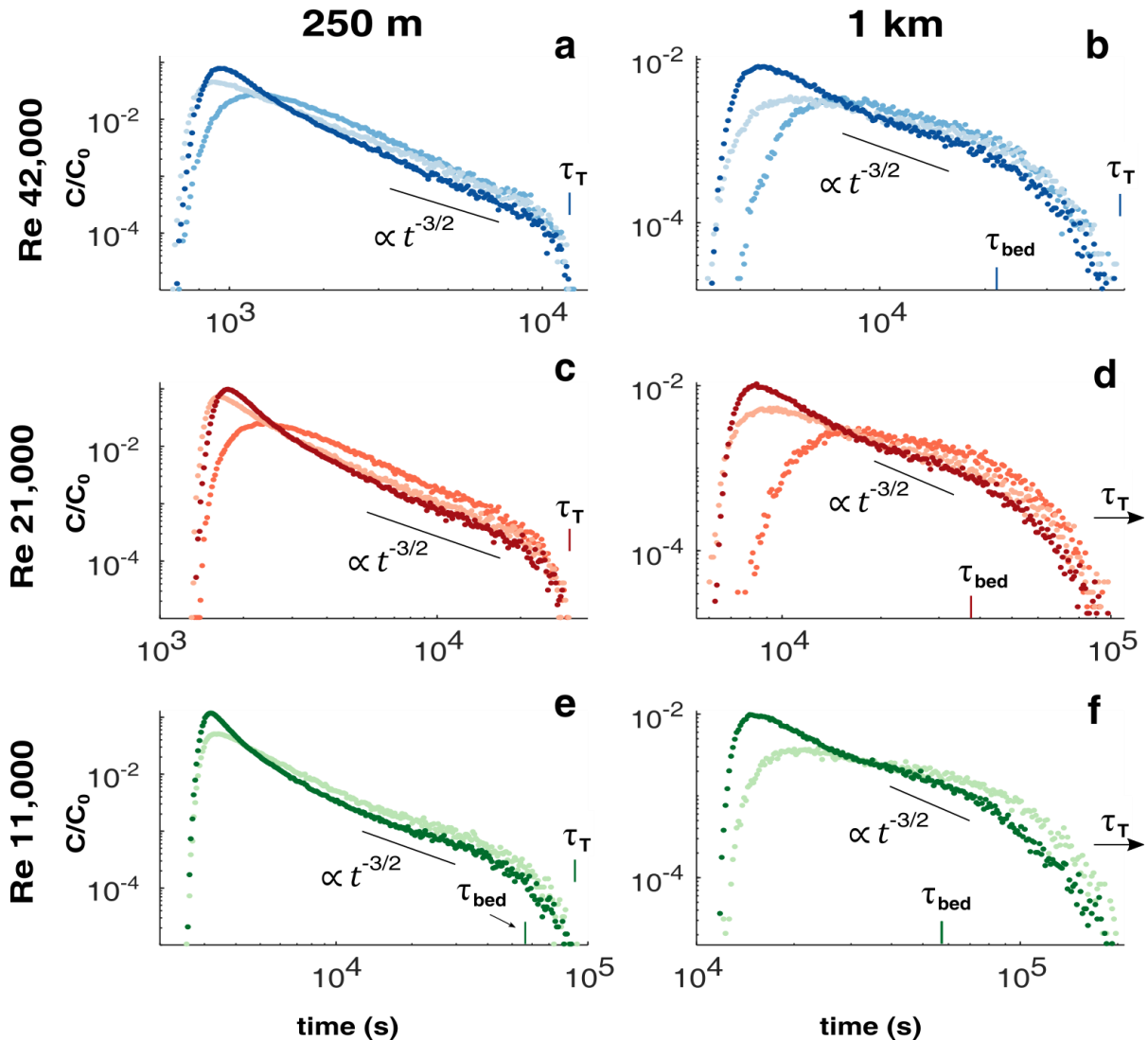
Figure 3.3. Simulated breakthrough curves for monotonic decrease model (medium hue), enhanced interfacial transport model (dark hue), and uniform hyporheic mixing (light hue). Note that axes of each plot are scaled differently to most clearly illustrate the shape of each breakthrough curve.

Arrival and decay of the concentration peak did not vary predictably with downstream distance, particularly at early times. This behavior is illustrated in the sequence of BTC arrival at $Re = 42,000$. Arrival order at the 250 m location was: uniform hyporheic mixing model, enhanced interfacial transport model, monotonic decrease model. By 1 km this order had

changed to: enhanced interfacial transport model, uniform hyporheic mixing model. Similar

nonlinear trends were also observed in values for concentration peaks. Concentrations decayed

most rapidly at early times in simulations with uniform hyporheic mixing (Figure 3.4, light

symbols), but these decay rates slowed after 1 h. Asymptotic peak concentrations directly

corresponded to the average rate of interfacial mixing between $z = 0$ and z_i. The early-time

trends are attributed to mass just below the SWI being rapidly flushed back into the water

column. This result is consistent with the vertical concentration profiles, which showed depleted

interfacial concentrations in simulations with enhanced interfacial transport.
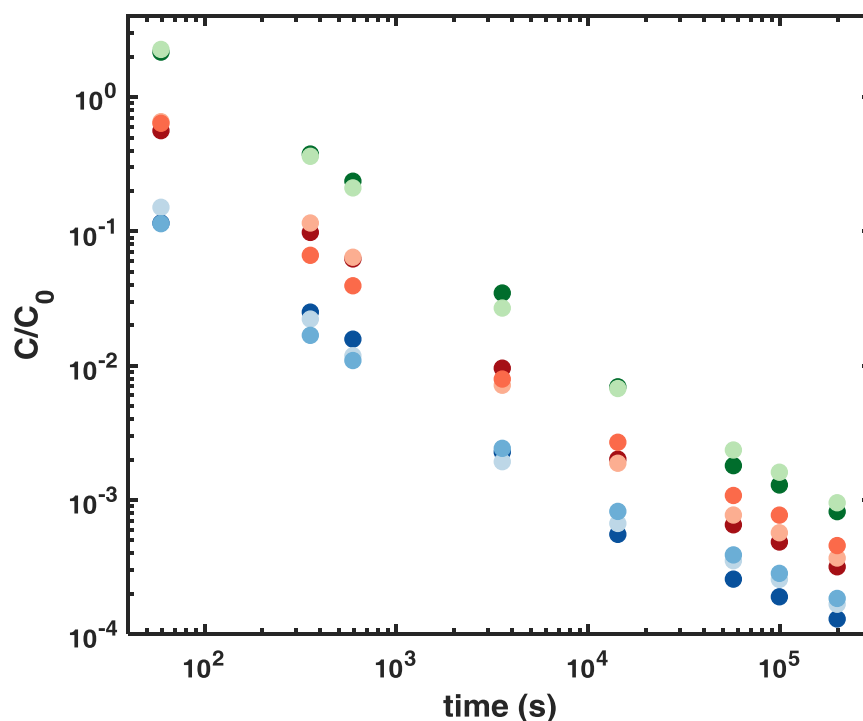
Figure 3.4. Peak concentration of each plume. Colors correspond to plots in Figure 3.3. Values for middle and low flows are shifted by a factor of 2 to emphasize patterns.

The exponential and power-law BTC tailing regimes also varied with mixing profile and flowrate. BTCs for simulations with a uniform mixing profile transitioned to power-law tailing earlier than the monotonic decrease and enhanced interfacial transport models. For example, the 250-m BTC at Re = 42,000 exhibited power-law tailing at $t \approx$ 1400-7200 s for the uniform mixing model, while the monotonic decrease and enhanced interfacial transport models showed tailing at $t \approx$ 2600-7200 s (Figure 3.3).

Hyporheic RTDs for each simulation matched predictions, exhibiting a power-law tail with $p(t) \sim t^{-1/2}$ and exponential tempering after τ_{bed} (see Supporting Information). However, calculated BTC tail slopes differed from the predicted scaling of $m \propto t^{-3/2}$ (Figure 3.5). The BTC tails for each mixing model converged to the same slope at L = 250 m (Figure 3.5a,c) before τ_{bed} or τ_T was reached. Slopes converged at $t \approx \tau_{bed}$ or not at all for BTCs at L = 1 km (Figure 3.5b,d).
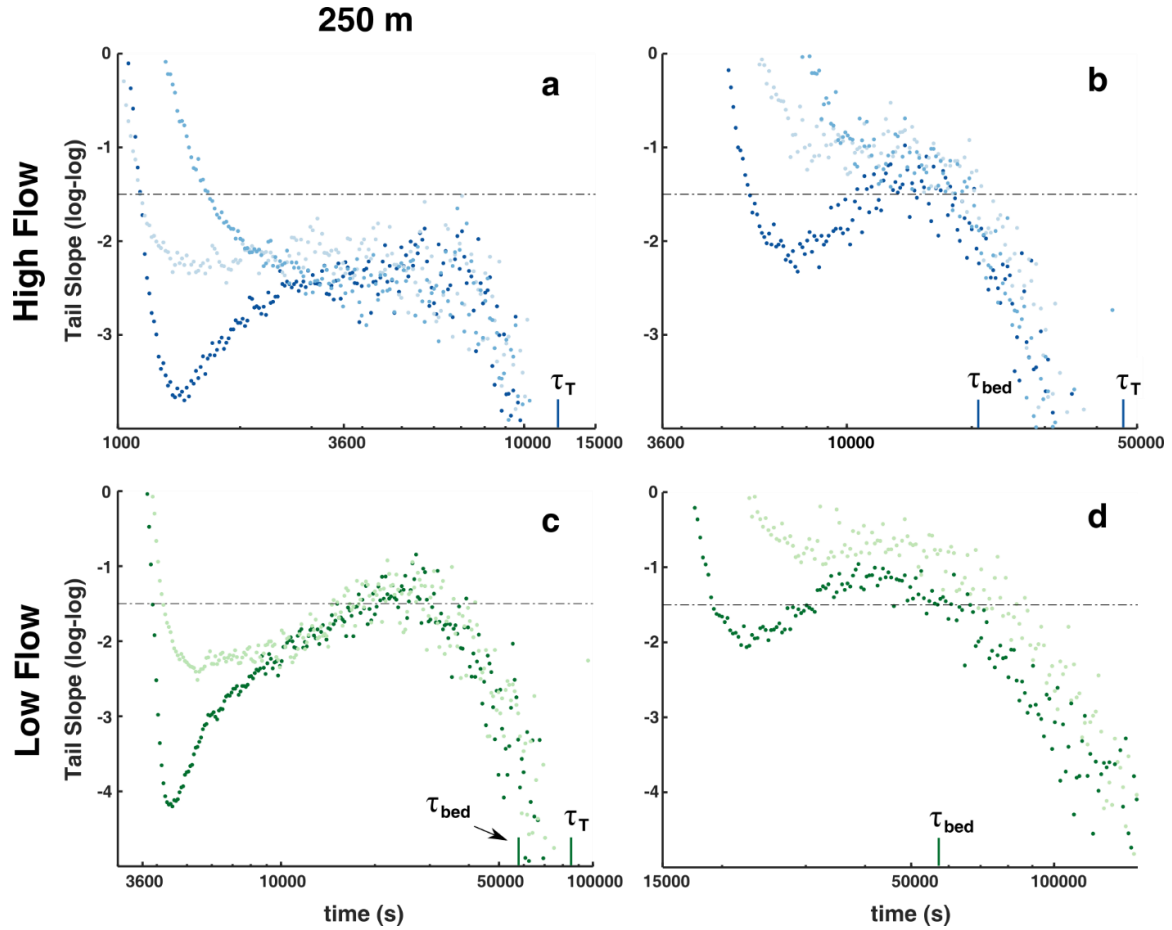
Figure 3.5. Tail slopes m for high- and low-flowrate BTCs reported in Figure 3.3. Dashed line represents the predicted asymptotic scaling, $C(t) \propto t^{-3/2}$. A tail slope of zero signals the passing of peak concentration.

A final exponential tempering to a regime of rapidly decaying concentrations was observed for all BTCs. The nature of the tempering was determined by the truncation timescale associated with the longitudinal hyporheic velocity deep in the bed, τ_T, and the characteristic timescale for vertical mixing over the full depth of the streambed, τ_{bed}. Truncation results in a sharp exponential decay in the BTC at $t = \tau_T$ (Figure 3.3a,c), as well as a sharp decay in tail slope before $t = \tau_T$ (Figure 3.5a,c). This behavior can be seen in the $Re = 21,000$ and $42,000$

simulations for reach length $L = 250$ m (Figure 3.3a,c). This represents a true truncation of the power-law BTC tail, as there is a sharp cutoff at the maximum residence time set by advective longitudinal washout of tracer mass from the hyporheic zone (τ_T). In contrast, Gaussian setting (transition to a regime of Fickian transport) occurs when tracer fully samples the velocity distribution over the entire stream-hyporheic continuum, i.e., the time at which the tracer becomes well-mixed between the stream and the bed (τ_{bed}). Gaussian setting manifests as slower exponential tempering in the BTCs for the middle- and low-flow conditions at $L = 1$ km (Figure 3.3d,f) at $\tau_{bed} \approx 38{,}000$ s and $57{,}000$ s, respectively.

The dominant process that controls tempering of the power-law BTC tail can be assessed as the ratio of the advective truncation and Gaussian setting timescales, τ_T/τ_{bed}. Cases with $\tau_T \gg \tau_{bed}$ show broad exponential tempering associated with Gaussian setting ($\tau_T/\tau_{bed} = 3.1$ and 5.9, respectively, for the BTCs that exhibit slow tempering in Figure 3.3d,f). Conversely, cases with $\tau_T \ll \tau_{bed}$ show much steeper exponential BTC tempering consistent with a truncation in the hyporheic residence time distribution (Figure 3.3a,c). Intermediate cases show exponential tempering of the BTC tail at τ_{bed} followed by a steeper exponential at τ_T (Figure 3.3b,e, tempering at $57{,}000$ s and $21{,}000$ s, with $\tau_T/\tau_{bed} = 2.6$ and 2.1, respectively).

Distinct transport regimes are also visible in the Lagrangian plume statistics (Figure 3.6). Mean velocities were nearly identical and linear early after the pulse injections, and then slowed nonlinearly after several hundred seconds. Mean velocities continued to decrease until they reached an asymptotic scaling regime that scaled approximately as $\overline{U}_s \sim t^{0.9}$. This regime was

followed by a transition to linear ($\overline{U}_s \sim t^1$) scaling at $t \approx \tau_{bed}$ (Figure 3.6a). The transition to linear scaling was quickest for the enhanced interfacial transport profile, with a slightly later transition for the monotonic decrease and uniform mixing profiles. The onset of this transition also decreased increased with increased Re.
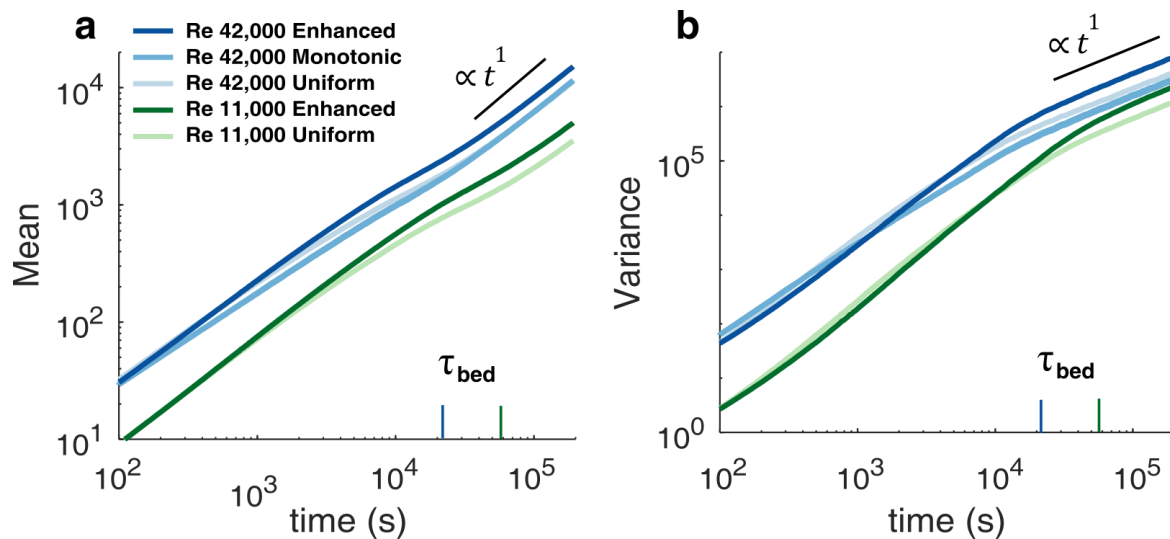
Figure 3.6. Trends in plume mean (a) and variance (b) for simulations at high (blue) and low (green) flows. Enhanced interfacial transport model (dark hue). Monotonic model (middle hue). Uniform hyporheic mixing model (light hue). The middle flowrate, not shown for clarity, exhibited trends in between the low and high flow cases. Both trends show a transition to nonlinear to linear scaling ($\propto t^1$) at $t \approx \tau_{bed}$; linear scalings are provided in each plot for comparison. Note that a greater *y*-intercept on a log-log plot corresponds to a greater slope for linear trends. Late-time trends in (b) that are shifted upward therefore have a greater longitudinal dispersion coefficient, per Equation (3.10).

Similarly, relaxation to $\sigma^2 \propto t$ scaling occurred earliest for $Re = 42,000$ simulations, and increased with decreasing flowrate. The quicker transition is due to tracer mass more rapidly sampling all transport timescales for this mixing profile, indicated by a smaller vertical mixing timescale τ_{bed} at the higher flowrate (Table 3.2, Figure 3.6b). Calculated values for longitudinal dispersion K_L were greatest for simulations with the enhanced interfacial transport mixing profile

(Table 3.3, Figure 3.6b). This result was expected because this profile shows the greatest

variability in mixing rates. Further, it shows that turbulent hyporheic mixing ultimately results in

greater longitudinal spreading of a tracer plume. The smoother transition in mixing rates from

the water column to the hyporheic zone reduced the variability in mixing rates for the monotonic

profile, compared to the uniform mixing and enhanced interfacial transport models. As a result,

K_L values were lowest for the monotonic decrease model.

Table 3.3. Longitudinal dispersion coefficients calculated from Equation (3.10).

Re	--	42,000	21,000	11,000
	Uniform	19.5	15.1	5.6
K_L (m^2/s)	Monotonic	15.1	6.8	--
	Enhanced	37.2	22.0	10.6

3.4 Discussion

Turbulent coupling between surface and porewaters creates a localized zone of enhanced

hyporheic mixing immediately below the SWI. We show that the spatial variability of mixing

within this zone directly controls concentrations and interfacial exchange rates at the grain scale,

as well as downstream transport at the reach scale (> 1 km). Vertical concentration profiles

observed in 0.5-m solute injection experiments were best described by a profile with enhanced

mixing intensity at the SWI and exponential decay to uniform mixing deep in the hyporheic

zone.

Particle-tracking simulations show that several processes control downstream solute transport.

Enhanced mixing at the SWI results in faster solute exchange between the water column and the

shallow hyporheic zone (i.e., $z_i \leq z \leq 0$). Solute that enters this zone is either rapidly flushed to the water column or delivered to deeper, slower moving porewaters. Sampling of vertical mixing rates is therefore highly variable for this profile, resulting in nonlinear trends for the arrival of the plume peak and plume mean velocity (Figure 3.3 and, Figure 3.6, respectively). Simulations with higher interfacial turbulence also exhibited a later-time transition to a power-law scaling regime (Figure 3.3). A necessary condition for a stream BTC to exhibit power-law scaling is that transported mass must sample a broad range of time scales [*Haggerty et al.*, 2000; *Haggerty et al.*, 2002; *Schumer et al.*, 2003; *Berkowitz et al.*, 2006]. A longer transition to power-law scaling implies that tracer samples a distribution of hyporheic velocities overlaps with in-stream velocities, resulting in a continuous distribution of transport timescales. Mass that enters the thin zone of enhanced mixing (between the SWI and z_i) returns to the mobile zone with high probability, and longer times are required for mass to adequately sample the slow velocities associated with deeper hyporheic water. In contrast, simulations with uniform subsurface mixing retained more mass near the SWI, allowing mass to sample slow-moving hyporheic waters more frequently at earlier times.

   Late-time BTC concentrations generally did not follow the scaling predicted from the fractional mobile-immobile model (FMIM), which links the local heavy-tailed hyporheic residence time distribution (RTD) to downstream transport [*Schumer et al.*, 2003]. Although RTDs in the streambed scaled with $t^{-1/2}$ over a broad range of times (see Supporting Information), BTCs did not scale with $t^{-3/2}$ over these times according to the FMIM. Tail slopes

only approached a power law for observations at $t < \tau_{bed}$ (the Gaussian setting time) and $t < \tau_T$ (the truncation time associated with tracer mass exiting the reach by downstream advection through the hyporheic zone). The ratio τ_T/τ_{bed} also determined the shape of late-time BTC tempering.

Application of the FMIM and other stochastic models is therefore limited in high permeability streambeds. The expected duration of asymptotic (power-law) tailing is limited by reductions in both the advective truncation timescale, τ_T, due to higher longitudinal hyporheic velocities, and the Gaussian setting time, τ_{bed}, due to more rapid vertical mixing within the bed. In addition, high hyporheic velocities result in the migration of mass a substantial distance downstream in the hyporheic zone, which results in correlations between transport events in this zone [*Li et al.*, 2017]. Events therefore cannot be treated as independent and identically distributed, which is a commonly-invoked assumption in the derivation of stochastic transport models for hyporheic exchange [*Boano et al.*, 2014]. This requires further generalization of stochastic models to capture the pre-asymptotic solute transport behavior observed at earlier times in coarse-bed streams. Recent numerical and groundwater studies have confirmed that velocity decorrelation timescales provide key information for determining pre-asymptotic plume evolution [*Kang et al.*, 2011; *Kang et al.*, 2015]. Spatial Markov models have successfully utilized velocity correlation information to predict pre-asymptotic transport [*Le Borgne et al.*, 2008; *de Anna et al.*, 2013; *Bolster et al.*, 2014; *Sund et al.*, 2015; *Dentz et al.*, 2016]. This type of approach may be useful for predicting early time transport behavior for highly-permeable riverbeds if the timescales of velocity decorrelation in the hyporheic zone are properly determined.

The final decay in BTC concentrations is also controlled by τ_T/τ_{bed}. Gaussian setting, marked by slow exponential tempering, is the dominant decay process when the downstream hyporheic transit time sufficiently exceeds the vertical hyporheic mixing timescale, τ_{bed}, which was found to occur only for $\tau_T/\tau_{bed} > \sim 2$. Turbulent hyporheic mixing reduced the thickness of the hyporheic zone characterized by power-law residence times. However, the small thickness of the zone of enhanced mixing relative to the bed depth ($z_i/d_b \leq 0.06$) implies that enhanced interfacial mixing is only a second order control on long vertical mixing timescales for deeper beds (Figure 3.3, 1 km BTCs), and exerts a much greater control on BTCs by increasing downstream hyporheic velocity and thereby reducing τ_T. BTCs in reaches with lower τ_T/τ_{bed} were characterized by sharp BTC tempering as mass exited the stream reach via downstream hyporheic advection, whereas reaches with higher τ_T/τ_{bed} were characterized by more gradual BTC tempering. The late-time shape of BTCs may therefore clarify interpretation of which timescale dominates plume behavior in the field [*Aubeneau et al.*, 2014], provided signal-to-noise ratios are sufficiently high to enable discrimination of the late-time tailing behavior [*Drummond et al.*, 2012].

The shape of the enhanced interfacial transport profile is not expected to exactly match the shape of profiles in real systems. Instead, it represents a minimally parameterized profile that captures key features of turbulent stress profiles observed for flows over very permeable streambeds. These features include enhanced stresses at the SWI and exponential decay of stresses in the streambed [*Breugem et al.*, 2006; *Manes et al.*, 2009; *Manes et al.*, 2011; *Blois et*

al., 2013; *Voermans et al.*, 2017]. Model fits to experimental injections show that the region of the streambed where enhanced mixing is found (i.e., SWI to z_i) corresponds to the region where turbulent stresses and high-frequency concentration fluctuations are observed (Chapter 2). This result suggests that high-frequency measures of subsurface concentration can be used to estimate z_i. Although field measurements of mass transport at turbulent timescales are currently limited by available sensing technology, recent numerical simulations [*Chandesris et al.*, 2013] and laboratory experiments (Chapter 2) show the existence of low-frequency (~10-100s) concentration oscillations just beyond the streambed depth where turbulent stresses are observed. Detection of low-frequency oscillations in the streambed may help identify regions of enhanced mixing.

Our findings add to a growing literature that confirms interfacial momentum transport directly controls mixing in highly-permeable porous media [*Nagaoka and Ohgaki*, 1990; *Packman et al.*, 2004; *Lightbody and Nepf*, 2006; *Poggi et al.*, 2006; *Nepf et al.*, 2007; *O'Connor and Harvey*, 2008; *Chandesris et al.*, 2013; *Chandler et al.*, 2016]. Further, we demonstrate that this control extends to the reach scale. A mechanistic understanding of turbulent momentum transport is therefore essential for inferring hyporheic residence times from solute injections. Recently-developed scaling relations for interfacial momentum transport have shown promising ability to predict characteristics of interfacial turbulence based on measurable system properties (e.g., permeability, shear stress), and may be valuable predictors of mass transport at both the local and reach scales [*Ghisalberti*, 2009; *Manes et al.*, 2012; *Voermans et al.*, 2017]. Future research is needed to validate the applicability of available scaling relationships to predict turbulent mass

transport in high permeability streambeds. This will require simultaneously measuring hyporheic momentum and mass transport at turbulent frequencies. Such efforts will provide a direct means to assess both the range of natural settings where hyporheic turbulence is important, as well to parameterize turbulent hyporheic exchange in upscaled models for solute transport in rivers

3.5 Supporting information
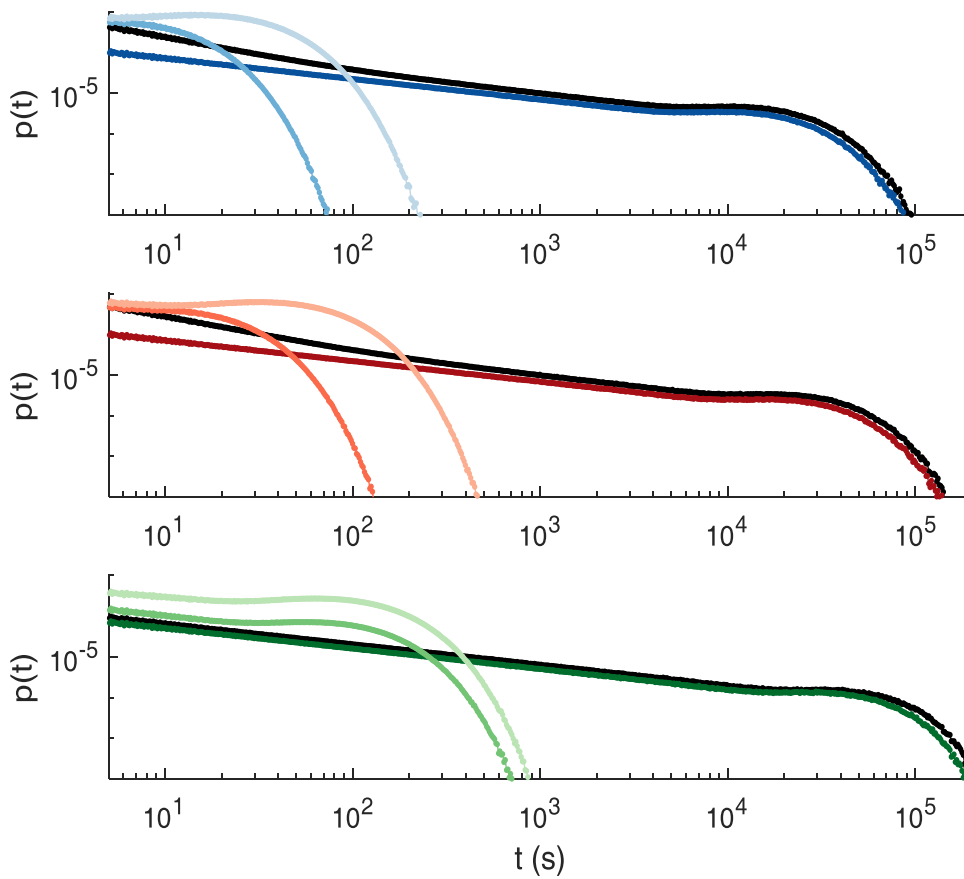
Figure 3.7. Residence time distributions for various subdomains in the simulation. Entire hyporheic zone (black line). Hyporheic zone below z_i (dark hue). Region between z_i and the SWI (middle hue). Mobile zone (light hue). Residence times in the interfacial layer are exponentially distributed and shorter than mobile zone residence times. The slope of the power-law is proportional to $\sim t^{-1/2}$ in all plots.

CHAPTER 4

Benthic Biofilm Controls on Fine Particle Dynamics in Streams*

ABSTRACT

Benthic (streambed) biofilms metabolize a substantial fraction of particulate organic matter and nutrient inputs to streams. These microbial communities comprise a significant proportion of overall biomass in headwater streams, and they present a primary control on the transformation and export of labile organic carbon. Biofilm growth has been linked to enhanced fine particle deposition and retention, a feedback that confers a distinct advantage for the acquisition and utilization of energy sources. We quantified the influence of biofilm structure on fine particle deposition and resuspension in experimental stream mesocosms. Biofilms were grown in identical 3-m recirculating flumes over periods of 18-47 days to obtain a range of biofilm characteristics. Fluorescent, 8-μm particles were introduced to each flume, and their concentrations in the water column were monitored over a 30-minute period. We measured particle concentrations using a flow cytometer and mesoscale (10 μm to 1 cm) biofilm structure using optical coherence tomography. Particle deposition-resuspension dynamics were determined by fitting results to a stochastic mobile-immobile model, which showed that retention timescales for particles within the biofilm-covered streambeds followed a power-law residence time distribution. Particle retention times increased with biofilm areal coverage, biofilm roughness, and mean biofilm height. Our findings suggest that biofilm structural parameters are key predictors of particle retention in streams and rivers.

4.1 Introduction

The streambed is a highly reactive habitat of stream ecosystems. Here, biogeochemical transformations are largely driven by sediment-attached and matrix-enclosed microbial communities, called biofilms [*Jones and Mulholland*, 1999; *Fellows et al.*, 2006; *Battin et al.*, 2008; *Battin et al.*, 2016]. Biofilms control critical ecosystem processes, provide entry for organic carbon into the stream food web, and influence the amount and lability of carbon exported downstream [*Battin et al.*, 2008; *Tank et al.*, 2010; *Battin et al.*, 2016]. Abiotic features of streams (e.g., flow, streambed topography) are traditionally used to parameterize in-stream transport models, while biofilms are generally assumed to control only the transformation of reactive constituents (e.g., organic carbon and nutrients). However, there is growing experimental evidence that shows benthic biofilms modify water flow [*Nikora*, 2010; *Marion et al.*, 2014] and nutrient retention [*Battin et al.*, 2003a; *Bottacin-Busolin et al.*, 2009; *Aubeneau et al.*, 2016] close to the streambed. This feedback may have implications for carbon fluxes in stream networks, since reactions largely occur at the sediment-water interface [*Jones and Mulholland*, 1999; *McClain et al.*, 2003; *Boano et al.*, 2014]. Biofilm-transport interactions are, therefore, critical but missing components of upscaled reactive transport models in streams.

Fine particulate organic matter (FPOM, <10 μm) are important sources of energy in streams and rivers [*D C Richardson et al.*, 2013]. Such particles derive from leaf litter and woody debris and from dissolved organic matter (DOM) that is adsorbed to soil and mineral particles. In streams, extracellular enzymes expressed by microbial heterotrophs in biofilms hydrolyze FPOM

into its dissolved constituents, which then can be taken up and metabolized [*D C Richardson et al.*, 2013]. Factors such as enzyme concentration, particle size, and the degree of organo-mineral complexation can reduce reaction efficiency [*Dimock and Morgenroth*, 2006; *Hunter et al.*, 2016]. FPOM can be remobilized before they are completely degraded, illustrating the dependence of FPOM metabolism on particle delivery and retention at the streambed and its biofilms [*Battin et al.*, 2003a; *Allan and Castillo*, 2007].

Particles deposit and resuspend episodically as they move through streams [*Cushing et al.*, 1993; *Newbold et al.*, 2005; *Harvey et al.*, 2012; *Boano et al.*, 2014; *Drummond et al.*, 2014a]. In a well-mixed stream, particle deposition can be described by a first-order removal rate, which is generally reported as a deposition velocity, v_{dep} [*McNair and Newbold*, 2012]. This velocity typically exceeds the gravitational settling velocity predicted by Stokes' Law for small (<160 µm) particles [*Thomas et al.*, 2001]. Particle resuspension is governed by a number of processes, resulting in a wide distribution of particle retention times. Turbulent eddies resuspend particles on the order of seconds by generating intermittent shear stresses at the streambed [*Ninto and Garcia*, 1996; *Niño et al.*, 2003; *Soldati and Marchioli*, 2009]. Long-term retention (hours to months) is attributed to a combination of biological trapping and deeper sequestration within the stream sediments [*Newbold et al.*, 2005; *Arnon et al.*, 2010; *Harvey et al.*, 2012; *Drummond et al.*, 2014b].

Fluvial transport models have evolved to accommodate the wide range of particle residence times in streambeds. *Drummond et al.* [2014a] extended a continuous time random walk model,

developed for solutes [*Boano et al.*, 2007], and showed that particle residence time distributions (RTDs) follow a power law in streambeds. This mobile-immobile model conceptualizes particle transport as a series of discrete displacements and waits, which are stochastically represented as displacement-length and wait-time probability distributions. Because it assumes no pre-specified RTD, the mobile-immobile model allows for parameterization of particle transport with distributions based on physical, independently verifiable processes. This allows deposition and resuspension to be parsed more explicitly than prior models, which have either lumped the two processes or parameterized exchange as an idealized transfer of mass between the stream and well-mixed storage zones [*Cushing et al.*, 1993; *Paul and Hall*, 2002; *Newbold et al.*, 2005]. Separation of deposition and resuspension dynamics is a crucial step to improving particle transport models, since these two processes are governed by different mechanisms [*Boano et al.*, 2014; *Aubeneau et al.*, 2015b]. *In situ* observations of deposition and resuspension events remains an experimental challenge. Consequently, particle deposition and resuspension parameters are typically estimated from fits to in-stream particle concentrations and constrained by physical process models or independent observations, such as particle retention in sediments [*Drummond et al.*, 2014a; *Drummond et al.*, 2014b].

Biofilms can substantially alter local environmental conditions on and within the streambed [*Battin et al.*, 2016]. The biofilm extracellular polysaccharide matrix is a sticky substance that increases particle trapping, potentially retaining particles until the microbial community is remobilized by dispersal or scour [*Lock and Williams*, 1981; *Sutherland*, 2001; *Boulêtreau et al.*, 2006; *Vignaga et al.*, 2013; *Marion et al.*, 2014]. Biofilms can also contain long, filamentous

structures called streamers that extend into the turbulent boundary layer [*Stoodley et al.*, 1999; *Besemer et al.*, 2009], and their oscillations interact with the external flow field [*Taherzadeh et al.*, 2012]. Mature biofilms are porous systems with highly variable topography [*Stoodley et al.*, 2002; *Battin et al.*, 2003a]. These contributions to highly heterogeneous biofilm structure modify streambed roughness, which modulates turbulence intensity and solute transport near the streambed [*Larned et al.*, 2004; *Nikora*, 2010; *Larned et al.*, 2011]. In turn, the modified flow field is expected to enhance particle deposition, since particle settling is more likely in a region of low turbulence [*Bouwer*, 1987; *Drury et al.*, 1993b; *Battin et al.*, 2003a].

Flow-biofilm interactions are expected to occur predominantly at vertical scales between 100 µm and 10 cm [*Nikora et al.*, 1998; *Nikora et al.*, 2002; *Larned et al.*, 2004; *Larned et al.*, 2011], which coincides with the scales of biofilm structural heterogeneity [*Morgenroth and Milferstedt*, 2009]. Nonetheless, few experiments have analyzed the influence of biofilm structure on fine particle dynamics across this range of scales, limiting our understanding of which mechanisms control this biophysical feedback. In this study we simultaneously quantified the mesoscale (10 µm to 1 cm) physical structure of benthic biofilms and suspended tracer particle concentrations in stream mesocosms. We fit the measured particle concentrations to a stochastic mobile-immobile model, allowing us to assess the influence of biofilm structure on particle deposition and resuspension dynamics. We hypothesized that benthic biofilms, differing in physical structure and overall streambed coverage, would differentially affect the deposition rate and resuspension probability of fine particles.

4.2 Materials and Methods

4.2.1 Mesocosm Setup

The study consisted of 14 individual experiments. For each experiment, we constructed a recirculating flume with a 300 cm L x 5 cm W x 12 cm H test section. The flume was gravity fed by a 1-L header tank and flowed into a 1-L effluent tank. We used an Eheim compact 1000 aquarium pump (Eheim GmbH & Co KH, Deizisau, Germany), located at the bottom of the effluent tank, to recirculate water to the header tank. The two tanks were connected with 1.25 cm diameter vinyl tubing. The flume slope was adjusted to achieve a uniform water column depth across the entire test section (slope = 0.005). We lined the test section with 5 cm L x 5 cm W x 1 cm H ceramic tiles, which were acid washed and precombusted at 450 $^{\circ}$C for 8 h to remove organic matter. The flume setup is shown in Figure 4.1, and photographs are provided in the Supporting Information.
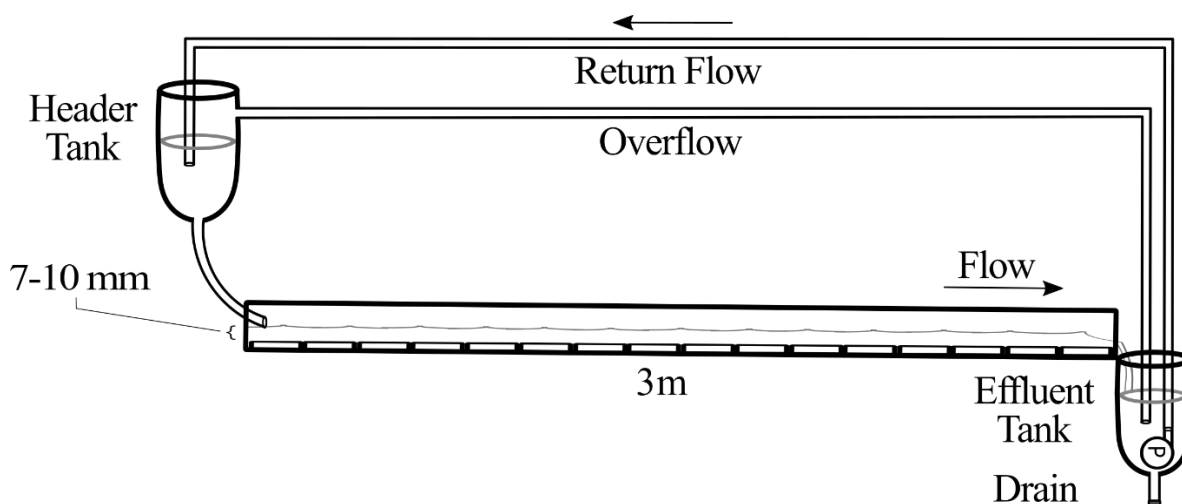
Figure 4.1. Mesocosm setup.

Each experiment consisted of a biofilm growth period, followed by a 30-min period where we injected tracer particles and monitored their concentration in the water column. For the duration of the experiment, we recirculated water from an oligotrophic alpine lake (Lunzer See, Austria). The biofilm growth period ranged from 0 to 47 days across experiments, which allowed for the development of biofilms with a range of structural properties. During the growth period we replaced flume water every second day to ensure adequate carbon and nutrients were available for microbial growth. We replaced water by first draining a small volume of water from the effluent tank. We then added an equivalent volume of replacement water to the effluent tank. These steps were repeated until one flume volume (approximately 3 L) was added. Flumes were located indoors and operated under twelve-hour light : dark cycles. A benthic biofilm formed on the tiles during this period.

4.2.2 Flume hydrodynamics

At the end of the growth period we measured stream depth and flowrate. Flowrate was measured by diverting the return flow to a 1-L graduated cylinder and measuring filling time. We calculated mean flume velocity $U = Q/dw$, where U is mean flume velocity (cm/s), Q is flowrate (cm^3/s), d is water column depth (cm), and w is flume width (cm). Stream Reynolds number is reported as $Re = 4UR_h/\nu$, where ν is the kinematic viscosity of water (cm^2/s). The Froude number is defined as $Fr = U/\sqrt{gd}$, where g is the gravitational constant (9.81 m^2/s). Shear velocity, u^* (cm/s), was calculated using the Colebrook-White equation for free-surface flow (see Supporting Information).

4.2.3 Fine particle release and monitoring

We immediately released a pulse of fine fluorescent tracer particles (EcoTrace, ETS Worldwide Ltd., Helensburgh Scotland) at the end of the growth period. Tracer particles were stained with rhodamine dye. Mean particle diameter was 8.4 ± 7.0 µm and mean particle volume was 25.4 ± 18.6 µm^3 as measured on an EyeTech particle size (Ankersmid, Eindhoven, Netherlands), and their specific gravity was 2.65. Estimated particle settling velocity was 0.044 mm/s, calculated from Stokes' Law. Particles were suspended in 50 mL of a 1 g/L sodium tetraborate solution (dissolved in deionized water) to prevent aggregation. This yielded a slug with 12.4 g/L particle concentration. We agitated this suspension for 30 s and immediately injected it into the flume header tank (Figure 4.1). We then monitored particle concentrations in the water column for 30 min following injection. During this time, we collected water column samples using standard 2-mL tubes inserted into the water column at the flume outlet (before flume water mixed with effluent tank water). We initially collected samples at 5-sec intervals and gradually decreased the sample rate over the course of the 30-min monitoring period (5-sec frequency from 0-2 min; 1 min/2-5 min; 5 min/5-30 min). Samples were immediately refrigerated until particle analysis.

We quantified particle concentrations with a Cell Lab Quanta flow cytometer (Beckman Coulter Inc., Brea, CA, USA). Briefly, water samples were mixed for 60 s using a vortex mixer. 500 µL of sample water was then drawn into the flow cytometer's flow cell at a rate of rate of 60 µL min^{-1} for between 2 and 5 mins (automated duration based on concentration). Particle

concentrations were quantified by measuring fluorescence in the green and orange spectra using the Cell Lab Quanta SC software package. Concentrations were normalized against background autofluorescence of the flume water and verified against detection limits of the instrument, following procedures described in *Drummond et al.* [2014]. We smoothed each concentration time series using a standard moving-window averaging function in Matlab (R2015b, Mathworks Inc., USA), as described in the Supporting Information.

Along with the particles, we co-injected a NaCl solution (50 mL, 100 mS/cm) as a conservative tracer, which we measured as electrical conductivity in the flume effluent tank (WTW Cond 3210, Xylem Inc., Weilheim, Germany). This solute pulse was detectible for 3-4 flume recirculations before fully mixing with the water column. We determined flume recirculation time, t_r, defined as the mean time between successive peaks of the recirculating solute pulse, and the volume of recirculating water in the flume, V_f, via the observed dilution of the solute tracer under well-mixed conditions.

4.2.4 Biofilm physical structure

At the conclusion of the 30-min particle release and monitoring period, we stopped the flow and randomly removed 3 tiles located at least 15 cm (3 tiles) from the flume inlet and outlet sections. Tiles were carefully transferred to petri dishes. Dishes were slowly filled with deionized water until the tile surface was submerged below 1 to 2 mm of water. We imaged 3 random but non-overlapping locations on each tile, resulting in 9 (1 cm x 1 cm) scan areas for each experiment. The biofilm-covered tiles were imaged with a spectral-domain optical

coherence tomography (OCT) microscope (Ganymede, ThorLabs, Newton, NJ, USA), which measures scattered and back-reflected light from an illuminated volume of the sample [*Huang et al.*, 1991; *Xi et al.*, 2006; *Wagner et al.*, 2010]. The microscope records 2-D image slices in the x-z plane (10-μm pixels) at 10-μm intervals in the transverse (y) direction. Note that the particles were smaller than the pixel size and thus could not be resolved individually. Output files were TIFF stacks of 2-D greyscale images in the x-z plane. These files were post-processed using Fiji (ImageJ platform 1.47h) [*Schindelin et al.*, 2012; *Schneider et al.*, 2012] and Matlab (R2015b). We manually straightened each image to assure biofilms were consistently measured from the base of the tile. We cropped the image stacks to minimize variability in light intensity, resulting in an average usable scan area of 3.8 cm^2 per experiment. Lastly, we binarized each image to distinguish biofilms from the water column. A full description of the post-processing procedure is provided in the Supporting Information.

We calculated several biofilm structural parameters from the OCT data to evaluate their influence on particle deposition and resuspension. Mean height measures the average overall height above the tile. We define roughness as the mean magnitude of variations in biofilm height, $\left|H - \overline{\overline{H}}\right|$. Areal coverage is defined as the fraction of tile surface area occupied by biofilm at least 10 μm thick, which is the smallest length scale we could resolve. For this calculation, we assume a unit spacing in the transverse (y) direction equal to the distance between scans (10 μm). All image analysis was performed using 2-D images, and 3-D composite images are provided for illustrative purposes only.

4.2.5 Stochastic model for fine particle deposition/resuspension in biofilms

We adapted the mobile-immobile model for particle transport in streams [*Boano et al.*, 2007; *Drummond et al.*, 2014a] to quantify fine particle dynamics in the recirculating flumes. The model assumes a partitioning of particles between a mobile and an immobile domain, considered to represent the water column and the streambed, respectively. Particle deposition events are mathematically represented as a transfer of particles from the mobile to the immobile domain, while particle resuspension is considered a transfer from the immobile domain to the mobile domain. Particle concentrations are assumed to be spatially uniform in the water column.

A full model derivation is provided in the Supporting Information. In brief, the concentration $C(t)$ of particles in a well-mixed water column is described by the following mass balance:

$$\frac{\mathrm{d}C(t)}{\mathrm{d}t} V_f = -N_{dep}(t) + N_{res}(t)$$

4.1

where V_f is the volume of water in the recirculating flume, and $N_{dep}(t)$ and $N_{res}(t)$ denote the rate of particle deposition and resuspension, respectively (t^{-1}). $N_{dep}(t)$ is a first-order boundary flux to the streambed, governed by a rate constant, Λ (t^{-1}) [*Drummond et al.*, 2014a]. Note that this rate is a depth-normalized deposition velocity, $\Lambda = v_{dep}/d$, where v_{dep} is the deposition velocity typically reported in field studies [*Thomas et al.*, 2001; *Newbold et al.*, 2005]. Following mobile-immobile stochastic theory [*Schumer et al.*, 2003], we assume $N_{res}(t)$ depends on the number of particles in the immobile zone at time t, as well as on the time each particle has remained immobile since it deposited, $t - \tau$, where τ is the time of immobilization.

These residence times are described by a probability distribution, $\varphi(t)$, which quantifies the probability a particle that has entered the immobile domain at time zero will return to the mobile domain at time t. Substitution of these expressions into equation 4.1 yields an integro-differential equation:

$$\frac{dC(t)}{dt} = \frac{\Lambda dA_b}{V_f}\left(-C(t) + \int_0^t C(\tau)\varphi(t-\tau)d\tau\right)$$

4.2

where Λ is the rate of particle immobilization (defined previously), and A_b is the area of the streambed. An algebraic solution for this expression can be derived after it is transformed to the Laplace domain ($\tilde{f}(u) = \int_0^\infty e^{-ut}f(t)dt$):

$$\tilde{C}(u) = \frac{C_0}{u + \frac{\Lambda dA_b}{V_f}(1 - \tilde{\varphi}(u))}$$

4.3

where $\tilde{C}(u)$ is the Laplace-transformed concentration, C_0 is the initial particle concentration in the water column, u is the Laplace variable, and $\tilde{\varphi}(u)$ is the Laplace transformed resuspension time probability distribution. We assume $\varphi(t)$ takes the form of a power-law distribution ($\varphi(t)\sim t^{-(1+\beta)}, 0 < \beta < 1$), where β is the power-law slope [*Berkowitz et al.*, 2006]. Here, decreasing values of β decrease the power-law slope, which increases the probability that a particle will be retained for very long times. The Laplace-transformed expression for $\varphi(t)$ was inserted into equation 4.3 to give the analytical solution for $\tilde{C}(u)$. This expression was inverse transformed to the time domain using a modified version of the CTRW MATLAB Toolbox (see Supporting Information [*de Hoog et al.*, 1982; *Cortis and Berkowitz*, 2005; *Aubeneau et al.*,

2015b]), yielding a concentration time series for a fixed value of Λ and β. Note that this time series represents the Green's function solution, which represents the system response to a pulse of well-mixed particles entering the mobile domain at $t = 0$. This solution can be convolved with a known source function (e.g., a constant or time-variable influx of particles) to predict a system response to more complex initial conditions.

This form of the mobile-immobile model requires a spatially uniform concentration in the water column, meaning particles are well mixed in all directions. For this reason we only fit the model to concentrations measured after the injected pulse of particles was fully mixed with the flume water. We assume particles are fully mixed after the concentration peak is no longer detectable in the sample time series. The initial particle concentration, C_0, was determined by extrapolating the smoothed time series to time $t = 0$. Particle concentrations can be treated as uniform in the vertical direction for very low values of the Rouse number ($p = {v_g}/{\kappa u_*}$, where p is the dimensionless Rouse number; v_g is the particle settling velocity; κ is Von Karman's coefficient, 0.4; and u_* is the shear velocity) [*Anderson and Anderson*, 2010]. To compare model outputs to experimental results, we normalize particle concentration by C_0 and normalize time by recirculation time, t_r.

We used the Maximum Likelihood Estimation method [*Montgomery and Runger*, 2010] to find values of Λ and β that best fit the concentration time series for each experiment. Details of the fitting procedure are presented in the Supporting Information. All mobile-immobile modeling and MLE fitting steps were executed in Matlab (R2015b).

4.2.6 Correlations between model parameters and biofilm structure

We used linear regression to quantify correlations between biofilm structural parameters and model fits for Λ and β across all experiments. Higher-order models were explored but did not substantially improve fits (results not shown). Model selection and validation was achieved by minimizing the Akaike Information Criterion (AIC) for each model [*Akaike*, 1974]. Statistical analysis was carried out in R [*R Development Core Team*, 2009] .

4.3 Results

4.3.1 Flume hydrodynamics

Average flow conditions are presented in Table 4.1. Flows did not vary considerably in time or between experiments. Stream depth varied by less than 1 mm across the entire flume test section for all experiments. The Rouse number was on the order of 10^{-3} to 10^{-2}, which supports our assumption of spatially uniform particle concentrations in the vertical direction [*Rouse*, 1939].

Table 4.1. Average hydrodynamic conditions across all 14 experiments.

Slope	0.005
d (cm)	0.8 ± 0.1
Q (cm^3/s)	110 ± 13
U (cm/s)	25 ± 4
t_r (s)	25 ± 2
t_0 (s)	75 ± 27
Re	6300 ± 900
Fr	0.87 ± 0.20
Rouse no., p	$(6.8 \pm 1.3) \times 10^{-3}$
u^* (cm/s)	1.7 ± 0.3

4.3.2 Biofilm growth

OCT analysis revealed that biofilm growth started from individual microcolonies (day 18 of experiment) that coalesced through 2-dimensional and 3-dimensional proliferation. An extensive network of void spaces (pores) was visible in biofilms older than 30 days. Isolated streamers developed rather sparsely (1 to 3 per meter of streambed). Streamers were roughly 1 cm in length and extended through the depth of the water column (Figure 4.2e).

Results from all experiments are plotted in Figure 4.2a-c, which show trends in structural parameters for biofilms of different ages. Mean biofilm height, biofilm roughness, and tile coverage increased rapidly between days 30 and 40. The streambed was nearly fully covered (80 to 99%) for biofilms older than 40 d. Mean biofilm height increased to a maximum between 140 and 160 µm, accounting for $\leq 2.5\%$ of water column depth. Biofilm roughness reached a maximum of 86 µm by day 42.
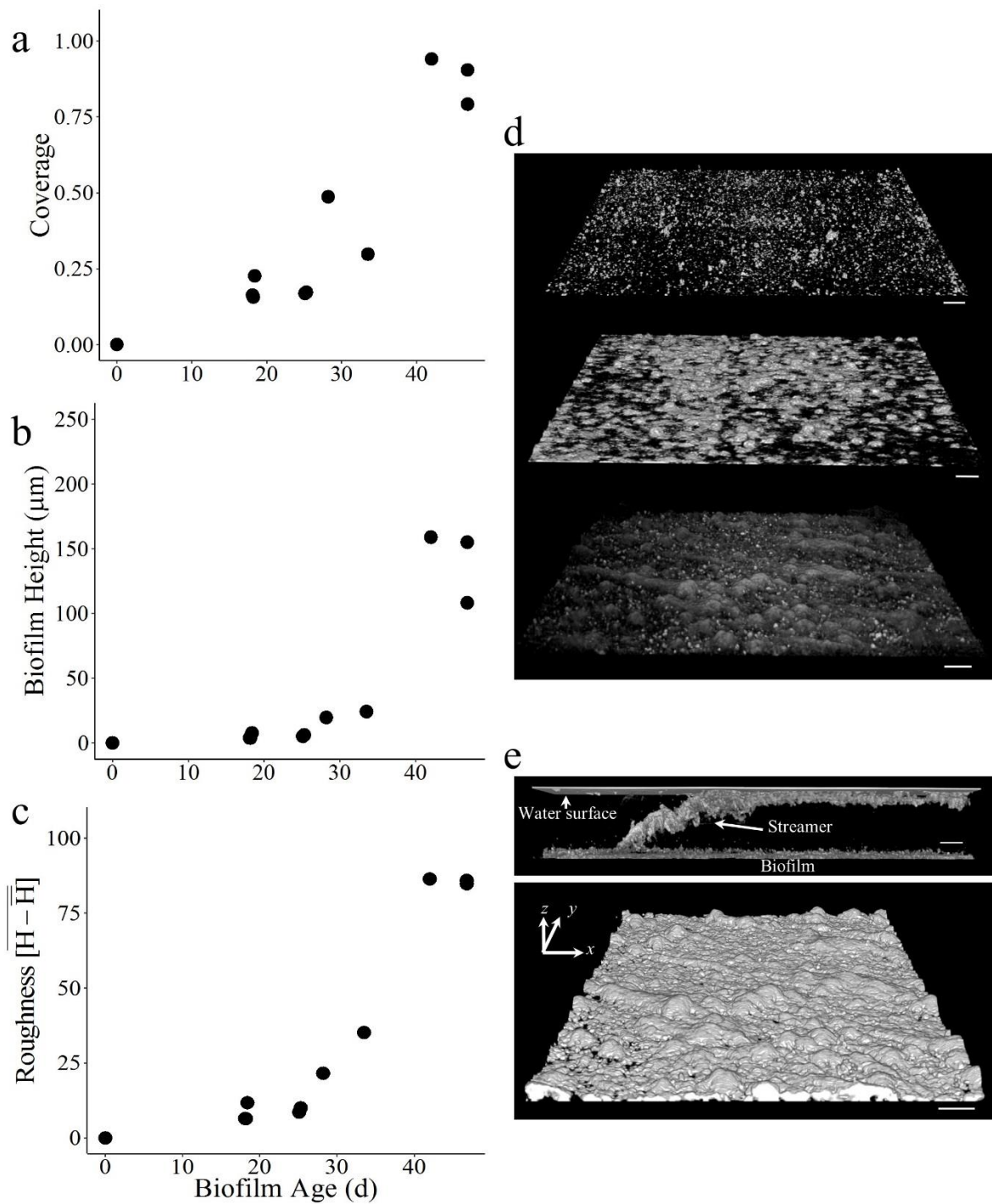
Figure 4.2. (a-c) Biofilm structural parameters measured from each experiment. (d) Processed OCT images for biofilms of different age. Biofilm age (top-bottom) is 18 d, 28 d, and 42 d, respectively. Scale bars are 500 µm for all images. Initial biofilm microcolonies eventually

coalesced into a continuous canopy, resulting in near 100% coverage. (e, top) Processed OCT images illustrating the 3-dimensional structure of a streamer; the thin plane at the top of the image is a surface reflection from water in the sample container. (e, bottom) Surface topography of a 42-d biofilm. Basal dimensions for the image are 9 mm (along page) x 6.3 mm (into page). Mean biofilm height is 115 µm, and max height is 450 µm.

4.3.3 Particle dynamics and model fits

The pulse of particles mixed fully with the water column after 2-5 flume recirculations (0.8-2.3 min) in each experiment, indicated by the disappearance of the recirculating concentration peak (Figure 4.3). Water column concentrations then declined steadily throughout the remainder of the 30-min monitoring period for each experiment. Particle deposition was visible on the face of tiles. In experiments with no biofilm growth, we observed some trapping of particles under and between tiles. We found no particle accumulation below tiles in all other experiments, as the biofilms quickly covered the surface and clogged interstices between tiles.

Water column particle concentrations from each experiment were fit to the mobile-immobile model, as described in the Materials and Methods. Example model fits are presented in Figure 4.4 for illustration. Best-fit parameter values for all experiments are provided in Table 4.2.
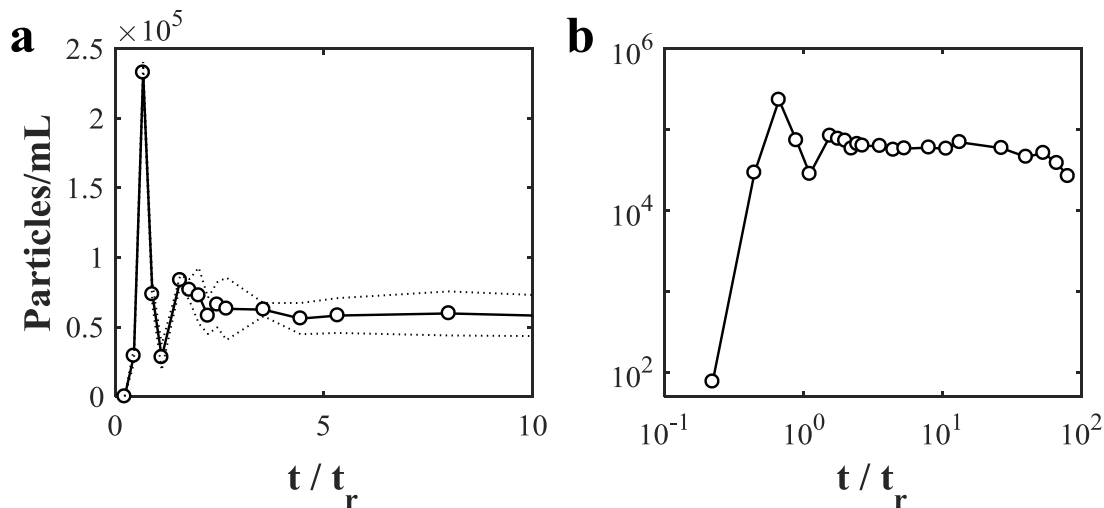
Figure 4.3. Particle concentrations following a pulse release for the experiment with 28-day biofilm. Biofilm is shown in the middle image of Figure 4.2d. Dotted lines show sample standard deviation for the measured particle concentrations. (a) Concentrations shortly after the pulse release (linear scale). (b) Concentrations over the entire deposition period (log scale).
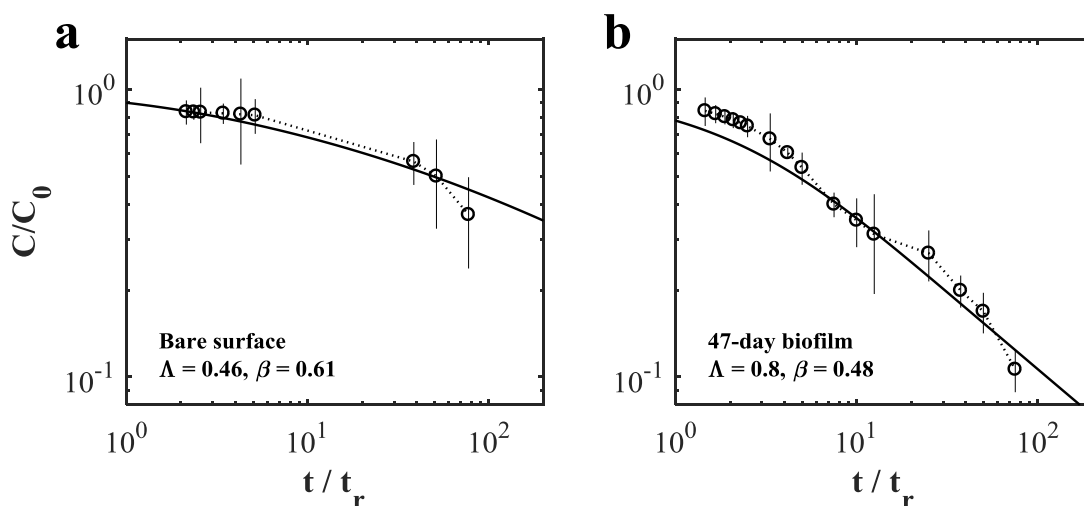
Figure 4.4. (a) Model fits of long-term particle concentrations for a streambed with no biofilm and (b) for a streambed with a 47-day biofilm. C_0 equals the initial particle concentration. t_r is the flume recirculation time. Data and error bars show the mean and standard deviation of triplicate concentration measurements, respectively.

Table 4.2. Measured parameters and mobile-immobile model fits.

Exp. No.	Days Growth	Coverage	Mean Height $\overline{H}$ (μm)	Roughness $\overline{H - \overline{H}}$ (μm)	d (cm)	Q (cm³/s)	U (cm/s)	Re	Fr	p (x 10⁻³)	Λ	β
1	0.0	0.00	0.01	0.0	0.70	116	33	7300	1.26	5.7	0.46	0.61
2	0.0	0.00	0.01	0.0	0.85	116	27	6900	0.95	6.2	0.26	0.72
3	18.1	0.16	3.88	6.5	0.80	109	27	6600	0.97	6.2	0.41	0.65
4	18.2	0.16	3.83	6.5	0.85	115	27	6800	0.93	6.3	0.46	0.44
5	18.4	0.23	7.61	11.8	0.80	112	28	6800	1.00	6.0	0.52	0.57
6	25.1	0.17	5.18	8.6	0.80	99	25	6000	0.88	6.7	0.88	0.60
7	25.3	0.17	6.07	10.0	0.85	101	24	6100	0.83	7.0	0.61	0.59
8	28.2	0.49	19.63	21.6	0.85	111	26	6600	0.90	6.4	0.16	0.49
9	33.5	0.30	24.17	35.2	0.95	75	16	4400	0.52	10.0	0.21	0.43
10	42.0	0.94	158.98	86.4	0.95	118	25	6800	0.81	6.4	0.23	0.42
11	46.8	0.79	108.29	85.9	0.10	88	18	5000	0.56	8.9	0.80	0.48
12	46.8	0.90	155.11	84.8	0.95	117	25	6800	0.81	6.4	0.49	0.46

4.3.4 Correlation of biofilm structure and mobile-immobile model parameters

We found a negative correlation of biofilm age with the power-law slope of the resuspension

RTD, β, demonstrating a significant increase in particle retention times for older communities

($R^2 = 0.58$, $p < 0.01$). Biofilm age did not influence deposition rate, Λ, ($R^2 = 0.02$, $p = 0.62$).

Measured flow parameters did not correlate with Λ ($R^2 < 0.05$, $p > 0.50$ for all parameters

specified in Table 4.1).

Table 4.3. Linear regression results between model parameters and biofilm structural
parameters. A positive (+) effect indicates that increasing values of the structural parameter
increased particle retention/deposition.

Model Parameter	Structural Parameter	Effect	R2	p-value	d.f.	AIC
β	Coverage	+	0.49	0.01	10	-24.74
	Mean Height, $\overline{H}$	+	0.36	0.04	10	-22.05
	Roughness, $\overline{H - \overline{H}}$	+	0.45	0.02	10	-23.87
Λ	Coverage	N/A	0.00	0.92	10	--
	Mean Height, $\overline{H}$	N/A	0.00	0.96	10	--
	Roughness, $\overline{H - \overline{H}}$	N/A	0.00	0.92	10	--

Linear regression results are provided in Table 4.3 for each biofilm structural parameter. All parameters were positively correlated with decreasing values of β, meaning they increased particle retention times. We chose surface coverage as the most robust predictor of β for several reasons: (1) it provided the best goodness of fit and lowest AIC value, (2) coverage values spanned the entire range of possible values, and (3) data points were the least clustered for this parameter. The regression equation was (Figure 4.5):

$$\beta = 0.61 - 0.20 * Coverage$$
$$(R^2 = 0.49, p = 0.011)$$

4.4

Biofilm structure did not influence particle deposition rate in the flumes ($R^2 = 0.00$, p $\geq$ 0.92). Values for Λ ranged between 0.16-0.88 s^{-1}. These rates equate to deposition velocities of 1.9 – 8.0 mm/s, which are 40x – 180x greater than the gravitational settling velocity (0.044 mm/s). Therefore, particle deposition was unaffected by settling. Although preferential deposition was observed behind isolated streamers, these structures only sparsely populated the flumes. Thus, they likely played a minor role in overall deposition.
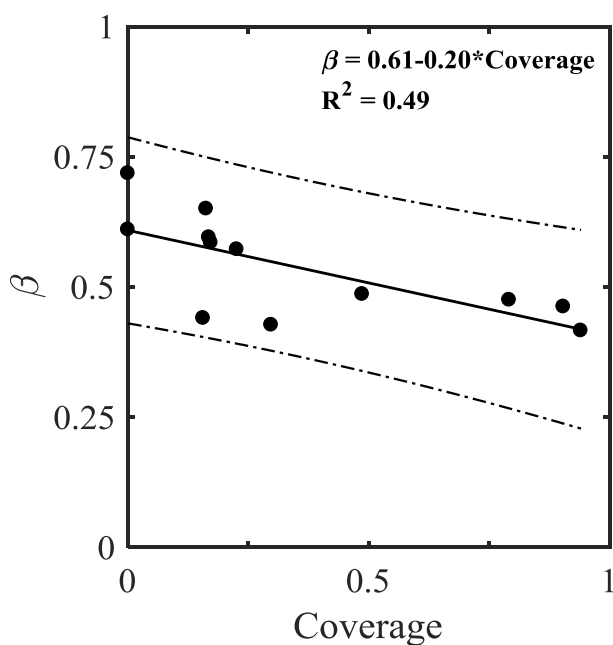
Figure 4.5. Linear regression fit showing relationship between power-law slope, β, and biofilm coverage. Solid line represents the best fit line (equation provided in plot), and dashed lines are 95% confidence intervals.

We present cumulative residence time distributions to illustrate the relationship between β and particle retention (Figure 4.6). The plotted distributions are derived directly from model fits to β for each experiment (see Supporting Information), and they show the probability that a

deposited particle will resuspend after a specified time, for a given value of β. We assume that

resuspension probabilities are nonzero over a finite interval of times, with a minimum of $1/\Lambda_{max}$

≈ 1 s, where Λ_{max} is the upper limit of the calculated values for Λ (0.88 s^{-1}). The maximum

residence time is assumed to be 7 months, which corresponds to retention times observed for

virus-sized particles in wetland mesocosms [*Flood and Ashbolt*, 2000]. The chosen values of β

correspond to measured values at distinct periods of biofilm growth: a bare surface (0%

coverage, $\beta = 0.72$), an 18-day biofilm (23% coverage, $\beta = 0.57$) and a 47-day biofilm (90%

coverage, $\beta = 0.46$). For low resuspension probabilities (< 0.8), an increase in biofilm coverage

results in a marginal increase in retention time (Figure 4.6a). This time difference grows

substantially for resuspension probabilities approaching 1, which reflects the increased

likelihood of very long retention times. For example, a particle will resuspend with 99.9%

probability in 0.17 d for a bare surface vs. 17 d for a bed with 90% coverage (Figure 4.6b).
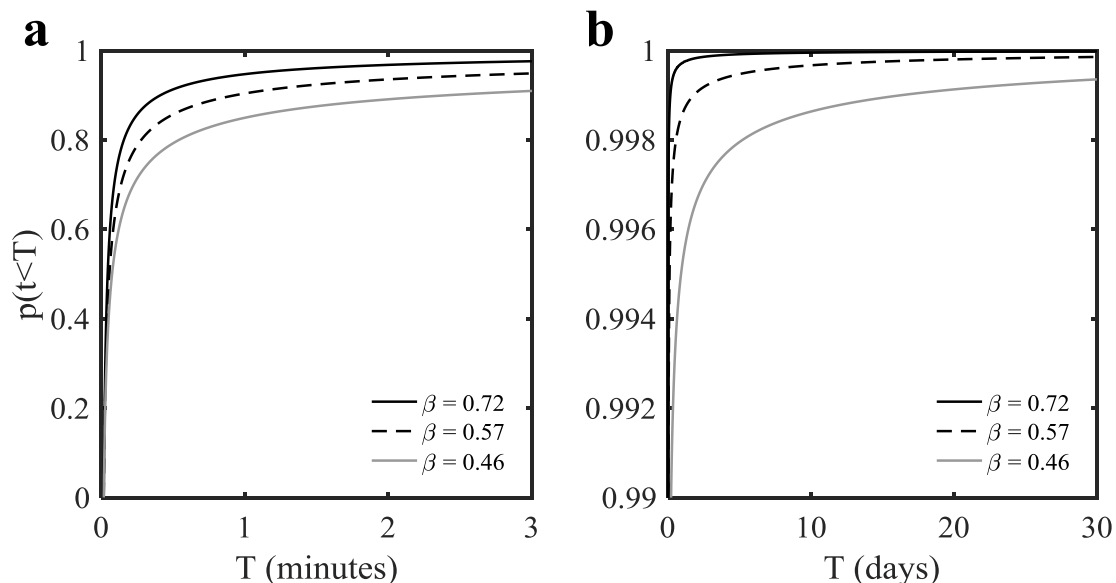
Figure 4.6. Cumulative resuspension time distributions for three measured values of power-law slope, β. A decrease in β increases the time required for a particle to reach a specific probability of resuspension. Distributions are similar at early times but differ substantially as resuspension probability approaches 1. (a) Distributions from 0 to 3 min. (b) Distributions from 0 to 30 d.

4.4 Discussion

Reach-scale particle transport integrates multiple deposition and resuspension events. The relative frequencies of these events determine the balance of fine particle sequestration and export downstream. Thus, the different mechanisms that govern deposition and resuspension must be independently parameterized in fluvial transport models. Using a stochastic mobile-immobile model, we found that fine particle residence times on a biofilm-covered impermeable streambed followed a heavy-tailed power law distribution (Figure 4.4). A similar result was found by *Drummond et al.* [2014a] for fine particles transported in natural streams, in which the authors attributed long-term particle retention to a combination of surface-subsurface (hyporheic)

exchange, reversible filtration by sediments, and trapping by biofilms. Our results show that biofilm trapping alone results in a heavy-tailed power law residence time distribution (RTD).

The power-law slope, β, correlated with mean biofilm height, roughness, and the fraction of the bed covered by biofilm (Table 4.3). Both physical trapping in biofilm pore spaces and electrostatic biofilm-particle interactions have been hypothesized to control particle interactions with the biofilm matrix. Early laboratory studies showed strong correlations between fine particle retention and biofilm thickness, suggesting that trapping within void spaces was most important [*Drury et al.*, 1993a; *Okabe et al.*, 1997]. However, particle trapping has also been observed in nascent (2-µm thick) biofilms that were too thin to contain pores large enough for particles [*Drury et al.*, 1993b]. This finding and others have pointed to particle adhesion to biofilms as an alternative control on particle retention [*Xu et al.*, 2005; *Morales et al.*, 2007]. Biofilm extracellular polymeric substances are typically heterogeneous at the micrometer scale, allowing for varied steric and electrostatic interactions between the biofilm and particle surfaces that favor adhesion [*Bouwer*, 1987; *Sutherland*, 2001; *Searcy et al.*, 2006; *Flemming and Wingender*, 2010].

The structural parameters reported in this study cannot be used to distinguish between physical trapping and particle adhesion to the biofilm, since we could not fully resolve pore structure across the thickness of mature biofilms or distinguish particles within the biofilm matrix. Nonetheless, we highlight the potential for biofilm surface coverage to be used as an integrated predictor of fine particle retention in streams and rivers, since it may be possible to

estimate this parameter without the aid of sophisticated microscopic techniques (e.g., hand-held photography, surface inspection). Biofilm coverage may, therefore, be a suitable complement to other local observations that are used to parameterize solute and fine particle RTDs in upscaled, predictive stream models [*Boano et al.*, 2007; *Stonedahl et al.*, 2012; *Drummond et al.*, 2014a; *Aubeneau et al.*, 2015b]. For example, *Drummond et al.* [2014] performed sediment column filtration experiments on 6-cm bed sediment cores to determine fine particle RTDs in hyporheic sediments of a lowland stream. They then used these results to parameterize a mobile-immobile model that accurately described particle transport and retention in a 221 m stream reach. This approached worked well because hyporheic filtration was the dominant control on particle deposition in the study reach. Biofilms are expected to increase fine particle retention both in the hyporheic zone and on the bed surface [*Thomas et al.*, 2001; *Morales et al.*, 2007; *Arnon et al.*, 2010]. The results presented here provide a basis to include the effects of biofilm coverage and growth directly onto biofilm-covered portions of the streambed, as well as the effects of biofilm coatings of hyporheic sediments, on particle transport. Biofilm growth should then be considered as a secondary modification to the primary retention RTDs [*Margolin et al.*, 2003], parameterized via experiments with biofilms grown on the relevant substratum or with *in situ* observations of particle retention in biofilms.
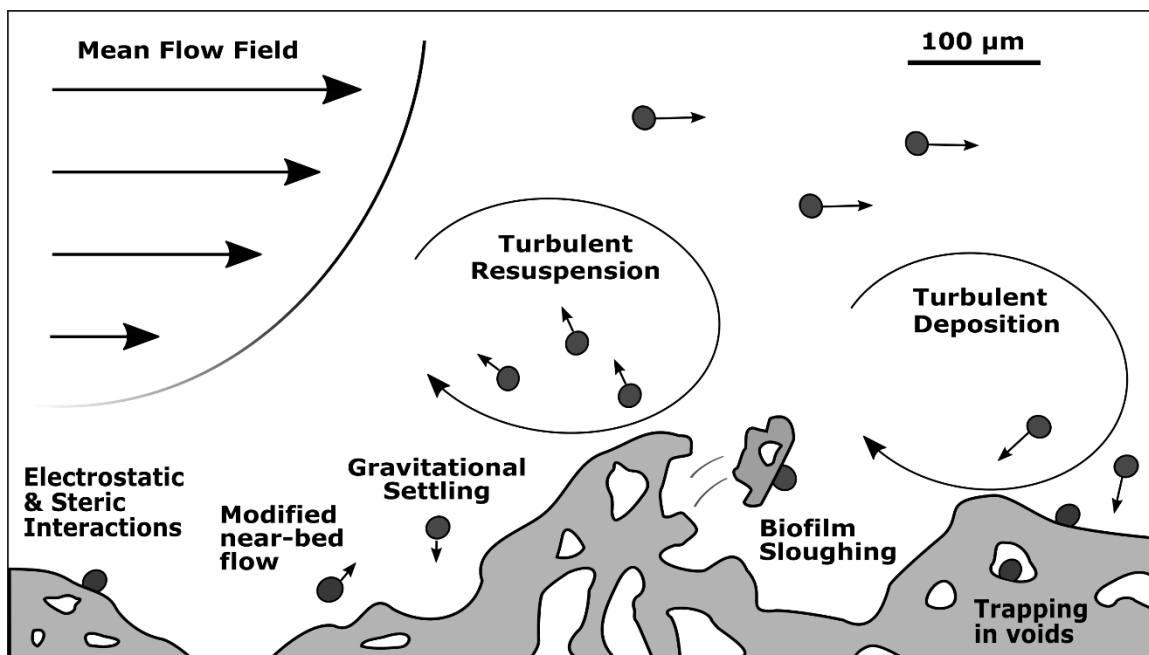
Figure 4.7. Conceptual diagram of mechanisms governing fine particle dynamics for a biofilm-covered streambed. Particle-biofilm interactions occur from scales ranging from biofilm pores (1 µm) to the depth of the stream (1 m).

We found no significant correlation between biofilm structure and particle deposition rate, Λ, which was unexpected. Model fits for Λ were sensitive to concentrations at early times, which were highly variable. Estimates for Λ were, therefore, less robust than estimates for β, which were determined by concentrations at late times. Early-time removal depends on primary delivery and deposition of particles to the benthic biofilm. The influence of biofilm canopies on particle deposition merits further investigation, as biofilm structure is known to influence near-bed hydrodynamics (Figure 4.7). The flow field near the streambed is highly altered by biofilm patches, producing complex, three-dimensional flow patterns [*Costerton et al.*, 1995]. Particles are advected around and into the biofilm before colliding with the biofilm matrix [*Birjiniuk et al.*, 2014]. Positive correlations have been found between particle deposition and biofilm

thickness [*Drury et al.*, 1993b], roughness [*Searcy et al.*, 2006; *DiCesare et al.*, 2012], and sinuosity [*Battin et al.*, 2003a]. However, a definitive mechanistic understanding of structure-deposition interactions requires substantial technological improvements to simultaneously resolve biofilm pore structure, the three-dimensional flow structure around biofilms, and fine particle deposition and resuspension under turbulent conditions [*Weiss et al.*, 2013].

The correlation between biofilm coverage and β, quantified by Equation 4.4, provides a functional relationship between the structure of streambed biofilms and RTDs for fine particles immobilized at the streambed. This relationship highlights one of the numerous process interactions between biofilm-covered streambeds and fine particles. Additional feedbacks recognized in engineered and natural systems are particle size relative to biofilm pore size [*Okabe et al.*, 1998; *Arnon et al.*, 2010], water chemistry [*Searcy et al.*, 2006; *Morales et al.*, 2007], biofilm modification of subsurface flowpaths [*Battin and Sengschmitt*, 1999; *Cuthbert et al.*, 2010; *Aubeneau et al.*, 2016], flow regime [*Okabe et al.*, 1997; *Okabe et al.*, 1998], and complex biofilm responses from interspecies interactions and environmental cues [*Battin et al.*, 2016; *Flemming et al.*, 2016]. Future research efforts should address the relative roles of these process interactions in controlling fine particle dynamics.

The small-scale feedbacks between biofilms and fine particles are a subset of the full range of feedbacks governing particle transport in streams. For example, the deposition dynamics modeled in the current study assume well-mixed particle concentrations in the water column, a condition that can vary over the meter scale in reaches with multiple geomorphological units

(e.g., pool-riffle sequences). Particle fluxes are also coupled to terrestrial factors such as hillslope, vegetation type, and land use [*Gomi et al.*, 2002; *Tank et al.*, 2010], which can create kilometer-scale correlations with stream inputs. Fluxes are driven by high flow events, whose timing and intensity not only influence FPOM supply and retention [*Fisher and Likens*, 1973; *Newbold et al.*, 1997; *Harvey et al.*, 2012; *Karwan and Saiers*, 2012], but also control microbial community lifecycles by scouring and reconfiguring the streambed [*Power and Stewart*, 1987; *Biggs*, 1995; *Gomi et al.*, 2002]. However, as biofilms modify near-bed flows [*Nikora et al.*, 2002; *Larned et al.*, 2011] and stabilize sediments over their growth cycle, they create time-dependent feedbacks that can extend to these scales [*Vignaga et al.*, 2013].

Multiscale feedbacks present a challenge for the application of transport models to streams. Uniform, steady-state models can accommodate spatial and temporal variability if a sufficient separation of scales exists [*Nikora*, 2010; *Marion et al.*, 2014]. Such models average over small-scale heterogeneities and are applied at scales much smaller than large geomorphic features or hydrologic events. Their validity thus depends on the intensity of feedbacks occurring across these scales. Our results contribute to a growing literature that suggests biofilm growth alters fine particle retention across a wide range of timescales [*Flood and Ashbolt*, 2000; *Thomas et al.*, 2001; *Drummond et al.*, 2014b]. These scales overlap with the timescales of hydrologic variability, which compromises the implicit assumption of stationarity in steady state transport models.

Scale interdependencies in fluvial ecosystems remain extremely difficult to characterize. Most experimental and field observations are restricted to a narrow range of spatial and temporal scales, which constrains our understanding of the predominant interactions beyond them. Future research efforts can address these limitations in three ways. First, the small-scale process interactions that control particle transport at the sediment-water interface must be properly characterized. New technologies will greatly improve our ability to directly observe these processes [*Weiss et al.*, 2013]. Such direct observations are needed to independently estimate particle deposition and resuspension rates, which currently are inferred from water column observations. Second, future experimental and field studies must target process interactions over yet-unexplored scale ranges. For instance, our μm-to-cm scale observations of a biofilm-retention feedback must be tested at larger scales where biofilm spatial patterns are observed (1 to 100 m), since small-scale biophysical interactions can control spatial organization at larger scales [*Nikora et al.*, 1998; *Coco et al.*, 2006; *Murray et al.*, 2008; *Larsen and Harvey*, 2010; *Meire et al.*, 2014]. Long-term studies will also provide clues for how particle fluxes and interactions vary across seasonal cycles and episodic events that, for example, could result in nonstationarity of the power-law RTDs identified in our study. Lastly, new process models (e.g., stochastic transport) must be developed to accommodate the hierarchy of scales and processes that influence fluvial ecosystem function [*Nikora*, 2010; *Boano et al.*, 2014; *Marion et al.*, 2014]. Such a framework is required to properly relate laboratory observations (e.g., mm-scale flow-biofilm interactions) to those for the entire fluvial network (e.g., time history of high flow events). These models will provide a tool to explore scale interdependencies that currently

cannot be observed, either experimentally or in the field, and predict how longer-term shifts in land use and climate may alter overall fine particle fluxes in streams [*Battin et al.*, 2009; *Quinton et al.*, 2010; *Tank et al.*, 2010; *Pizzuto et al.*, 2014].

4.5 Conclusions

These experiments show that particles are retained in benthic biofilms across a wide range of timescales (seconds to months). Application of a stochastic mobile-immobile model indicates that fine particle retention probabilities in biofilm-covered streambeds follow a heavy-tailed power law distribution ($\varphi(t) \sim t^{-(1+\beta)}, 0 < \beta < 1$). Particle retention, parameterized by β, was enhanced by increases in mean biofilm height, biofilm roughness, and streambed coverage. These correlations suggest that retention is controlled by biofilm structure, and that biofilm structural parameters should be incorporated into upscaled models for fine particle retention in streams and rivers. However, no biofilm structural parameters were correlated with fine particle deposition rate. Definitive conclusions of deposition-structure interactions require improved experimental capability that can resolve discrete particle deposition and resuspension events at the scales of turbulence. Our results direct future experimental efforts to finer scales (1 to 100 µm) to elucidate the relative importance of microscale physical structure, surface chemistry, and biofilm matrix composition to overall particle deposition and retention. They also call for a multiscale approach to modeling fluvial transport of fine particles, since the process interactions influencing particle retention may be active at different spatial and temporal scales from those influencing deposition.

4.6 Supporting Information

4.6.1 Flume Images

Figure 4.8. Downstream view of flume. Flume and tile width are 5 cm. Tubes connect effluent and influent reservoirs. One tube delivered effluent water to influent reservoir, and the second tube served as overflow.
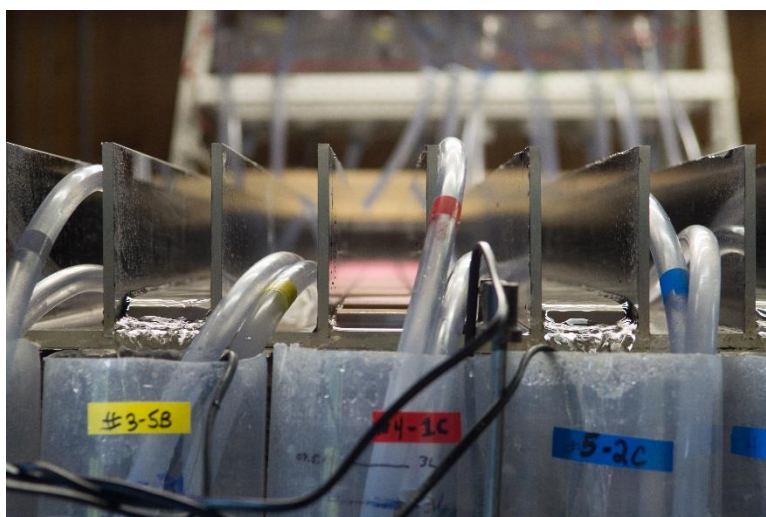
Figure 4.9. Upstream view of flumes from effluent reservoirs. Middle flume (red label) is at the experimental endpoint, with tiles removed for image analysis.

4.6.2 Image analysis workflow

OCT images were obtained using a ThorLabs Ganymede spectral domain (ThorLabs, Newton, NJ, USA) microscope and manufacturer-provided image acquisition software. Output files were 3-D image stacks in TIFF format with 10 μm square voxels and a 1 cm x 1 cm scan area. These files were post-processed using Fiji (ImageJ platform 1.47h). The following steps describe the sequential method by which images were post-processed:

1. An image stack was imported and converted to 8-bit.
2. The original images were distorted so the flat tile surface was concave up. To remove warping, images were flatted via a combination of rotation and registration steps. For example, if the substratum location varied across slices (i.e. 2-D images in the x-z plane), all images in the stack were co-registered so that the substratum was a fixed datum. This step flattened the substratum along the y-axis. A subsequent rotation and co-registration along the x-axis were then performed.
3. Images were cropped to remove the substratum. Areas with significant light attenuation were also removed to minimize intra-image variability.
4. Image noise was reduced in three steps:
   a. We applied the built-in Despeckle feature.
   b. We applied a Gaussian filter. Filter strength ranged from 5-15 μm.
   c. We subtracted a uniform value equal to the median background intensity (intensity 0-25 on a scale of 0-255)
5. The image was thresholded using Otsu's method. The low-intensity cutoff value was adjusted between 9-65 (standard deviation of 8), depending on image quality.
6. For images of biofilms older than 40 d, noise was manually removed from the background area. This step was necessary due to very low signal-to-noise ratios for these images.
7. If necessary, the built-in Fiji processing step 'Remove Outliers' was applied (radius adjusted between 0-2) to further reduce noise from the image.
8. Images stacks were converted to 3D volumes using the '3D Viewer' plugin. 3D volumes were used for illustration only.

Due to a number of limitations, image quality is inversely proportional to biofilm thickness and heterogeneity in OCT analysis. Limited photon penetration depth causes significant signal

attenuation below roughly 100 μm of biomass. High density areas in the biofilm completely reflect incident light, masking all internal structure below them. Also, thicker biofilms (>100 μm) occupy a larger area than the depth of field of the microscope optic. As a result, internal structure was not fully resolved for larger biofilms. OCT images were therefore focused on the uppermost region of the biofilm to fully resolve surface topography. This approach maximized integrity of structural parameters used for this analysis (mean biofilm thickness, variations in thickness, and areal coverage), at the expense of reduced image quality below the biofilm-water interface. Thus, we were unable to fully resolve biofilm porosity.

Variable signal-to-noise ratios across image stacks prevented us from fully automating the post-processing algorithm. Parameters were constrained to the ranges specified above. These variables were chosen to minimize background noise and preserve the bulk biofilm structure. As a result, the total scan area for each replicate varied between 1-10 cm^2.
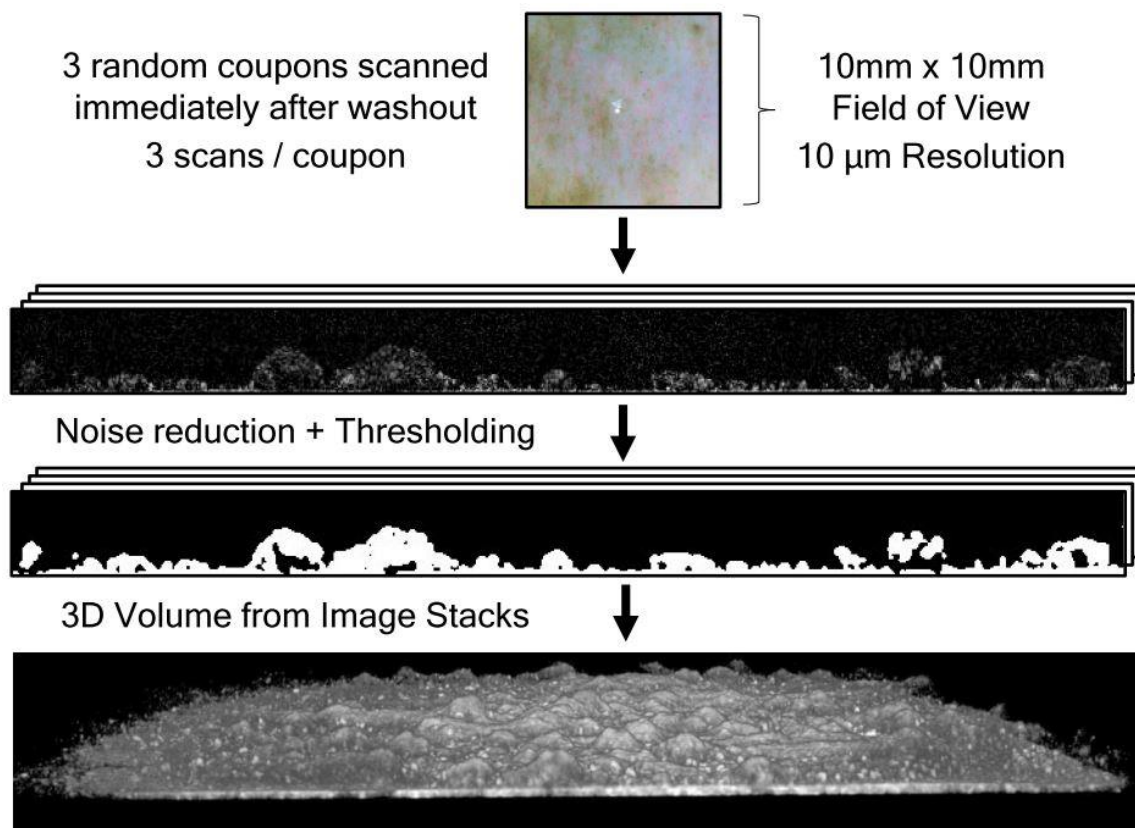
Figure 4.10. Flow diagram describing image analysis procedure.

Figure 4.11. Image slice (longitudinal-vertical plane) of a 47-day biofilm. Large voids are visible throughout the biofilm matrix. Scale bar is 500 μm.

4.6.3 Hydrodynamic calculations

We calculated shear velocity by first estimating the friction factor, f [unitless], from the

Colebrook-White equation for free surface flow:

$$\frac{1}{\sqrt{f}} = -2 \log_{10} \left(\frac{k}{12R_h} + \frac{2.51}{Re\sqrt{f}} \right) \tag{S1}$$

where k is bed roughness estimated from mean biofilm height, and R_h [m] is the hydraulic

radius (ratio of stream cross-sectional area to wetted perimeter). We used f to calculate the shear

Reynolds number u_* [m/s] from the relation:

$$\frac{U}{u_*} = \sqrt{\frac{8}{f}}. \tag{S2}$$

Values for u_* ranged between 1.1 - 2.1 cm/s.

4.6.4 Stochastic mobile-immobile model derivation

We present a derivation of the stochastic mobile-immobile model, adapted for a recirculating

flume. The model is based on Continuous Time Random Walk (CTRW) theory, and it assumes a

partitioning of particles between a well-mixed water column and the streambed. The

concentration, $C(t)$, of particles in a well-mixed water column is described by the following

mass balance:

$$\frac{dC(t)}{dt} V_f = -N_{dep}(t) + N_{res}(t) \tag{S3}$$

where V_f is the volume of water in the recirculating flume, and $N_{dep}(t)$ and $N_{res}(t)$ denote

the rate of particle deposition and resuspension to the streambed, respectively [t⁻¹]. $N_{dep}(t)$ can

be described as a boundary flux of particles, J [particles/(m^2-t)], integrated over the entire bed

surface, A_{bed} [m^2]:

$$N_{dep}(t) = JA_{bed}.$$

(S4)

We assume J takes the form of a first-order removal rate, Λ [s^{-1}], which is proportional to the

concentration per unit bed area:

$$J = \Lambda C(t)d$$

(S5)

where d is the depth of the water column above the streambed [m].

$$N_{dep}(t) = \Lambda C(t)dA_{bed}$$

(S6)

Deposited particles will remain on the bed until the forces keeping it in place (e.g., adhesive,

gravitational) are exceeded by shear forces at the bed surface. These shear forces result from

coherent turbulent structures sweeping over the bed. Assuming steady state flow conditions,

particle resuspension can be described with a probability density function, $\varphi(t)$, defined as the

probability a particle will resuspend at time t after deposition. Particle resuspension over the

interval $t + dt$ therefore depends on the number of particles deposited at time τ:

$$N_{dep}(\tau) = \Lambda C(\tau)dA_{bed}$$

(S7)

as well as the probability of resuspension since the particle was immobilized, $\varphi(t - \tau)$. Total

particle resuspension over the interval $t + dt$ is found by integrating over all possible deposition

times, $\tau \in [0, t]$:

$$N_{res}(t) = \int_0^t N_{dep}(\tau)\,\varphi(t - \tau)d\tau = \int_0^t \Lambda C(\tau)dA_{bed}\varphi(t - \tau)d\tau.$$

(S8)

Substitution of equations (S6) and (S8) into equation (S3) yields:

$$\frac{dC(t)}{dt}V_f = -\Lambda dA_{bed}C(t) + \Lambda dA_{bed}\int_0^t C(\tau)\varphi(t-\tau)d\tau \qquad \text{(S9)}$$

$$\frac{dC(t)}{dt} = \frac{\Lambda dA_b}{V_f}\left(-C(t) + \int_0^t C(\tau)\varphi(t-\tau)d\tau\right) \qquad \text{(S10)}$$

Note that the coefficient dA_b is equivalent to the water volume above the streambed, V_s. Thus, $dA_b/V_f = V_s/V_f$. Equation (S10) represents the desired stochastic mobile-immobile equation, which describes the evolution of particle concentration in the water column. For a given initial concentration, C_0, at $t = 0$, equation (S10) can be solved in Laplace space to derive an analytical solution for the concentration. The Laplace transform of equation (S10) is:

$$u\tilde{C}(u) - C_0 = \frac{\Lambda dA_b}{V_f}\left(-\tilde{C} + \tilde{C}\tilde{\varphi}(u)\right) \qquad \text{(S11)}$$

where $\tilde{C}(u)$ and $\tilde{\varphi}(u)$ denote the Laplace transforms of $C(t)$ and $\varphi(t)$, respectively. The analytical solution for the Laplace transform of $C(t)$ is then given by:

$$\tilde{C}(u) = \frac{C_0}{u + \frac{\Lambda dA_b}{V_f}(1 - \tilde{\varphi}(u))}. \qquad \text{(S12)}$$

We assume a power-law resuspension distribution $\varphi(t) \sim t^{-(1+\beta)}$, $(0 < \beta < 1)$ since fine particles have been shown to follow this distribution in natural streams [*Drummond et al.*, 2014a; *Drummond et al.*, 2014b]. In Laplace space $\tilde{\varphi}(u) = 1/(1+u^\beta)$. This expression was substituted into (S12) to yield the final form of the Laplace-transformed analytical solution. The solution was inverse transformed to the time domain using a modified version of the CTRW toolbox

developed by *Cortis and Berkowitz* [2005] and adapted by *Aubeneau et al.* [2015b]. The toolbox

uses DeHoog's algorithm [*de Hoog et al.*, 1982] to perform the inverse Laplace transform.

4.6.5 Model fits

Prior to model fits, we smoothed each concentration time series using the built-in Matlab

function *smooth* (10% averaging window, 'rlowess' method). Concentration and time was

normalized as reported in the main text.

We used the method of maximum likelihood estimation (MLE) to find best fits for the

smoothed data to the mobile-immobile model [*Montgomery and Runger*, 2010]. Briefly, this

statistical estimation method assumes that values of the measured concentration time series are

normally distributed about an unknown, but true, model time series with fixed values of Λ and β:

$$\mathcal{L} = \prod_{i=1}^{N} f(C_i | C_{m,i}, \sigma) = \prod_{i=1}^{N} \frac{1}{\sqrt{2\pi\sigma^2}} e^{\frac{(C_i - C_{m,i})^2}{2\sigma^2}} \tag{S13}$$

where $\mathcal{L}$ is the likelihood function (to be maximized), C_i is the sample concentration at time t_i,

$C_{m,i}$ is the model concentration, i is the sample index, σ is the standard deviation (assumed to be

$0.2C_{m,i}$), and N is the total number of samples in the time series. The fitting algorithm iteratively

generates outputs of the mobile-immobile model (with different values of Λ and β) to maximize

the likelihood function.

Table 4.4. Mobile-immobile model fits and additional parameters. Λ_{init} and β_{init} were the parameter values determined from manual fits, which were used as starting values for the MLE fits (Λ_{fit} and β_{fit}). V_f and V_s/V_f were determined from solute mass balance, as described in the main text. Note that an effective flume length of 2.85 m was used for the

calculation of V_s/V_f, since the first 0.15 m was not lined with tiles to accommodate the flow inlet.

Exp. No.	$\Lambda_{init}:\Lambda_{fit}$	$\beta_{init}:\beta_{fit}$	V_f (L)	V_s/V_f
1	.500 : .464	.450 : .610	2.5	0.40
2	.200 : .255	.600 : .718	2.3	0.52
3	.300 : .405	.600 : .650	3.0	0.38
4	.600 : .461	.550 : .442	2.4	0.51
5	.500 : .519	.600 : .572	2.5	0.46
6	.700 : .884	.580 : .595	2.3	0.50
7	.550 : .605	.550 : .585	2.2	0.55
8	.100 : .163	.300 : .486	2.2	0.55
9	.150 : .213	.200 : .427	2.5	0.54
10	.300 : .227	.400 : .416	2.8	0.49
11	.650 : .800	.450 : .475	2.5	0.57
12	.400 : .489	.350 : .462	2.9	0.46

4.6.6 Cumulative probability density function calculations

To illustrate the influence of β on retention times, we present cumulative probability density functions (CDF) in the manuscript, which are calculated from fits of β. For convenience, we assume resuspension times are non-zero over a finite interval, with the following PDF:

$$\varphi(t) = \begin{cases} Ct^{-(1+\beta)}, & t_{min} \leq t \leq t_{max} \\ 0, & otherwise \end{cases} \tag{S14}$$

where C is a normalization constant , t_{min} is the minimum resuspension time, t_{max} is the maximum resuspension time, and $0 < \beta < 1$. We set $C = \beta/(t_{min}^{-\beta} - t_{max}^{-\beta})$ so the

distribution integrates to 1. We assume $t_{min} = 1/\Lambda_{max} \approx 1$ s, where Λ_{max} is the upper limit of

the calculated values for Λ (0.88 s⁻¹), and $t_{max} = 7$ months, since retention time of virus-sized

particles in wetland mesocosms has been observed for at least this duration [*Flood and Ashbolt*,

2000]. This PDF can be integrated to yield the corresponding CDF:

$$p(t \leq T) = \int_{t_{min}}^{T} C\varphi(t)dt = \frac{t_{min}^{-\beta} - T^{-\beta}}{t_{min}^{-\beta} - t_{max}^{-\beta}} . \qquad (S15)$$

CDFs for three experimental fits of β are presented in Figure 4.6.

CHAPTER 5

An integrated experimental and modeling approach to predict sediment mixing from benthic burrowing behavior *

Predict Sediment Mixing from Benthic Burrowing Behavior, *Env. Sci. Tech.*, 50 (18), 10047-

10054, doi: 10.1021/acs.est.6b01704.

ABSTRACT

Bioturbation is the dominant mode of sediment transport in many aquatic environments, and strongly influences both sediment biogeochemistry and contaminant fate. Available bioturbation models rely on highly simplified biodiffusion formulations that inadequately capture the behavior of many benthic organisms. We present a novel experimental and modeling approach that uses time-lapse imagery to directly relate burrow formation to resulting sediment mixing. We paired white-light imaging of burrow formation with fluorescence imaging of tracer particle redistribution by the oligochaete *Lumbriculus variegatus*. We used the observed burrow formation statistics and organism density to parameterize a parsimonious model for sediment mixing based on fundamental random walk theory. Worms burrowed over a range of times and depths, resulting in homogenization of sediments near the sediment-water interface, rapid nonlocal transport of tracer particles to deep sediments, and large areas of unperturbed sediments. Our fundamental, parsimonious random walk model captures the central features of this highly heterogeneous sediment bioturbation, including evolution of the sediment-water interface coupled with rapid near-surface mixing, and anomalous late-time mixing resulting from infrequent deep burrowing events. This approach provides a general, transferable framework for explicitly linking sediment transport to governing biophysical processes.

5.1 Introduction

Sediment-dwelling organisms modify their local environment as they burrow, scavenge for food, and hide from predators. Biological reworking of sediments, termed *bioturbation*, mixes

particles in the sediment bed [*Thibodeaux and Bierman*, 2003; *Meysman et al.*, 2006; *Kristensen et al.*, 2011]. Reworked sediments encounter different biogeochemical environments that control particle transformation, for example by microbial metabolism, precipitation/dissolution, and sorption/desorption processes. Particulate organic matter is metabolized more slowly in anoxic sediments, and particles retained in such environments are more likely to be preserved [*Lehmann et al.*, 2002; *Thomsen et al.*, 2004; *Canavan et al.*, 2006]. Similarly, reduced metal sulfides are oxidized when transported from depth into oxic surficial environments, leading to liberation of bioavailable dissolved metals [*Phipps et al.*, 1993; *Sundelin and Eriksson*, 2001; *Ciutat and Boudou*, 2003; *Simpson et al.*, 2012; *Remaili et al.*, 2016]. Bioturbation is thus an important transport process that should be included in biogeochemical models for sediment diagenesis and contaminant fate in sediments.

Continuum models are widely used to represent bioturbation [*Boudreau*, 2000; *Lampert and Reible*, 2009; *Bessinger et al.*, 2012; *Lin et al.*, 2014]. These models treat the subsurface as a continuous domain with volume-averaged bulk properties, such as porosity and particle concentrations. The simplest continuum model for bioturbation is the 1-D biodiffusion model [*Goldberg and Koide*, 1962; *Guinasso and Schink*, 1975; *Berner*, 1980; *Boudreau*, 2000; *Thibodeaux et al.*, 2001]. In this model, fluxes are proportional to local concentration gradients, following classical Fickian diffusion assumptions, yielding particle motions that are small, isotropic and frequent relative to the scale of observation [*Boudreau*, 1986b; *Meysman et al.*, 2010]. Scale restrictions limit the applicability of local continuum models in natural environments. Motion that violates standard assumptions of regular Fickian diffusion, and thus

cannot be predicted by continuum biodiffusion models, is commonly termed anomalous transport [*Metzler and Klafter*, 2000; *Zhang et al.*, 2012]. Fickian assumptions are violated when organisms quickly transport sediments over long distances. In this case, particle fluxes are not controlled solely by local concentration gradients, and are thus nonlocal. Commonly used bioturbation models are also asymptotic, meaning they are valid only after a large number of mixing events have been observed. However, timescales for sediment mixing by bioturbation can be very large because burrowing is highly heterogeneous and new burrow formation is infrequent, yielding substantial deviations from asymptotic model predictions [*Meysman et al.*, 2010].

Several approaches have been proposed for anomalous bioturbation. Robbins[*Robbins*, 1986] and Boudreau [*Boudreau*, 1986a] independently developed models to describe upward-conveying deposit feeders, which are worms that continuously ingest sediments at depth and egest them above the sediment-water interface (SWI). These models include a nonlocal transport term associated with feeding over a range of depths. François et al. [*François et al.*, 1997] extended this approach to 2-D using a finite element numerical model. Stochastic continuous time random walk (CTRW) models have also been proposed for bioturbation [*Maire et al.*, 2007; *Meysman et al.*, 2008a]. As with Fickian biodiffusion, CTRW models describe the ensemble redistribution of particles resulting from an underlying random motion, but no predefined range of scales are assumed in the CTRW formulation. Instead, the model is parameterized with probability density functions (PDFs) whose shapes explicitly define the scales that govern particle movements.

A scarcity of direct observations limits identification and parameterization of bioturbation models [*Meysman et al.*, 2008b; *Meysman et al.*, 2008a]. Current models assume, but do not verify, that biodiffusion and nonlocal transport are the relevant processes governing sediment mixing. Incorrect assumptions of governing processes greatly limit model fidelity and transferability, since model parameters are not clearly linked to fundamental, measurable system attributes. The goal of the present study was to develop a parsimonious model to directly relate statistics of burrow formation to resulting sediment mixing. We used *Lumbriculus variegatus* as a model organism because it is a common bioturbator of freshwater sediments and a standard test organism for contaminant transport and toxicity studies [*Spencer*, 1980; *Timm*, 1980; *Lauritsen et al.*, 1985]. *L. variegatus* is a head-down deposit feeder that transports sediments nonlocally by ingesting particles at depth and egesting them at the SWI. Using time-lapse imagery, we observed the development of burrow structures and the resulting redistribution of tracer particles within experimental chambers. We then used the observed burrow statistics to parameterize a numerical random walk model for sediment bioturbation, and tested the model predictions against independent observations of sediment transport.

5.2 Methods

5.2.1 Sediment Collection and Characterization

We collected sediments from Lake DePue, a shallow backwater lake of the Illinois River (IL, USA). Sediments, collected to a depth of 15 cm, were transported to the laboratory and refrigerated at 4 °C until used. Sediments were characterized by Xie et al. [*M W Xie et al.*, 2015].

81% of the sediments by volume had a diameter ≤ 45 µm, and ~70% had a diameter ≤ 10 µm. Bulk sediment properties (porosity, permeability, carbon content, and metals concentrations) are reported in the Supporting Information.

5.2.2 Experimental Setup

Organism burrowing and sediment mixing were observed in an acrylic aquarium (10 cm long x 10 cm wide x 22 cm high). We added 8 cm of homogenized sediment to the aquarium and then added 1.5 L of artificially-reconstituted fresh water (see Supporting Information) [*Smith et al.*, 1997; *M W Xie et al.*, 2015], creating a 10-cm water column that was constantly recirculated between the aquarium and the reservoir. A mechanical stirrer (IKA Lab Egg, Cole Parmer, IL, USA) was used to keep the overlying water in the aquarium well mixed, and the reservoir was constantly aerated so that the water column remained oxic.

We allowed sediments to stabilize for 24 h, which was sufficient for all suspended particles to deposit back to the bed. We then added 5 mg of fluorescent tracer particles (ZQ-14, DayGlo Color Corp, OH) to form a uniform 0.8-mm-thick layer at the SWI. Tracer particles had excitation and emission wavelengths of 405 nm and 620 nm, respectively. The tracer particle size (20-60 µm in diameter) was chosen so that particle mobility was similar to Lake DePue sediments, based on the critical shear for resuspension.

We added 0.250 g of *Lumbriculus variegatus* (Aquatic Research Organisms, Hampton, NH, USA) evenly over the SWI immediately following sediment stabilization. This corresponds to an organism density of 6,300/m^2 [*Landrum et al.*, 2002], which falls within the typical range of

oligochaete densities in freshwater sediments, 1,000-40,000/m^2 [*Brinkhurst*, 1970; *Cook and Johnson*, 1974; *Sauter and Güde*, 1996]. *L. variegatus* egested and excreted the organic-rich test sediments, and no exogenous food was added during the experiment.

This experimental setup enabled us to directly assess the linkage between *L. variegatus* movement and sediment transport, since all observed transport events were directly associated with organism motions. We used time-lapse photography to capture *L. variegatus* burrowing activity and resulting sediment transport. Methods to measure tracer particle motion follow those previously used to assess biological reworking of freshwater and marine sediments [*Maire et al.*, 2007; *Bernard et al.*, 2012]. We placed a digital camera (Nikon D7000, 40-mm macro lens) 35 cm from one face of the experimental chamber (Figure 5.1), providing a 13-µm pixel resolution. Burrow development and resulting sediment mixing were then imaged with a series of three photographs taken at 3-min intervals. Tracer particles were first imaged using ultraviolet LEDs (excitation wavelength 407 nm, Super Bright LEDs Inc., St. Louis, USA), and the fluorescent emission signal was isolated by a 610-nm bandpass filter (10 nm bandwidth, Edmund Optics Inc., NJ, USA). White LEDs (Super Bright LEDs) were then triggered to capture the SWI location SWI and worm burrows. Lastly, a dark image was taken to measure background light. The experiment was replicated in duplicate using sediments from the same sample and identical image-acquisition hardware.

5.2.3 Image Processing

Image processing, numerical simulations, and model fits were performed with Matlab R2015b (Mathworks Inc., USA). Images were converted from .RAW to .JPEG using a linear tone curve, after which background light intensity was subtracted (dark images). We quantified SWI movement by first identifying images where the SWI changed rapidly (e.g., because of sediment mound collapse). We manually traced the SWI in these images and then automatically interpolated the SWI for all others.
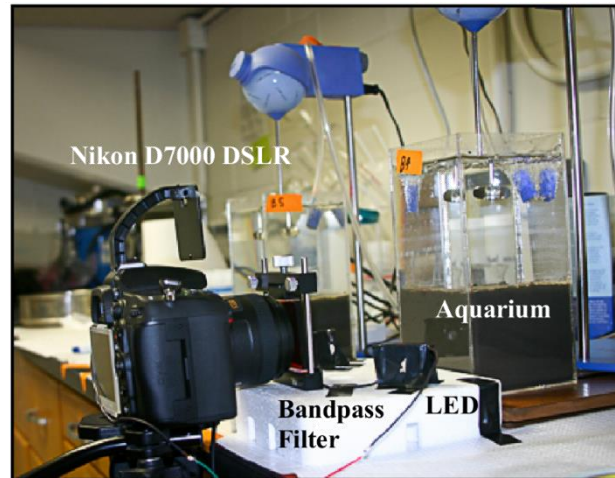
Figure 5.1. Experimental setup.

To calculate tracer particle distributions, we averaged light intensity over the width of each fluorescent image to generate a 1-D fluorescence intensity profile, $F(x,t)$, where x equals distance below the SWI and t is time since worms were added. We then normalized these profiles by the overall light intensity measured below the SWI:

$$P(x,t) = \frac{F(x,t)}{\sum_x F(x,t)}.$$

5.1

Burrows were identified using white-light images. We smoothed these images using a Gaussian filter and binarized them using a global thresholding algorithm (detailed in Supporting Information). Because LED intensity varied slightly from image to image, we averaged images over a 90-min window to exclude optical noise and minimize misidentification of spurious burrowing events. We then coarsened the resulting grayscale images to 230-μm pixels, corresponding to the typical burrow width. The resulting image was 205 x 137 pixels. Burrow development was determined from pixels that changed from light to dark between successive images. Burrows were identified at a threshold of <15% light intensity to minimize false positives. For each pixel that changed from light to dark, the pixel depth and the time since the last disturbance event (wait time) were recorded. We used these results to generate a joint PDF:

$$\Psi(x,\tau) = \frac{n(x,\tau)}{N} \qquad 5.2$$

where $\Psi(x,\tau)$ is the probability density of a burrow event occurring at depth x after wait time τ, $n(x,\tau)$ is the number of events that occurred for a pixel centered at depth x with wait time τ, and N is the total number of events. Marginal burrow-depth and wait-time PDFs were computed from the joint PDF by integrating over the complementary parameter:

$$\lambda(x) = \int_{\tau} \Psi(x,\tau)\, \mathrm{d}\tau \qquad 5.3$$

$$\varphi(\tau) = \int_{x} \Psi(x,\tau)\, \mathrm{d}x. \qquad 5.4$$

5.2.4 Random Walk Model

We constructed a numerical random walk model for sediment motion conditioned on $\Psi(x, \tau)$. The model domain consisted of a 2-D grid, identical to the coarsened grid used to monitor burrowing events. Model time steps were set equal to the averaging window for experimental images (90 min). The initial condition was a thin layer of tracer added uniformly to the top 0.8 mm of the grid, which matched the experimental conditions.

We considered two different random walk models: coupled and uncoupled. In the coupled model, sediment particles sample a wait time, $T \sim \varphi$, and then sample a burrow depth from the joint density, $X \sim \Psi(\cdot, T)$, which is conditioned on T. In the uncoupled model, sediment particles sample independently from φ and λ. Burrowing events are considered vertical and instantaneous, so within a single time step a worm is assumed to have burrowed and returned to the surface. The horizontal location of each burrow is randomly assigned from a uniform distribution. Tracer particles are redistributed according to a set of rules that transports a fraction of sediments to the SWI at a rate proportional to the mean SWI velocity (i.e. rate of SWI movement due to sediment reworking), and a characteristic burrow velocity derived from the marginal PDFs (see Supporting Information).

We ran 200 realizations of the model to generate ensemble-averaged concentration profiles $C(x, t)$. Worm densities matched experimental conditions, $6{,}300/m^2$. We then calculated the mean and variance for the tracer particle concentration profile at each time:

$$E(X,t) = \int_0^{x_{max}} xC(x,t)\mathrm{d}x \qquad\qquad 5.5$$

$$E(X^2,t) = \int_0^{x_{max}} \left(x - E(X,t)\right)^2 C(x,t)\mathrm{d}x. \qquad\qquad 5.6$$

5.2.5 Biodiffusion Model

For comparison, we fit a simple advection-diffusion (ADE) model to experimental results:

$$\frac{\partial C(x,t)}{\partial t} + U_b \frac{\partial C(x,t)}{\partial x} = D_b \frac{\partial^2 C(x,t)}{\partial x^2} \qquad\qquad 5.7$$

where U_b is the bioadvective drift of the tracer peak and D_b is the effective biodiffusion coefficient (both assumed constant). We treated the SWI as a no-flux boundary, enabling a standard Green's function solution to the problem [*Polyanin and Nazaikinskii*, 2016]. We fit U_b and D_b with a Maximum Likelihood Estimation method [*Montgomery and Runger*, 2010].

5.3 RESULTS

5.3.1 Burrow statistics
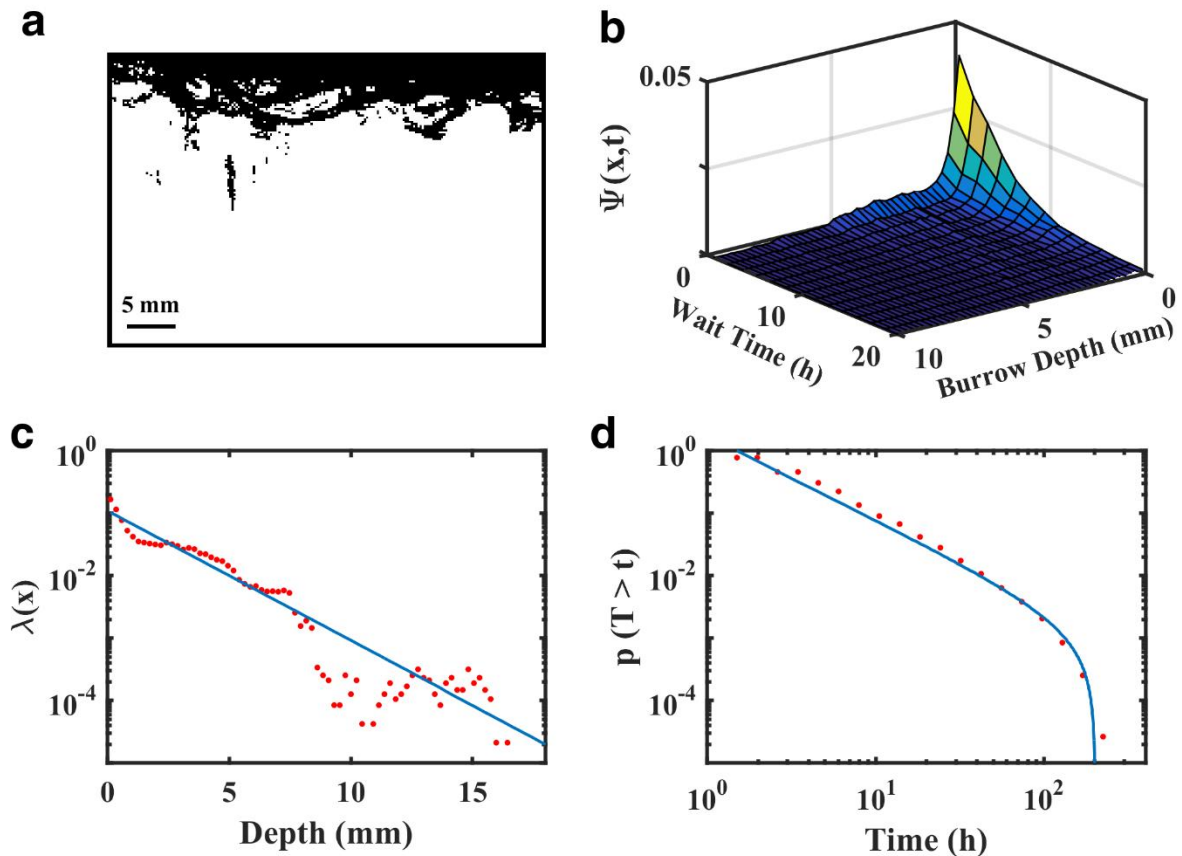
Figure 5.2. (a) Event plot showing locations where at least one burrowing event occurred (black pixels). Large portions of the sediment remained unworked, especially below 10 mm (white pixels). (b) PDF of organism movements. This density was decomposed into marginal burrow-depth and wait-time PDFs. (c) Marginal burrow-depth density with an exponential fit, $\lambda(x) \sim \gamma e^{-\gamma x}$, where $\gamma = 0.48$/mm. (d) Cumulative wait-time distribution, fit to a truncated power-law distribution, $p(T > \tau) \sim \frac{\tau_1{}^\beta (\tau^{-\beta} - \tau_2{}^{-\beta})}{1 - (\tau_1/\tau_2)^\beta}$, for times $\tau_1 \ll \tau \ll \tau_2$, where β is the power law slope [*Aban et al.*, 2006]. Line shows a best-fit truncated power law with $\tau_1 = 1.5$ h, $\tau_2 = 200$ h, and $\beta = 1.35$.

Total sediment reworking (Figure 5.2a) and burrowing distributions (Figure 5.2b,c) varied

with depth. By day 9, worms had reworked 86% of sediments above 5.0 mm and 10.3% of

sediments between 5.0 mm and the deepest burrow (16.4 mm). Percentages increased to 90%

and 13.5% by the end of the experiment. Just 3% of sediments from 10.0-16.4 mm were

reworked at the experimental endpoint. The joint PDF, Ψ, shows that 56% of burrowing events

were less than 5 mm with wait times less than 10 h (Figure 5.2b). Burrows below 10.0 mm

accounted for 0.4% of all events. An average burrow depth of 2.16 mm and wait time of 0.91 d

were calculated from the marginal densities.
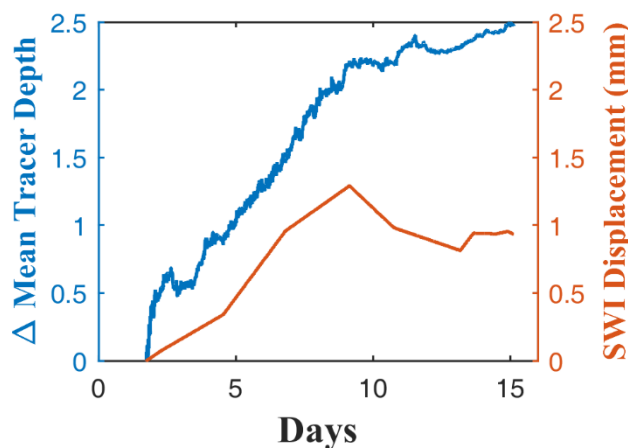
Figure 5.3: Time series of mean tracer depth and SWI displacement. t = 0 is the time at which
worms were introduced.

Because sediments did not completely consolidate until 2 d after worms were introduced, we

tracked the evolution of the average SWI location relative to its location when sediments finished

consolidating (day 2). After consolidation the SWI height grew linearly until stabilizing at day 9

(Figure 5.3, red line). Time-lapse photography showed that this stabilization was primarily due to

excavated sediment mounds collapsing at a rate equal to their growth (see movie S1). However, the rate of sediment reworking also decreased from 4,200 pixels/day to 3,200 pixels/day after day 9 (24% decrease). SWI velocity was found to be 0.18 mm/d for the initial period of linear growth (days 2-9).

5.3.2 Fluorescent Tracer Results
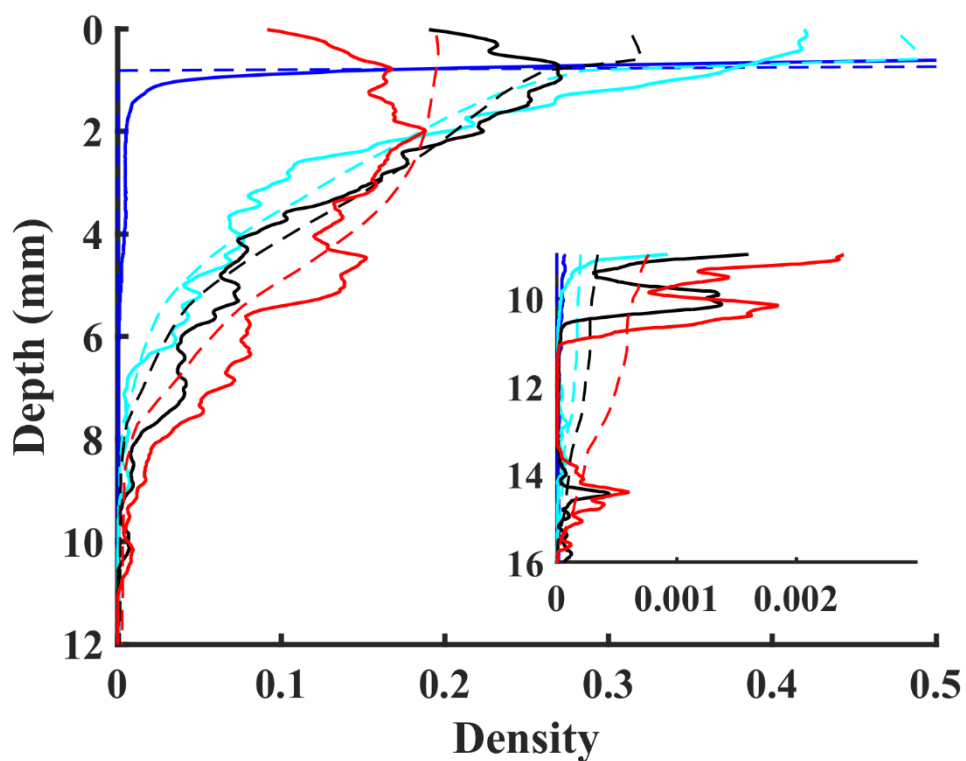
Figure 5.4: Fluorescence profiles from the experiment (—) and the joint random walk model (– –) at different times; blue, cyan, black, and red lines are 0, 4, 7, and 15 d, respectively. Tracer spread rapidly from the SWI and then slowed at later times, as evidenced by the similarity between Day 7 and Day 15 profiles. Inset shows tracer profiles in deep sediments. The model captured rapid tracer propagation into deep sediment layers (below 10 mm), which could not be captured by the ADE model (results shown in Supporting Information).

Tracer particles were rapidly mixed near the SWI (upper 5 mm) and also rapidly driven into deeper into the bed. Depth-averaged tracer concentration profiles are shown in Figure 5.4 for multiple times. Profiles are characterized by a slow advection of the tracer peak, accompanied by a gradual decrease in the peak concentration and spreading of the tracer profile. Both advection and spreading of the peak slowed at day 9, and little change occurred in the profile from days 9-15. Nonlocal tracer transport was observed as early as 1.75 d, when a peak appeared at 8 mm depth. The first peak below 10 mm appeared on Day 6 (14 mm).
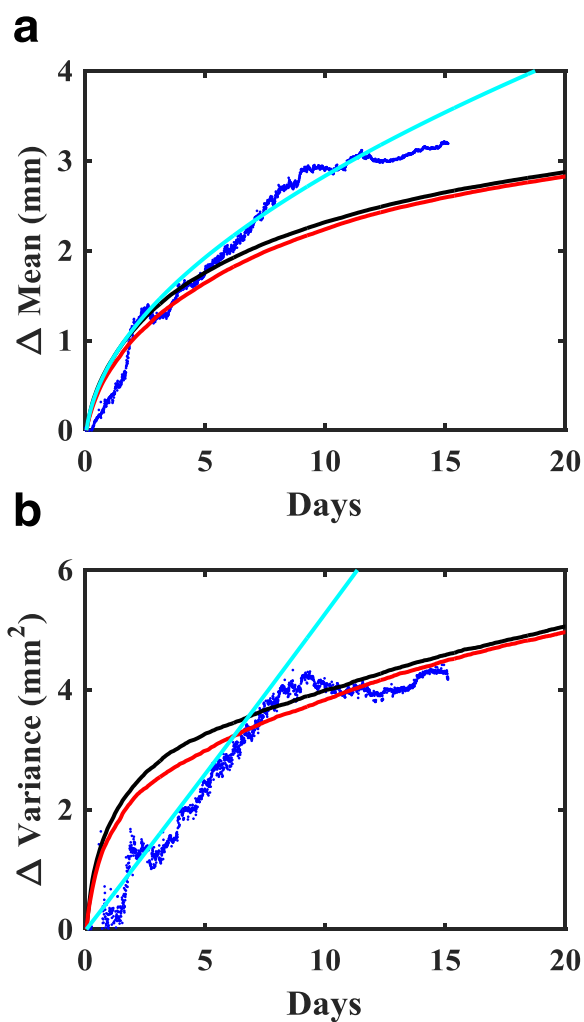
Figure 5.5: Changes in tracer mean (a) and variance (b) from initial values calculated from experimental observations (blue dots) and predicted by the models (black line for coupled, red line for uncoupled, and cyan line for ADE).

The gradual changes in advection and spreading were also reflected in the first- and second-order statistics of the profiles (Figure 5.5, blue dots). Both experimental statistics showed a sharp transition to slower growth rates at day 9, and this timing corresponded exactly to the transition in the SWI displacement (Figure 5.3). Similar trends in tracer mean and variance were observed in a replicate experiment (see Supporting Information).

5.3.3 Model Results

The random walk model reproduced several central features of the experimental tracer profiles, including the slow advection of the tracer peak, spreading of the peak, nonlocal transport beyond 10 mm, and rapid mixing of near-surface sediments (Figure 5.4). The coupled and uncoupled models performed nearly identically, which indicates that burrowing depth and frequency were largely independent. Random walk simulations captured the overall trend in both the mean and variance, but under-predicted the observed mean tracer propagation (Figure 5.5). However, the asymptotic rate of increase of the mean was identical between models and experiment (0.04 mm/d at day 15), indicating that the random walk model captures the asymptotic behavior over long times. Predicted and observed variance matched near the experimental endpoint, but model's rate of increase was 3 times faster than the experimental rate (0.09 mm^2/d vs 0.03 mm^2/d, averaged over 1 d).

Because the sediment redistribution time series exhibited a clear non-diffusive trend, we fit the ADE model over the initial time interval where experimental variance was linear (days 0-9). Best-fit values were $U_b = 0.052$ mm/d and $D_b = 0.73$ mm^2/d. The ADE could not adequately capture deep burrowing events at early times because this model only represents local diffusive fluxes with an inherent length support scale of $\sqrt{2D_b t}$. As a result, the ADE only predicted significant motion below 10 mm after 3.9 d (based on tracer concentration density $> 1 \times 10^{-4}$), whereas the random walk model reached this threshold over just 0.4 d because of its ability to reproduce rapid, nonlocal transport events based on the observed spatial and temporal scales of

worm burrow events. The ADE model greatly overpredicted the mean transport at late times because this model only accounts for mean transport with a time-invariant advection parameter. Mixing events in the random walk model were directly related to burrowing events and, thus, were appropriately restricted to the bioactive region of sediments. This enabled the random walk model to more accurately capture the observed transition to slower mean transport after day 9. Similarly, ADE variance increased linearly, which matched the experimental result at early times (a direct consequence of the model fit) but failed to capture the transition to slower spreading after day 9. This transition was captured by the random walk model owing to its direct encoding of the linkage between burrowing events and sediment mixing.

5.4 DISCUSSION

5.4.1 Worm burrowing and sediment mixing

L. variegatus motion was highly heterogeneous. Although this organism is commonly described as an upward conveyor [*Landrum et al.*, 2002; *Lick*, 2006], we observed several distinct behaviors, including sediment excavation, particle ingestion/egestion, rapid reworking of interfacial sediments, and deep burrowing. Burrows were biased to the upper 10 mm of the bed (99.6% of events), which left extensive areas of the subsurface unaltered (Figure 5.2a). Marginal burrow-depth probabilities show that the majority of depths follow an exponential PDF. However, the infrequent deep burrowing events (0.4%) that rapidly transported sediments beyond 10 mm were not adequately described by this PDF, and were instead super-exponential. The marginal wait-time distribution contains a scale-free region from 1.5-200 h, illustrating a

wide range of times between revisits to a specific location. The lower limit of this distribution is expected to extend to the minute scale, since we observed frequent organism movements in images taken 3 min apart. Similarly, truncation at 200 h simply reflects the experiment duration, since the majority (64%) of the sediments between the SWI and the deepest burrow remained unperturbed at the end of the experiment.

Heterogeneous burrowing by *L. variegatus* resulted in anomalous sediment mixing. Deep burrow events immediately delivered tracer particles well below the SWI, illustrating that these very infrequent events significantly influenced the tracer distribution by transporting sediments nonlocally. Low tracer concentrations below 10 mm were visible in the 1-D fluorescence profiles by day 4 (Figure 5.4), even though worms had only reworked a small portion of these sediments: only 3% of sediments between 10-16 mm depth had been reworked at the end of the experiment. Mean and variance of the tracer concentration profiles increased steadily for the first 9 days of the experiment (Figure 5.5), and then continued to increase at a slower rate thereafter. A similar transition was observed in the SWI dynamics (Figure 5.3, red line). Time-lapse images show that worms created steadily-growing mounds of sediment during the first 9 days, displacing the SWI upward. Mounds collapsed after reaching a critical height and/or after disruption by worms. Mound growth and collapse equilibrated at day 9, leading to stochastic variations but no net increase in the SWI height after this time. The synchronous changes in tracer statistics and mean SWI height suggest that sediment mixing is directly linked to mound formation on the SWI, meaning propagation of particles is not only due to worm movements below the surface, but also deposition of egested and excavated particles at the SWI.

Sediment mixing by *L. variegatus* was also time dependent. Tracer particles initially propagated downward at a rate of 0.32 mm/d (Figure 5.5a), and propagation slowed to 0.04 mm/d after day 9. By this time worms had already reworked 86% of sediments above 5 mm. Subsequent sediment reworking near the SWI did not substantially alter tracer distributions, since tracer particles were well mixed in this region. Ongoing burrowing deeper in the sediments controlled downward tracer propagation at late times. The fraction of sediments reworked between 5-16 mm increased by 30% after day 9.

These results show that a minimum of several weeks are needed before a pulse of particles is well mixed in the zone of *L. variegatus* activity, which is an important consideration for sediment biogeochemistry [*Koelmans and Jonker*, 2011; *Kupryianchyk et al.*, 2013; *Lin et al.*, 2014; *Remaili et al.*, 2016]. In particular, our findings suggest that heterogeneous sediment reworking by bioturbating organisms strongly influences the timescale of response to natural and engineered perturbations. The infrequency of nonlocal bioturbation events leaves large areas of deep sediments unmixed for long periods of time, limiting interaction between new and pre-existing particles at these depths. This is expected to limit the timescale of response to sediment amendments for site remediation that require close contact between introduced particles and contaminated sediments [*Luthy et al.*, 1997; *Kosian et al.*, 1999; *Thibodeaux and Bierman*, 2003; *Dąbrowski et al.*, 2005; *Millward et al.*, 2005]. Nonlocal transport also can mobilize contaminated sediments from depth while effectively bypassing regions of sediment capping or amendment. The approach presented here can be used to predict conditions under which

introduced particles can be simply deposited on the SWI vs. conditions that require active mixing to ensure adequate contact with underlying contaminated sediments.

5.4.2 Sediment Transport Model

Our random walk model uniquely relates biophysical information to sediment mixing, utilizing statistics of organism motion acquired through a novel direct-visualization approach. The model's use of burrow statistics as a proxy for organism motion directly links sediment transport to the most relevant governing process (burrowing), as opposed to commonly-used bioturbation models that represent transport with assumed system-scale descriptive parameters, e.g., biodiffusion coefficient. The model specifically relates observations of burrow formation to sediment motion over all relevant spatial and temporal scales, which distinguishes it from local continuum models that are inherently limited to frequent small-scale motions. The classical biodiffusion model adequately captures the effects of frequent, local mixing events near the SWI, but does not represent intermittent tracer displacements to deep sediments or the associated transition from fast mixing of surficial sediments to slower mixing of deeper sediments. Models with a depth-dependent diffusion coefficient can improve fits to tracer data [*Christensen*, 1982; *Boudreau*, 2000], but they inherently cannot represent nonlocal transport and are non-transferrable because they are not explicitly related to the underlying motion processes. Conveyor-feeding models explicitly incorporate nonlocal particle displacements [*Boudreau*, 1986b; *Robbins*, 1986], but also do not capture the full range of sediment motion because they impose restrictions on the scales over which these displacements occur.

The random walk model presented here directly represents the effects of macroscopic organism motions. Application of the model to specific behavioral classes of organisms requires the development of rules that relate organism motion to sediment redistribution. For surface deposit feeders and other species regarded as true biodiffusors [*Robbins et al.*, 1979; *Maire et al.*, 2007; *Piot et al.*, 2008], organism motions homogenize sediments locally, yielding the classical biodiffusion model as an outcome. However, the general approach proposed here can represent sediment mixing caused by a much wider range of organism behaviors in a unified, fundamental theoretical framework. The specific transport rule developed for the oligochaete *Lumbriculus variegatus* is based on known behavior of the organism (head-down deposit feeder), as well as direct observations of burrowing events, mound formation, and tracer redistribution within the sediments. Burrowing statistics were obtained via direct visualization, and the fraction of sediments delivered to the SWI was obtained by measuring the accumulation of sediments on the SWI caused by burrow excavation and sediment egestion. The model provides a parsimonious description of key sediment mixing outcomes that are not captured by conventional biodiffusion models, including time-dependent burial and spreading of the tracer peak, long-term trends in the mean and variance of the tracer concentration profiles, and nonlocal mixing in deep sediments (Figure 5.4). This sediment redistribution rule is expected to apply to the general class of deposit feeding organisms historically considered surface feeders or conveyor-belt feeders [*Rhoads*, 1974; *Powell*, 1977; *Robbins*, 1986; *Kristensen et al.*, 2012], comprising many oligochaete and polychaete species [*McCall and Tevesz*, 1982; *Lopez and Levinton*, 1987; *Hutchings*, 1998; *Gérino et al.*, 2003], as well as gallery diffusers (e.g., *Nereis diversicolor*) and predators (e.g.,

Nephtys caeca) that mix sediments diffusively near the SWI and nonlocally at depth [*François et al.*, 2002; *Gérino et al.*, 2003; *Piot et al.*, 2008; *Pischedda et al.*, 2008]. The transport rule can be reformulated to represent other types of organism behavior. The model assumes that all sediments are equally likely to be remobilized, which is not expected to be the case for all organisms or sediments. For example, the oligochaete *Tubifex tubifex* is generally considered an upward conveyor (nonlocal transport) of fine (< 63 μm) sediments, but does not transport larger particles [*Mermillod-Blondin et al.*, 2001].

The model also assumes that all burrow events are independent and stationary (i.e., time invariant), implying that organism numbers and behavior do not change over time. These limitations are expected to be most severe for prediction of deeper and longer-term sediment mixing. For example, increased probability of organism revisits to existing burrows (as opposed to the formation of new burrows) and decreases in organism numbers over time will both lead to decreased mixing of deep sediments at late times. Further model generalization is therefore required to represent cases where burrowing activity varies with time. Future research efforts should explore extensions to represent nonstationarity and correlations related to time-varying worm populations and other population- and community-level changes in the benthic ecosystem, including species-pair interactions [*Kaster*; *Preisser et al.*, 2005], burrow network/gallery formation [*Ziebis et al.*, 1996; *Nogaro et al.*, 2006], and behavioral changes due to environmental cues (e.g., toxicity, temperature) [*Landrum et al.*, 2004; *Maire et al.*, 2007; *Sardo and Soares*, 2010].

5.5 Conclusions

The combined experimental and modeling approach introduced here simplifies model parameterization and improves transferability by relating input parameters to the most critical measurable system attributes. Future research is needed to elucidate the specific roles of sediment reworking and other biologically-mediated transport mechanisms (e.g., solute exchange via bioirrigation [*Kristensen et al.*, 2012]) in sediment biogeochemistry [*Mermillod-Blondin et al.*, 2004; *Pischedda et al.*, 2008; *Volkenborn et al.*, 2010]. These efforts will inform the proper coupling between transport and biogeochemical models—a necessary step for predicting responses to large-scale environmental pressures and designing successful site remediation strategies [*Lohrer et al.*, 2004; *Burton and Johnston*, 2010].

5.6 Supporting Information.

Time-lapse videos are available free of charge via the Internet at http://pubs.acs.org.

5.6.1 Sediment and Water Properties

Sediments were homogenized and analyzed several days prior to the experiment. Analysis methods and complete size distribution information is provided in *M W Xie et al.* [2015]. Bulk sediment properties are:

Table 5.1. Bulk characteristics of the Lake DePue sediments used in the experiments.

Porosity	49.3%	Permeability	$2.0 \pm 1.2 \times 10^{-14} \, m^2$
Organic C	3.09%	$[Zn^{2+}]$	14,000 mg/kg dry weight

Inorganic C	2.65%	[Cu^{2+}]	410 mg/kg dry weight

Artificially-reconstituted freshwater consisted of the following chemical constituents: 5 g

$CaSO_4$, 5 g $CaCl_2$, 3 g $MgSO_4$, 9.6 g $NaHCO_3$, 0.4 g KCl in 100 L of deionized water.

Burrow isolation algorithm

The following section of MATLAB script uses a Gaussian filter to smooth color images and

convert to binary.

```
% Load image
brwimg = imread(fullfile(photopath,brwname));


% Process image to extract burrows -
% brwimg is a 3-channel (RGB) jpeg image


% Use built-in MATLAB function imfilter
brwimg = imfilter(brwimg, fspecial('gaussian',5,2.5));


% Use built-in MATLAB function im2bw, with manually-chosen threshold 0.125
bstruct.burrows = im2bw(brwimg,.125);
```
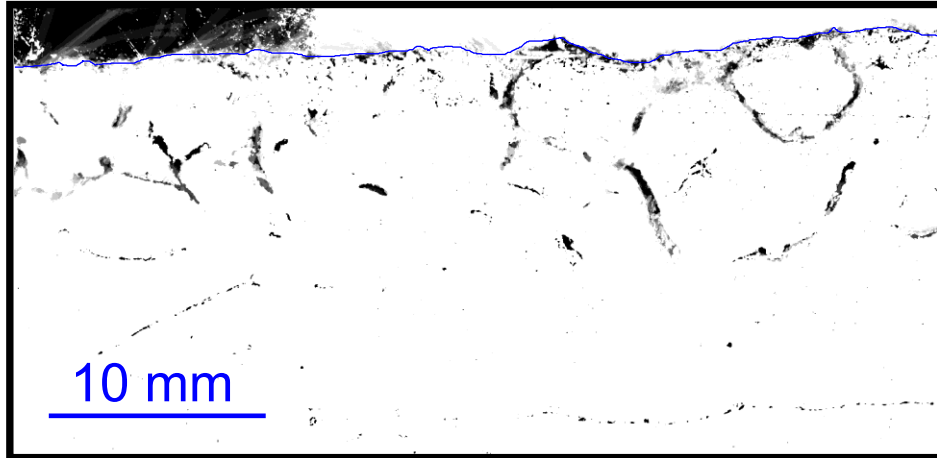
Figure 5.6. Example threshold image. Blue line denotes the sediment-water interface.

Sediment Transport Rule

For each burrowing event, tracer particles are redistributed according to the following rules: (1) The burrow depth X is partitioned into upper and lower sections; the upper section extends from the SWI to depth $f_p X$, where f_p is a fraction. (2) Pixels in the upper section are assigned a new tracer concentration equal to the average concentration in the lower section. (3) The remaining tracer particles are uniformly distributed over the remainder of the burrow, conserving mass.

We define the pile fraction f_p as the ratio of the mean SWI velocity (i.e., rate of SWI movement due to sediment reworking) to the characteristic burrow velocity derived from the marginal PDFs:

$$f_p = \frac{\Delta x_{SWI}/\Delta t_{growth}}{v_c} \qquad 5.8$$

where Δx_{SWI} is the rate of change in mean position of the SWI over time Δt_{growth}. The

characteristic burrow velocity v_c is calculated as the ratio of mean burrow depth to mean wait

time, calculated from λ and φ, respectively.

SWI velocity was found to be 0.18 mm/d for the initial period of linear growth (days 2-9). An

average burrow depth of 2.16 mm and wait time of 0.91 d were calculated from the marginal

densities, yielding a characteristic burrowing velocity of 2.25 mm/d. The pile fraction f_p,

calculated from equation S1, equaled 0.08.
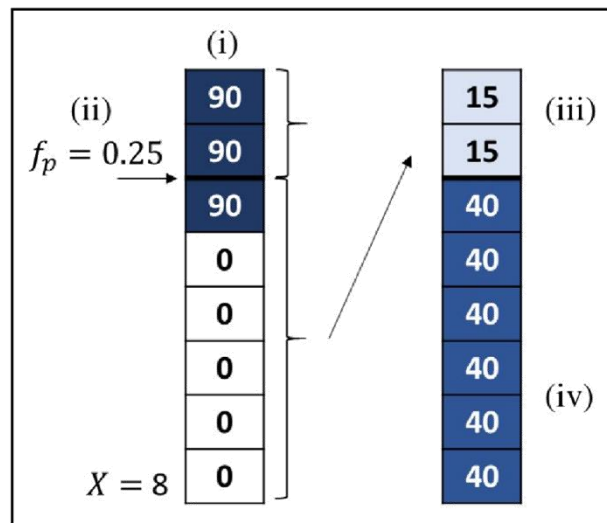
Figure 5.7. Example illustrating the tracer mixing algorithm used in the numerical model, for a burrow depht of 8 pixels and a burrow fraction of 0.25. Numbers within each pixel represent the fluorescence intensity (0-255). (i) A burrow depth X is sampled from λ; (ii) the burrow is partitioned into two sections, where the separation depth is designated by the pile fraction f_p ; (iii) the average pixel value in the lower section is assigned to pixels in the upper section; (iv) and the remaining pixels are populated to conserve mass.

5.6.2 Replicate fluorescence experiment.

We conducted replicate experiment in parallel with the one reported in the main text. Bulk fluorescence statistics for this experiment exhibit very similar trends (Figure 5.8). Mean and variance increased steadily for the first 10 d and then transitioned to much slower rates of increase. Burrowing distributions could not be measured in the second experiment because variability of the LED lighting produced an abundance of spurious burrowing events.
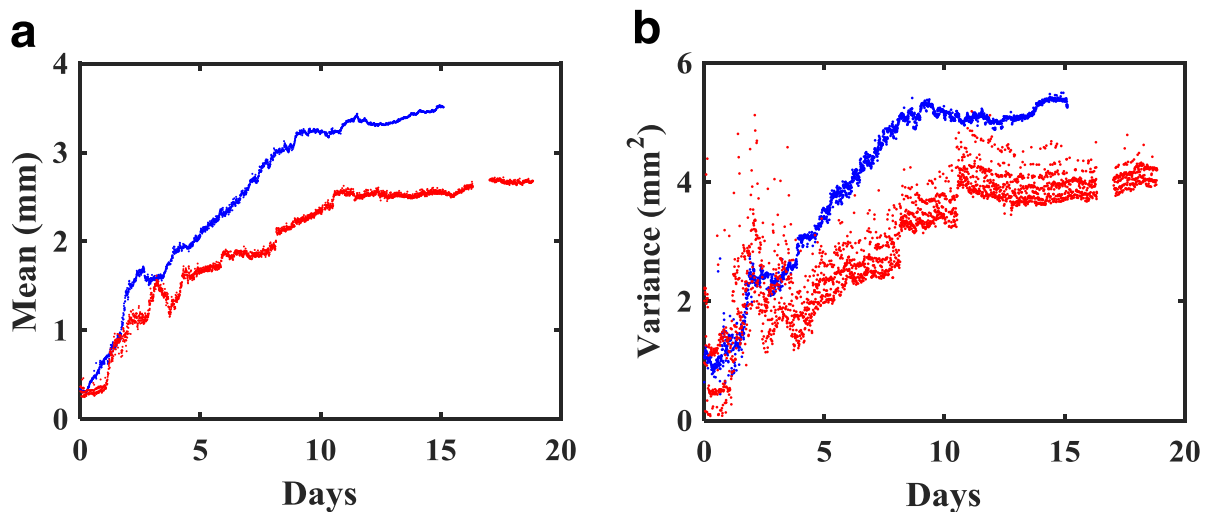
Figure 5.8. Time series for mean (a) and variance (b) for the experiment reported in the main text (blue dots) and a replicate fluorescent experiment (red dots). Large scatter in the time series in (b) is due to variability of the LED light source.
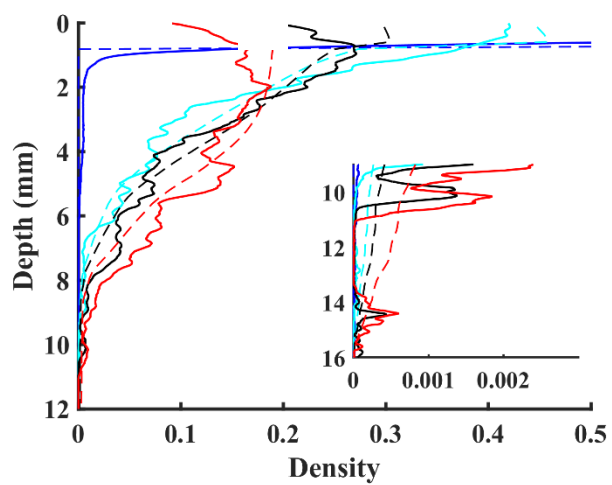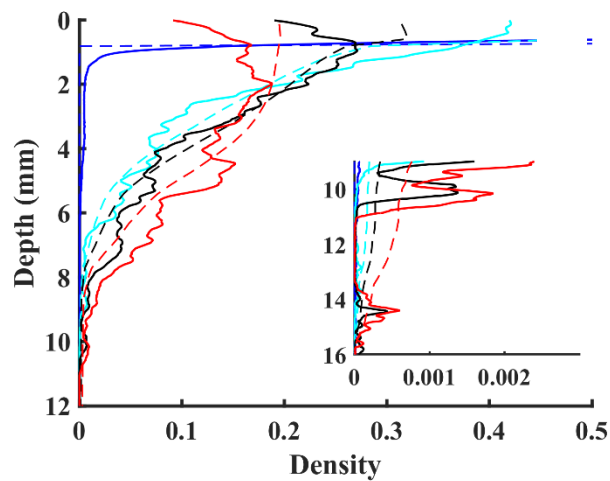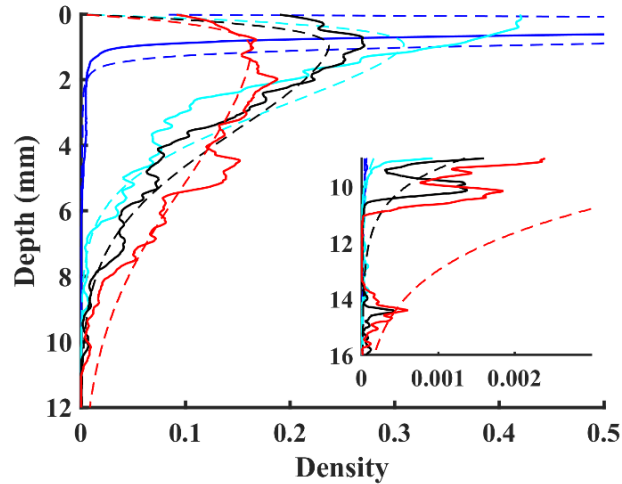
Figure 5.9. Comparison of particle densities across models. Fluorescence profiles from the experiment (—) and each model (– –) at different times; blue, cyan, black, and red lines are 0, 4, 7, and 15 d, respectively. (a) coupled random walk model, reproduced from the main text for ease of comparison. (b) random walk model with independent burrow-depth and wait-time distributions. (c) advection-diffusion model. This model provides good fits at early times but substantially overpredicts transport to deep sediments at late times.

CHAPTER 6

Conclusions

The fate of a wide range of reactive constituents is controlled by transport at and below the sediment-water interface. It is therefore critical that the physical processes controlling transport in this zone are understood and properly described in environmental transport models. The collection of studies presented here advances understanding of interfacial solute and fine particle transport by providing novel observations of several physical processes that regulate interfacial dynamics, and strategies for how these processes can be incorporated into multi-scale transport modeling frameworks.

6.1 Broader implications

Our findings clarify the range of spatial and temporal scales over which specific processes regulate interfacial transport. We show that commonly-employed assumptions about hyporheic mixing are violated when turbulence enhances mixing at the sediment-water interface (SWI). Rapid mixing at the SWI occurred over only 1-2 grain diameters (4-8 cm) in our hyporheic injection experiments. However, the rate of solute depletion in this zone dominated overall solute exchange in the streambed at early times, both at the local scale (Chapter 2) and at the scales commonly used to assess whole-stream transport (Chapter 3). A model that did not account for the spatial variability of vertical mixing could not describe local or integrated exchange rates. Further, we show in Chapter 2 that the magnitude of mixing and the spatial extent of this zone are directly related to turbulent momentum stresses in the hyporheic zone. This finding provides a stronger physical basis for the choice of hyporheic transport model in the field, provided the region of enhanced mixing can be properly characterized. Ultimately, improved transport

modeling will yield more accurate estimates of local reaction kinetics, since transport models are used directly to infer reaction rates from observed reactive tracer concentration distributions [*Harvey et al.*, 2013; *Boano et al.*, 2014].

We also show that the short-timescale concentration signature of turbulence varies in the hyporheic zone, both spatially and as a function of streamflow. This finding provides key information about the local hydrodynamic environment in the benthic and hyporheic zones. Given that turbulence is known to control benthic and hyporheic microbial metabolism [*Battin et al.*, 2003a; *Singer et al.*, 2010] and community structure [*Battin et al.*, 2003b; *Niederdorfer et al.*, 2016], the profile of turbulent mixing in these zones is a key predictor of both biogeochemical transformation and microbial diversity in streams.

Results from Chapter 4 demonstrate that the connection between hydrodynamic transport and microbial community structure is dynamic. The small-scale structure of benthic biofilms directly modifies retention of fine particles on the streambed. Since particle residence times can exceed one month [*Flood and Ashbolt*, 2000; *Drummond et al.*, 2014c], there exists an overlap between the timescales of particle retention and of biofilm growth. By quantifying the feedback between growth and retention, we provide a physical basis for assessing the range of times that simplified assumptions are valid in current transport models (e.g. stationarity of the wait-time distribution), as well as extend their capability to longer times by describing how the underlying transport mechanism will change. Our results strongly suggest that valuable information will be gained in

field studies that incorporate measures of biofilm structure, streambed particle counts, and multiple experiments timed over different stages of biofilm growth.

Sediment biomixing experiments (Chapter 5) show the implications of process heterogeneity. Burrow formation by *Lumbriculus variegatus* was frequent and highly localized to the SWI, with long intervals between burrowing events in deep sediments. This process spanned a broad range of spatial and temporal scales, resulting in rapid sediment mixing in some regions and unperturbed sediments in others. In the field, measurements of tracer movement at early times will likely not capture rare burrowing events, even though these events may be the most important for biogeochemical transformations or contaminant transport. In contrast, late-time measurements may show a fully mixed sediment layer, potentially leading to the improper conclusion that mixing is uniform across the bioactive zone. A predictive understanding of biomixing requires measurements that capture the full distribution transport events. We show in Chapter 5 that a combined experimental and modeling approach will aid in the measurement and modeling of this heterogeneous transport mechanism. Imaging experiments provide direct spatio-temporal information about the biological events controlling sediment transport, which can then be used directly in a sediment mixing model. This approach therefore provides valuable information that can be used to construct improved analytical and numerical models for field application that account for the intrinsic heterogeneity underlying the governing transport process.

6.2 General challenges and future directions

These four studies were motivated by the need for parsimonious models that predict solute and fine particle transport at the SWI. Numerous challenges remain before our specific findings can be incorporated into an integrated modeling framework. Hyporheic mixing experiments in Chapter 2 were performed in a system designed to yield high hyporheic turbulence (i.e., large sediments with open pores). Future experiments are needed to determine the range of sediment sizes, streambed geometries, and flow conditions over which turbulence will significantly impact hyporheic mass transport. Results from Chapters 2 and 3 suggest that enhanced mass transport is directly linked with the profile of turbulent stresses at and below the SWI. This provides a path forward to linking mechanistic models of hyporheic momentum transport and mass transport. Surface-subsurface flow coupling is nonlinear over a wide range of velocities and streambed permeabilities, and the complete, fundamental modeling of its nature remains a challenge [*Blois et al.*, 2013]. Nonetheless, predictive scaling relations of momentum transport are beginning to emerge that are based on measurable properties of the system (e.g., streambed permeability, shear stress) [*Ghisalberti*, 2009; *Manes et al.*, 2012; *Voermans et al.*, 2017]. Results from Chapter 2 suggest that these scaling relations are generally applicable to hyporheic mass transport, but future experiments are needed to validate this claim. Once validated, a model that predicts the coupled effects of streambed geometry and fluid flow will substantially improve current upscaled (i.e., regional- and continental-scale) assessments of transport and transformation [*Gomez‐Velez and Harvey*, 2014].

We show in Chapter 3 that enhanced mixing at the SWI alters the downstream evolution of an injected solute pulse, which is the most commonly used method to assess integrated, reach-scale mass transport in the field [*Haggerty et al.*, 2000; *Payn et al.*, 2008; *Hauer and Lamberti*, 2011; *Boano et al.*, 2014]. The interaction of several physically-based parameters—hyporheic velocity, the characteristic timescale for vertical hyporheic mixing, and distance from injection location—determined the shape of measured breakthrough curves. More simulations are needed to explore the full range of these interactions. A phase plot of physical parameters would reveal if there are specific combinations that will guarantee the emergence of an asymptotic power-law interval in a measured BTC. Such information would be highly valuable for field practitioners, since it could inform the proper field and experimental conditions needed to correctly infer hyporheic residence time distributions. Results could then be validated in a natural stream whose measurable attributes fall within the range of our parametric analysis. Future work is also needed to identify an analytical modeling framework that parsimoniously describes integrated transport in coarse-sediment streams. Such a framework must capture the highly correlated motions and narrow separation of velocity scales inherent to these systems—two attributes that violate the underlying assumptions of most current hyporheic transport models.

The flow-biofilm feedback identified in Chapter 4 highlights a general challenge for predicting solute and particle transport in fluvial systems: both transport processes and process interactions are active over a broad range of scales. Isolation of any individual process (or feedback) therefore does not provide complete information of the environmental controls of transport and transformation. This highlights the value of identifying the range of scales over

which specific processes are expected to control the system-scale behavior. Model results from Chapter 4 demonstrate that structural properties of benthic biofilms correlated with fine particle retention from minutes to months, which agrees with retention timescales observed in the field [*Drummond et al.*, 2014c]. However, since surface coverage, mean height, and biofilm roughness were all found to co-vary with particle retention here, finer-scale observations are needed to identify the main control of retention (e.g., biofilm surface chemistry, morphology, and porosity). Controls on fine-particle deposition also remain unresolved at the scales of biofilm heterogeneity and turbulent flow-biofilm interactions, as current biofilm imaging technology cannot capture biofilm-particle interactions at turbulent timescales. We anticipate that computational fluid dynamics models, which can potentially describe flow-structure interactions down to viscous length scales, will provide the most direct insights into these interactions until improved high-speed/high-resolution imaging technology emerges.

Results from Chapter 5 demonstrate that a key criterion of environmental transport models is that they capture the intrinsic process heterogeneity. Our *in situ* observations of sediment biomixing provide valuable insights into the structure of this heterogeneity by quantifying both the distribution of biological motions and the resulting sediment transport. However, advanced tools must be brought to bear to reduce this rich information to a parsimonious (and broadly applicable) description of sediment transport. The recent success of stochastic models for hydrodynamic transport suggests that this branch of mathematical physics may also provide analytically tractable descriptions of biological mixing [*Aquino et al.*, In Review]. Again, such a framework will improve the physical basis for model upscaling by explicitly accounting for

process heterogeneity, as well as providing the physical basis for development of multi-scale,

predictive reactive transport models.

CHAPTER 7

References

Aban, I. B., M. M. Meerschaert, and A. K. Panorska (2006), Parameter Estimation for the Truncated Pareto Distribution, *Journal of the American Statistical Association*, *101*, 270-277.

Akaike, H. (1974), A new look at the statistical model identification, *Automatic Control, IEEE Transactions on*, *19*, 716-723.

Allan, J. D., and M. M. Castillo (2007), *Stream Ecology: Structure and function of running waters*, 2 ed., Springer Science & Business Media, Dordrecht, The Netherlands.

Anderson, R. S., and S. P. Anderson (2010), *Geomorphology: the mechanics and chemistry of landscapes*, Cambridge University Press.

Aquino, T., A. Aubeneau, and D. Bolster (2015), Peak and tail scaling of breakthrough curves in hydrologic tracer tests, *Advances in Water Resources*, *78*, 1-8. doi: https://doi.org/10.1016/j.advwatres.2015.01.016.

Aquino, T., K. R. Roche, A. F. Aubeneau, A. I. Packman, and D. Bolster (In Review).

Arnon, S., L. P. Marx, K. E. Searcy, and A. I. Packman (2010), Effects of overlying velocity, particle size, and biofilm growth on stream--subsurface exchange of particles, *Hydrological Processes*, *24*, 108-114.

Aubeneau, A. F., B. Hanrahan, D. Bolster, and J. L. Tank (2014), Substrate size and heterogeneity control anomalous transport in small streams, *Geophysical Research Letters*, *41*, 8335-8341.

Aubeneau, A. F., B. Hanrahan, D. Bolster, and J. Tank (2016), Biofilm growth in gravel bed streams controls solute residence time distributions, *Journal of Geophysical Research: Biogeosciences*, *121*, 1840-1850. doi: 10.1002/2016JG003333.

Aubeneau, A. F., R. L. Martin, D. Bolster, R. Schumer, D. Jerolmack, and A. Packman (2015a), Fractal patterns in riverbed morphology produce fractal scaling of water storage times, *Geophysical Research Letters*, *42*, 5309-5315. doi: 10.1002/2015GL064155.

Aubeneau, A. F., J. D. Drummond, R. Schumer, D. Bolster, J. L. Tank, and A. I. Packman (2015b), Effects of benthic and hyporheic reactive transport on breakthrough curves, *Freshwater Science*, *34*, 301-315.

Aufdenkampe, A. K., E. Mayorga, P. A. Raymond, J. M. Melack, S. C. Doney, S. R. Alin, R. E. Aalto, and K. Yoo (2011), Riverine coupling of biogeochemical cycles between land, oceans, and atmosphere, *Frontiers in Ecology and the Environment*, *9*, 53-60.

Bardini, L., F. Boano, M. Cardenas, R. Revelli, and L. Ridolfi (2012a), Nutrient cycling in bedform induced hyporheic zones, *Geochimica et Cosmochimica Acta*, *84*, 47-61.

Bardini, L., F. Boano, M. B. Cardenas, R. Revelli, and L. Ridolfi (2012b), Nutrient cycling in bedform induced hyporheic zones, *Geochimica et Cosmochimica Acta*, *84*, 47 - 61.

Bastviken, D., L. J. Tranvik, J. A. Downing, P. M. Crill, and A. Enrich-Prast (2011), Freshwater Methane Emissions Offset the Continental Carbon Sink, *Science*, *331*, 50.

Battin, T. J., and D. Sengschmitt (1999), Linking Sediment Biofilms, Hydrodynamics, and River Bed Clogging: Evidence from a Large River, *Microbial Ecology*, *37*, 185-196.

Battin, T. J., L. A. Kaplan, J. D. Newbold, and C. M. Hansen (2003a), Contributions of microbial biofilms to ecosystem processes in stream mesocosms, *Nature*, *426*, 439-442.

Battin, T. J., L. A. Kaplan, J. D. Newbold, X. Cheng, and C. Hansen (2003b), Effects of current velocity on the nascent architecture of stream microbial biofilms, *Applied and Environmental Microbiology*, *69*, 5443-5452.

Battin, T. J., K. Besemer, M. M. Bengtsson, A. M. Romani, and A. I. Packmann (2016), The ecology and biogeochemistry of stream biofilms, *Nat Rev Micro*, *14*, 251-263. doi: 10.1038/nrmicro.2016.15.

Battin, T. J., S. Luyssaert, L. A. Kaplan, A. K. Aufdenkampe, A. Richter, and L. J. Tranvik (2009), The boundless carbon cycle, *Nature Geoscience*, *2*, 598-600.

Battin, T. J., W. T. Sloan, S. Kjelleberg, H. Daims, I. M. Head, T. P. Curtis, and L. Eberl (2007), Microbial landscapes: new paths to biofilm research, *Nature Reviews Microbiology*, *5*, 76-81.

Battin, T. J., L. A. Kaplan, S. Findlay, C. S. Hopkinson, E. Marti, A. I. Packman, J. D. Newbold, and F. Sabater (2008), Biophysical controls on organic carbon fluxes in fluvial networks, *Nature Geosci*, *1*, 95-100. doi: http://www.nature.com/ngeo/journal/v1/n2/suppinfo/ngeo101_S1.html.

Bear, J. (1979), *Hydraulics of groundwater*, Courier Corporation.

Bencala, K. E., and R. A. Walters (1983), Simulation of Solute Transport in a Mountain Pool-and-Riffle Stream - a Transient Storage Model, *Water Resources Research*, *19*, 718-724.

Benhamou, S. (2007), HOW MANY ANIMALS REALLY DO THE LÉVY WALK?, *Ecology*, *88*, 1962-1969. doi: 10.1890/06-1769.1.

Berkowitz, B., A. Cortis, M. Dentz, and H. Scher (2006), Modeling non-Fickian transport in geological formations as a continuous time random walk, *Reviews of Geophysics*, *44*.

Bernard, G., A. Grémare, O. Maire, P. Lecroart, F. J. Meysman, A. Ciutat, B. Deflandre, and J. C. Duchêne (2012), Experimental assessment of particle mixing fingerprints in the deposit-feeding bivalve Abra alba (Wood), *Journal of Marine Research*, *70*, 689-718.

Berner, R. A. (1980), *Early diagenesis: A theoretical approach*, Princeton University Press.

Besemer, K., G. Singer, I. Hödl, and T. J. Battin (2009), Bacterial community composition of stream biofilms in spatially variable-flow environments, *Applied and environmental microbiology*, *75*, 7189-7195.

Bessinger, B. A., D. Vlassopoulos, S. Serrano, and P. A. O'Day (2012), Reactive Transport Modeling of Subaqueous Sediment Caps and Implications for the Long-Term Fate of Arsenic, Mercury, and Methylmercury, *Aquatic Geochemistry*, *18*, 297-326. doi: 10.1007/s10498-012-9165-4.

Biggs, B. J. F. (1995), The contribution of flood disturbance, catchment geology and land use to the habitat template of periphyton in stream ecosystems, *Freshwater Biology*, *33*, 419-438. doi: 10.1111/j.1365-2427.1995.tb00404.x.

Biggs, B. J. F., V. I. Nikora, and T. H. Snelder (2005), Linking scales of flow variability to lotic ecosystem structure and function, *River Research and Applications*, *21*, 283-298. doi: 10.1002/rra.847.

Birjiniuk, A., N. Billings, E. Nance, J. Hanes, K. Ribbeck, and P. S. Doyle (2014), Single particle tracking reveals spatial and dynamic organization of the Escherichia coli biofilm matrix, *New journal of physics*, *16*, 085014.

Blois, G. L., G. H. Sambrook Smith, J. L. Best, R. J. Hardy, and J. R. Lead (2012), Quantifying the dynamics of flow within a permeable bed using time-resolved endoscopic particle imaging velocimetry (EPIV), *Experiments in Fluids*, *53*, 51???76.

Blois, G. L., J. L. Best, K. T. Christensen, R. J. Hardy, and G. H. S. Smith (2013), Coherent Flow Structures in the Pore Spaces of Permeable Beds Underlying a Unidirectional Turbulent Boundary Layer: A Review and Some New Experimental Results, in *Coherent Flow Structures at Earth's Surface*, edited, pp. 43-62, John Wiley & Sons, Ltd.

Boano, F., R. Revelli, and L. Ridolfi (2011), Water and solute exchange through flat streambeds induced by large turbulent eddies, *Journal of Hydrology*, *402*, 290-296.

Boano, F., A. Packman, A. Cortis, R. Revelli, and L. Ridolfi (2007), A continuous time random walk approach to the stream transport of solutes, *Water Resources Research*, *43*, W10425.

Boano, F., J. W. Harvey, A. Marion, A. I. Packman, R. Revelli, L. Ridolfi, and A. Wörman (2014), Hyporheic flow and transport processes: Mechanisms, models, and biogeochemical implications, *Reviews of Geophysics*, *52*, 603-679.

Bolster, D., Y. Méheust, T. Le Borgne, J. Bouquain, and P. Davy (2014), Modeling preasymptotic transport in flows with significant inertial and trapping effects–The importance of velocity correlations and a spatial Markov model, *Advances in Water Resources*, *70*, 89-103.

Bottacin-Busolin, A., and A. Marion (2010), Combined role of advective pumping and mechanical dispersion on time scales of bed form–induced hyporheic exchange, *Water Resources Research*, *46*, n/a-n/a. doi: 10.1029/2009WR008892.

Bottacin-Busolin, A., G. Singer, M. Zaramella, T. J. Battin, and A. Marion (2009), Effects of Streambed Morphology and Biofilm Growth on the Transient Storage of Solutes, *Environmental Science & Technology*, *43*, 7337-7342.

Boudreau, B. P. (1986a), Mathematics of tracer mixing in sediments: II. Nonlocal mixing and biological conveyor-belt phenomena, *Am. J. Sci*, *286*, 199-238.

Boudreau, B. P. (1986b), Mathematics of tracer mixing in sediments; I, Spatially-dependent, diffusive mixing, *American Journal of Science*, *286*, 161-198.

Boudreau, B. P. (2000), The mathematics of early diagenesis: From worms to waves, *Reviews of Geophysics*, *38*, 389-416.

Boudreau, B. P., and B. B. Jorgensen (2001), The benthic boundary layer: Transport processes and biogeochemistry, edited, Oxford University Press.

Boulêtreau, S., F. Garbétian, S. Sauvage, and J.-M. Sánchez-Pérez (2006), Assessing the importance of a self-generated detachment process in river biofilm models, *Freshwater Biology*, *51*, 901-912.

Boulton, A. J., S. Findlay, P. Marmonier, E. H. Stanley, and H. M. Valett (1998), The functional significance of the hyporheic zone in streams and rivers, *Annual Review of Ecology and Systematics*, *29*, 59-81. doi: 10.1146/annurev.ecolsys.29.1.59.

Bouwer, E. J. (1987), Theoretical investigation of particle deposition in biofilm systems, *Water Research*, *21*, 1489-1498.

Breugem, W. P., B. J. Boersma, and R. E. Uittenbogaard (2006), The influence of wall permeability on turbulent channel flow, *Journal of Fluid Mechanics*, *562*, 35-72.

Brinkhurst, R. O. (1970), Distribution and Abundance of Tubificid (Oligochaeta) Species in Toronto Harbour, Lake Ontario, *Journal of the Fisheries Research Board of Canada*, *27*, 1961-1969. doi: 10.1139/f70-220.

Burton, G. A., and E. L. Johnston (2010), Assessing contaminated sediments in the context of multiple stressors, *Environmental Toxicology and Chemistry*, *29*, 2625-2643. doi: 10.1002/etc.332.

Canavan, R. W., C. P. Slomp, P. Jourabchi, P. Van Cappellen, A. M. Laverman, and G. A. van den Berg (2006), Organic matter mineralization in sediment of a coastal freshwater lake and response to salinization, *Geochimica et Cosmochimica Acta*, *70*, 2836-2855. doi: http://dx.doi.org/10.1016/j.gca.2006.03.012.

Cardenas, M. B. (2015), Hyporheic zone hydrologic science: A historical account of its emergence and a prospectus, *Water Resources Research*.

Cardenas, M. B., and J. L. Wilson (2007), Dunes, turbulent eddies, and interfacial exchange with permeable sediments, *Water Resources Research*, *43*.

Cardinale, B. J., M. A. Palmer, C. M. Swan, S. Brooks, and N. L. Poff (2002), The influence of substrate heterogeneity on biofilm metabolism in a stream ecosystem, *Ecology*, *83*, 412-422.

Carpenter, S. R., E. H. Stanley, and M. J. Vander Zanden (2011), State of the world's freshwater ecosystems: physical, chemical, and biological changes, *Annual review of Environment and Resources*, *36*, 75-99.

Chandesris, M., A. D'Hueppe, B. Mathieu, D. Jamet, and B. Goyeau (2013), Direct numerical simulation of turbulent heat transfer in a fluid-porous domain, *Physics of Fluids (1994-present)*, *25*, 125110.

Chandler, I. D., I. Guymer, J. M. Pearson, and R. van Egmond (2016), Vertical variation of mixing within porous sediment beds below turbulent flows, *Water Resources Research*, *52*, 3493-3509. doi: 10.1002/2015WR018274.

Christensen, E. R. (1982), A model for radionuclides in sediments influenced by mixing and compaction, *Journal of Geophysical Research: Oceans*, *87*, 566-572. doi: 10.1029/JC087iC01p00566.

Ciutat, A., and A. Boudou (2003), Bioturbation effects on cadmium and zinc transfers from a contaminated sediment and on metal bioavailability to benthic bivalves, *Environmental Toxicology and Chemistry*, *22*, 1574-1581.

Coco, G., S. F. Thrush, M. O. Green, and J. E. Hewitt (2006), Feedbacks between bivalve density, flow, and suspended sediment concentration on patch stable states, *Ecology*, *87*, 2862-2870.

Cook, D. G., and M. G. Johnson (1974), Benthic Macroinvertebrates of the St. Lawrence Great Lakes, *Journal of the Fisheries Research Board of Canada*, *31*, 763-782. doi: 10.1139/f74-101.

Cortis, A., and B. Berkowitz (2005), Computing "anomalous" contaminant transport in porous media: The CTRW MATLAB toolbox, *Groundwater*, *43*, 947-950.

Costerton, J. W., Z. Lewandowski, D. E. Caldwell, D. R. Korber, and H. M. Lappin-Scott (1995), Microbial Biofilms, *Annual Review of Microbiology*, *49*, 711-745.

Cushing, C. E., G. W. Minshall, and J. D. Newbold (1993), Transport dynamics of fine particulate organic matter in two Idaho streams, *Limnology and Oceanography*, *38*, 1101-1115.

Cuthbert, M. O., R. Mackay, V. Durand, M. F. Aller, R. B. Greswell, and M. O. Rivett (2010), Impacts of river bed gas on the hydraulic and thermal dynamics of the hyporheic zone, *Advances in Water Resources*, *33*, 1347-1358. doi: http://dx.doi.org/10.1016/j.advwatres.2010.09.014.

Dąbrowski, A., P. Podkościelny, Z. Hubicki, and M. Barczak (2005), Adsorption of phenolic compounds by activated carbon—a critical review, *Chemosphere*, *58*, 1049-1070. doi: http://dx.doi.org/10.1016/j.chemosphere.2004.09.067.

de Anna, P., T. Le Borgne, M. Dentz, A. M. Tartakovsky, D. Bolster, and P. Davy (2013), Flow Intermittency, Dispersion, and Correlated Continuous Time Random Walks in Porous Media, *Physical Review Letters*, *110*, 184502.

de Hoog, F., J. Knight, and A. Stokes (1982), An Improved Method for Numerical Inversion of Laplace Transforms, *SIAM Journal on Scientific and Statistical Computing*, *3*, 357-366.

Dentz, M., P. K. Kang, A. Comolli, T. Le Borgne, and D. R. Lester (2016), Continuous time random walks for the evolution of Lagrangian velocities, *Physical Review Fluids*, *1*, 074004.

Diaz, R. J., and R. Rosenberg (2008), Spreading dead zones and consequences for marine ecosystems, *science*, *321*, 926-929.

DiCesare, E. A. W., B. R. Hargreaves, and K. L. Jellison (2012), Biofilm Roughness Determines Cryptosporidium parvum Retention in Environmental Biofilms, *Applied and Environmental Microbiology*, *78*, 4187-4193. doi: 10.1128/aem.08026-11.

Dimock, R., and E. Morgenroth (2006), The influence of particle size on microbial hydrolysis of protein particles in activated sludge, *Water Research*, *40*, 2064-2074. doi: http://dx.doi.org/10.1016/j.watres.2006.03.011.

Drummond, J., A. Aubeneau, and A. Packman (2014a), Stochastic modeling of fine particulate organic carbon dynamics in rivers, *Water Resources Research*, *50*, 4341-4356.

Drummond, J., T. Covino, A. Aubeneau, D. Leong, S. Patil, R. Schumer, and A. Packman (2012), Effects of solute breakthrough curve tail truncation on residence time estimates: A synthesis of solute tracer injection studies, *Journal of Geophysical Research: Biogeosciences (2005--2012)*, *117*.

Drummond, J., R. J. Davies-Colley, R. Stott, J. P. Sukias, J. W. Nagels, A. Sharp, and A. I. Packman (2014b), Retention and remobilization dynamics of fine particles and microorganisms in pastoral streams, *Water Research*, *66*, 459-472. doi: http://dx.doi.org/10.1016/j.watres.2014.08.025.

Drummond, J., R. Davies-Colley, R. Stott, J. Sukias, J. Nagels, A. Sharp, and A. Packman (2014c), Retention and remobilization dynamics of fine particles and microorganisms in pastoral streams, *water research*, *66*, 459-472.

Drury, W. J., P. S. Stewart, and W. G. Characklis (1993a), Transport of 1-μm latex particles in pseudomonas aeruginosa biofilms, *Biotechnology and Bioengineering*, *42*, 111-117. doi: 10.1002/bit.260420115.

Drury, W. J., W. G. Characklis, and P. S. Stewart (1993b), Interactions of 1 μm latex particles with pseudomonas aeruginosa biofilms, *Water Research*, *27*, 1119-1126.

Elder, J. (1959), The dispersion of marked fluid in turbulent shear flow, *Journal of fluid mechanics*, *5*, 544-560.

Elliott, A. H., and N. H. Brooks (1997a), Transfer of nonsorbing solutes to a streambed with bed forms: Theory, *Water Resources Research*, *33*, 123-136.

Elliott, A. H., and N. H. Brooks (1997b), Transfer of nonsorbing solutes to a streambed with bed forms: Laboratory experiments, *Water Resources Research*, *33*, 137-151.

Ensign, S. H., and M. W. Doyle (2005), In-channel transient storage and associated nutrient retention: Evidence from experimental manipulations, *Limnology and Oceanography*, *50*, 1740-1751. doi: 10.4319/lo.2005.50.6.1740.

Feller, W. (2008), *An introduction to probability theory and its applications*, John Wiley & Sons.

Fellows, C. S., H. M. Valett, C. N. Dahm, P. J. Mulholland, and S. A. Thomas (2006), Coupling Nutrient Uptake and Energy Flow in Headwater Streams, *Ecosystems*, *9*, 788-804. doi: 10.1007/s10021-006-0005-5.

Fischer, H. B., J. E. List, C. R. Koh, J. Imberger, and N. H. Brooks (1979), Mixing in inland and coastal waters.

Fisher, S. G., and G. E. Likens (1973), Energy Flow in Bear Brook, New Hampshire: An Integrative Approach to Stream Ecosystem Metabolism, *Ecological Monographs*, *43*, 421-439. doi: 10.2307/1942301.

Flemming, H.-C., and J. Wingender (2010), The biofilm matrix, *Nature Reviews Microbiology*, *8*, 623-633.

Flemming, H.-C., J. Wingender, U. Szewzyk, P. Steinberg, S. A. Rice, and S. Kjelleberg (2016), Biofilms: an emergent form of bacterial life, *Nat Rev Micro*, *14*, 563-575. doi: 10.1038/nrmicro.2016.94.

Flood, J., and N. Ashbolt (2000), Virus-sized particles are concentrated and maintained within wastewater wetland biofilms, *Advances in Environmental Research*, *3*, 403-411.

Fogg, G. E., and Y. Zhang (2016), Debates—Stochastic subsurface hydrology from theory to practice: A geologic perspective, *Water Resources Research*, *52*, 9235-9245. doi: 10.1002/2016WR019699.

Foufoula-Georgiou, E., and C. Stark (2010), Introduction to special section on Stochastic Transport and Emergent Scaling on Earth's Surface: Rethinking geomorphic transport—Stochastic theories, broad scales of motion and nonlocality, *Journal of Geophysical Research: Earth Surface*, *115*, n/a-n/a. doi: 10.1029/2010JF001661.

Fox, A., F. Boano, and S. Arnon (2014), Impact of losing and gaining streamflow conditions on hyporheic exchange fluxes induced by dune- shaped bed forms, *Water Resources Research*, *50*, 1895-1907.

François, F., J.-C. Poggiale, J.-P. Durbec, and G. Stora (1997), A new approach for the modelling of sediment reworking induced by a macrobenthic community, *Acta Biotheoretica*, *45*, 295-319.

François, F., M. Gerino, G. Stora, J.-P. Durbec, and J.-C. Poggiale (2002), Functional approach to sediment reworking by gallery-forming macrobenthic organisms: modeling and application with the polychaete Nereis diversicolor, *Marine Ecology Progress Series*, *229*, 127-136.

Freeze, R. A., and J. A. Cherry (1979), Groundwater, *Printice-Hall, New Jersey*.

Gelhar, L. W., C. Welty, and K. R. Rehfeldt (1992), A critical review of data on field-scale dispersion in aquifers, *Water Resources Research*, *28*, 1955-1974. doi: 10.1029/92WR00607.

Gérino, M., G. Stora, F. François-Carcaillet, F. Gilbert, J.-C. Poggiale, F. Mermillod-Blondin, G. Desrosiers, and P. Vervier (2003), Macro-invertebrate functional groups in freshwater and marine sediments: a common mechanistic classification, *Vie et Milieu*, *53*, 221-231.

Ghisalberti, M. (2009), Obstructed shear flows: similarities across systems and scales, *Journal of Fluid Mechanics*, *641*, 51-61.

Ghisalberti, M., and H. Nepf (2005), Mass Transport in Vegetated Shear Flows, *Environmental Fluid Mechanics*, *5*, 527-551. doi: 10.1007/s10652-005-0419-1.

Goldberg, E. D., and M. Koide (1962), Geochronological studies of deep sea sediments by the ionium/thorium method, *Geochimica et Cosmochimica Acta*, *26*, 417-450.

Gomez‑Velez, J. D., and J. W. Harvey (2014), A hydrogeomorphic river network model predicts where and why hyporheic exchange is important in large basins, *Geophysical Research Letters*, *41*, 6403-6412.

Gomi, T., R. C. Sidle, and J. S. Richardson (2002), Understanding Processes and Downstream Linkages of Headwater Systems, *BioScience*, *52*, 905-916.

Gooseff, M. N., J. LaNier, R. Haggerty, and K. Kokkeler (2005), Determining in-channel (dead zone) transient storage by comparing solute transport in a bedrock channel--alluvial channel sequence, Oregon, *Water Resources Research*, *41*.

Goring, D., and V. Nikora (2002), Despiking Acoustic Doppler Velocimeter Data, *Journal of Hydraulic Engineering*, *128*, 117-126.

Grant, S. B., M. J. Stewardson, and I. Marusic (2012), Effective diffusivity and mass flux across the sediment-water interface in streams, *Water Resources Research*, *48*, n/a-n/a. doi: 10.1029/2011WR011148.

Guinasso, N. L., and D. R. Schink (1975), Quantitative estimates of biological mixing rates in abyssal sediments, *Journal of Geophysical Research*, *80*, 3032-3043.

Haggerty, R., S. A. McKenna, and L. C. Meigs (2000), On the late-time behavior of tracer test breakthrough curves, *Water Resources Research*, *36*, 3467-3479.

Haggerty, R., S. M. Wondzell, and M. A. Johnson (2002), Power-law residence time distribution in the hyporheic zone of a 2nd-order mountain stream, *Geophysical Research Letters*, *29*, 18-11.

Hall, R. J. O., E. S. Bernhardt, and G. E. Likens (2002), Relating nutrient uptake with transient storage in forested mountain streams, *Limnology and Oceanography*, *47*, 255-265.

Harvey, J. W., and C. C. Fuller (1998), Effect of enhanced manganese oxidation in the hyporheic zone on basin-scale geochemical mass balance, *Water Resources Research*, *34*, 623-636. doi: 10.1029/97WR03606.

Harvey, J. W., B. J. Wagner, and K. E. Bencala (1996), Evaluating the reliability of the stream tracer approach to characterize stream-subsurface water exchange, *Water Resources Research*, *32*, 2441-2451.

Harvey, J. W., J. K. Böhlke, M. A. Voytek, D. Scott, and C. R. Tobias (2013), Hyporheic zone denitrification: Controls on effective reaction depth and contribution to whole-stream mass balance, *Water Resources Research*, *49*, 6298-6316.

Harvey, J. W., et al. (2012), Hydrogeomorphology of the hyporheic zone: Stream solute and fine particle interactions with a dynamic streambed, *Journal of Geophysical Research: Biogeosciences (2005--2012)*, *117*.

Hauer, F. R., and G. A. Lamberti (2011), *Methods in stream ecology*, Academic Press.

Hester, E. T., M. B. Cardenas, R. Haggerty, and S. V. Apte (2017), The importance and challenge of hyporheic mixing, *Water Resources Research*, *53*, 3565-3575.

Higashino, M., J. J. Clark, and H. G. Stefan (2009), Pore water flow due to near-bed turbulence and associated solute transfer in a stream or lake sediment bed, *Water Resources Research*, *45*, n/a-n/a.

Hondzo, M., and H. Wang (2002), Effects of turbulence on growth and metabolism of periphyton in a laboratory flume, *Water Resources Research*, *38*, 13-11-13-19. doi: 10.1029/2002WR001409.

Huang, D., E. A. Swanson, C. P. Lin, J. S. Schuman, W. G. Stinson, W. Chang, M. R. Hee, T. Flotte, K. Gregory, and C. A. Puliafito (1991), Optical coherence tomography, *Science (New York, NY)*, *254*, 1178.

Huettel, M., and G. Gust (1992), Solute release mechanisms from confined sediment cores in stirred benthic chambers and flume flows, *Marine ecology progress series. Oldendorf*, *82*, 187-197.

Huettel, M., W. Ziebis, and S. Forster (1996), Flow-induced uptake of particulate matter in permeable sediments, *Limnology and Oceanography*, *41*, 309-322.

Hunter, W. R., R. Niederdorfer, A. Gernand, B. Veuger, J. Prommer, M. Mooshammer, W. Wanek, and T. J. Battin (2016), Metabolism of mineral-sorbed organic matter depends upon microbial lifestyle in fluvial ecosystems, *Geophysical Research Letters*, *43*, 1582-1588. doi: 10.1002/2016GL067719.

Hutchings, P. (1998), Biodiversity and functioning of polychaetes in benthic sediments, *Biodiversity & Conservation*, *7*, 1133-1145. doi: 10.1023/a:1008871430178.

Jackson, T. R., R. Haggerty, and S. V. Apte (2013), A fluid-mechanics based classification scheme for surface transient storage in riverine environments: quantitatively separating surface from hyporheic transient storage.

Jones, J. B., and P. J. Mulholland (1999), *Streams and Ground Waters*, Academic Press, San Diego, CA.

Kang, P. K., M. Dentz, T. Le Borgne, and R. Juanes (2011), Spatial Markov model of anomalous transport through random lattice networks, *Physical review letters*, *107*, 180602.

Kang, P. K., T. Le Borgne, M. Dentz, O. Bour, and R. Juanes (2015), Impact of velocity correlation and distribution on transport in fractured media: Field evidence and theoretical model, *Water Resources Research*, *51*, 940-959. doi: 10.1002/2014WR015799.

Karwan, D. L., and J. E. Saiers (2012), Hyporheic exchange and streambed filtration of suspended particles, *Water Resources Research*, *48*, n/a-n/a. doi: 10.1029/2011WR011173.

Kaster, J. L. Observations of predator-prey interaction on dispersal of an oligochaete prey, Limnodrilus hoffmeisteri, *Hydrobiologia*, *180*, 191-193. doi: 10.1007/bf00027552.

Klafter, J., and I. M. Sokolov (2005), Anomalous diffusion spreads its wings, *Physics world*, *18*, 29.

Koelmans, A. A., and M. T. O. Jonker (2011), Effects of black carbon on bioturbation-induced benthic fluxes of polychlorinated biphenyls, *Chemosphere*, *84*, 1150 - 1157.

Kosian, P. A., C. W. West, M. S. Pasha, J. S. Cox, D. R. Mount, R. J. Huggett, and G. T. Ankley (1999), Use of nonpolar resin for reduction of fluoranthene bioavailability in sediment, *Environmental Toxicology and Chemistry*, *18*, 201-206. doi: 10.1002/etc.5620180215.

Kristensen, E., G. Penha-Lopes, M. Delefosse, T. Valdemarsen, C. O. Quintana, and G. T. Banta (2011), What is bioturbation? The need for a precise definition for fauna in aquatic sciences, *Marine Ecology Progress Series*, *446*, 285-302.

Kristensen, E., G. Penha-Lopes, M. Delefosse, T. Valdemarsen, C. O. Quintana, and G. T. Banta (2012), What is bioturbation? The need for a precise definition for fauna in aquatic sciences, *Marine Ecology Progress Series*, *446*, 285-302.

Kupryianchyk, D., A. Noori, M. I. Rakowska, J. T. C. Grotenhuis, and A. A. Koelmans (2013), Bioturbation and Dissolved Organic Matter Enhance Contaminant Fluxes from Sediment Treated with Powdered and Granular Activated Carbon, *Environmental Science & Technology*, *47*, 5092-5100.

Lampert, D. J., and D. Reible (2009), An Analytical Modeling Approach for Evaluation of Capping of Contaminated Sediments, *Soil and Sediment Contamination: An International Journal*, *18*, 470-488.

Landrum, P. F., M. Gedeon, G. Burton, M. Greenberg, and C. Rowland (2002), Biological responses of Lumbriculus variegatus exposed to fluoranthene-spiked sediment, *Archives of environmental contamination and toxicology*, *42*, 292-302.

Landrum, P. F., M. Leppänen, S. D. Robinson, D. C. Gossiaux, G. A. Burton, M. Greenberg, J. V. K. Kukkonen, B. J. Eadie, and M. B. Lansing (2004), Effect of 3,4,3,4'-tetrachlorobiphenyl on the reworking behavior of Lumbriculus variegatus exposed to contaminated sediment, *Environmental Toxicology and Chemistry*, *23*, 178-186. doi: 10.1897/03-104.

Larned, S. T., V. I. Nikora, and B. J. Biggs (2004), Mass-transfer-limited nitrogen and phosphorus uptake by stream periphyton: A conceptual model and experimental evidence, *Limnology and Oceanography*, *49*, 1992-2000.

Larned, S. T., A. I. Packman, D. R. Plew, and K. Vopel (2011), Interactions between the mat-forming alga Didymosphenia geminata and its hydrodynamic environment, *Limnology & Oceanography: Fluids & Environment*, *1*, 4-22.

Larsen, L. G., and J. W. Harvey (2010), How Vegetation and Sediment Transport Feedbacks Drive Landscape Change in the Everglades and Wetlands Worldwide, *The American Naturalist*, *176*, E66-E79. doi: 10.1086/655215.

Lauritsen, D. D., S. C. Mozley, and D. S. White (1985), Distribution of Oligochaetes in Lake Michigan and Comments on Their use as Indices of Pollution, *Journal of Great Lakes Research*, *11*, 67-76. doi: http://dx.doi.org/10.1016/S0380-1330(85)71745-5.

Lawrence, J. E., M. E. Skold, F. A. Hussain, D. R. Silverman, V. H. Resh, D. L. Sedlak, R. G. Luthy, and J. E. McCray (2013), Hyporheic Zone in Urban Streams: A Review and Opportunities for Enhancing Water Quality and Improving Aquatic Habitat by Active Management, *Environmental Engineering Science*, *30*, 480-501. doi: 10.1089/ees.2012.0235.

Le Borgne, T., M. Dentz, and J. Carrera (2008), Lagrangian Statistical Model for Transport in Highly Heterogeneous Velocity Fields, *Physical Review Letters*, *101*, 090601.

Lehmann, M. F., S. M. Bernasconi, A. Barbieri, and J. A. McKenzie (2002), Preservation of organic matter and alteration of its carbon and nitrogen isotope composition during simulated and in situ early sedimentary diagenesis, *Geochimica et Cosmochimica Acta*, *66*, 3573-3584. doi: http://dx.doi.org/10.1016/S0016-7037(02)00968-7.

Leopold, L. B., M. G. Wolman, and J. P. Miller (1964), *Fluvial processes in geomorphology*, Courier Corporation.

Li, A., A. F. Aubeneau, D. Bolster, J. L. Tank, and A. I. Packman (2017), Covariation in patterns of turbulence-driven hyporheic flow and denitrification enhances reach-scale nitrogen removal, *Water Resources Research*. doi: 10.1002/2016WR019949.

Lick, W. (2006), The Sediment-Water Flux of HOCs Due to "Diffusion" or Is There a Well-Mixed Layer? If There Is, Does It Matter?, *Environmental Science & Technology*, *40*, 5610-5617.

Lightbody, A. F., and H. M. Nepf (2006), Prediction of velocity profiles and longitudinal dispersion in salt marsh vegetation, *Limnology and Oceanography*, *51*, 218-228. doi: 10.4319/lo.2006.51.1.0218.

Lin, D., Y.-M. Cho, D. Werner, and R. G. Luthy (2014), Bioturbation Delays Attenuation of DDT by Clean Sediment Cap but Promotes Sequestration by Thin-Layered Activated Carbon, *Environmental Science & Technology*, *48*, 1175-1183. doi: 10.1021/es404108h.

Lock, M. A., and D. D. Williams (1981), River epilithon—a light and organic energy transducer, in *Perspectives in Running Water Ecology*, edited by M. A. Lock, pp. 3-40, Springer, New York, New York.

Lohrer, A. M., S. F. Thrush, and M. M. Gibbs (2004), Bioturbators enhance ecosystem function through complex biogeochemical interactions, *Nature*, *431*, 1092-1095.

Lopez, G. R., and J. S. Levinton (1987), Ecology of Deposit-Feeding Animals in Marine Sediments, *The Quarterly Review of Biology*, *62*, 235-260.

Luthy, R. G., G. R. Aiken, M. L. Brusseau, S. D. Cunningham, P. M. Gschwend, J. J. Pignatello, M. Reinhard, S. J. Traina, W. J. Weber, and J. C. Westall (1997), Sequestration of Hydrophobic Organic Contaminants by Geosorbents, *Environmental Science & Technology*, *31*, 3341-3347. doi: 10.1021/es970512m.

Maire, O., J. Duchêne, A. Grémare, V. Malyuga, and F. Meysman (2007), A comparison of sediment reworking rates by the surface deposit-feeding bivalve Abra ovata during summertime and wintertime, with a comparison between two models of sediment reworking, *Journal of Experimental Marine Biology and Ecology*, *343*, 21-36.

Manes, C., L. Ridolfi, and G. Katul (2012), A phenomenological model to describe turbulent friction in permeable-wall flows, *Geophysical Research Letters*, *39*, n/a-n/a. doi: 10.1029/2012GL052369.

Manes, C., D. Pokrajac, I. McEwan, and V. Nikora (2009), Turbulence structure of open channel flows over permeable and impermeable beds: A comparative study, *Physics of Fluids (1994-present)*, *21*, -.

Manes, C., D. Pokrajac, V. Nikora, L. Ridolfi, and D. Poggi (2011), Turbulent friction in flows over permeable walls, *Geophysical Research Letters*, *38*.

Margolin, G., M. Dentz, and B. Berkowitz (2003), Continuous time random walk and multirate mass transfer modeling of sorption, *Chemical physics*, *295*, 71-80.

Marion, A., A. I. Packman, M. Zaramella, and A. Bottacin-Busolin (2008), Hyporheic flows in stratified beds, *Water Resources Research*, *44*, n/a-n/a. doi: 10.1029/2007WR006079.

Marion, A., et al. (2014), Aquatic interfaces: a hydrodynamic and ecological perspective, *Journal of Hydraulic Research*, *52*, 744-758. doi: 10.1080/00221686.2014.968887.

Martin, R. L., D. J. Jerolmack, and R. Schumer (2012), The physical basis for anomalous diffusion in bed load transport, *Journal of Geophysical Research: Earth Surface*, *117*, n/a-n/a. doi: 10.1029/2011JF002075.

Marzadri, A., D. Tonina, and A. Bellin (2011), A semianalytical three‐dimensional process‐based model for hyporheic nitrogen dynamics in gravel bed rivers, *Water Resources Research*, *47*.

McCall, P. L., and M. J. Tevesz (1982), *The effects of benthos on physical properties of freshwater sediments*, Springer.

McClain, M. E., et al. (2003), Biogeochemical Hot Spots and Hot Moments at the Interface of Terrestrial and Aquatic Ecosystems, *Ecosystems*, *6*, 301-312.

McNair, J. N., and J. D. Newbold (2012), Turbulent particle transport in streams: Can exponential settling be reconciled with fluid mechanics?, *Journal of Theoretical Biology*, *300*, 62-80.

Meerschaert, M. M., and A. Sikorskii (2012), Stochastic models for fractional calculus, edited, Walter de Gruyter.

Meire, D. W. S. A., J. M. Kondziolka, and H. M. Nepf (2014), Interaction between neighboring vegetation patches: Impact on flow and deposition, *Water Resources Research*, *50*, 3809-3825. doi: 10.1002/2013WR015070.

Mendoza, C., and D. Zhou (1992), Effects of porous bed on turbulent stream flow above bed, *Journal of Hydraulic Engineering*, *118*, 1222-1240.

Mermillod-Blondin, F., R. Rosenberg, F. François-Carcaillet, K. Norling, and L. Mauclaire (2004), Influence of bioturbation by three benthic infaunal species on microbial communities and biogeochemical processes in marine sediment, *Aquatic Microbial Ecology*, *36*, 271-284.

Mermillod-Blondin, F., M. Gérino, V. Degrange, R. Lensi, J.-L. Chassé, M. Rard, and M. C. d. Châtelliers (2001), Testing the functional redundancy of Limnodrilus and Tubifex (Oligochaeta, Tubificidae) in hyporheic sediments: an experimental study in microcosms, *Canadian Journal of Fisheries and Aquatic Sciences*, *58*, 1747-1759. doi: 10.1139/f01-119.

Meter, K. J. V., N. B. Basu, J. J. Veenstra, and C. L. Burras (2016), The nitrogen legacy: emerging evidence of nitrogen accumulation in anthropogenic landscapes, *Environmental Research Letters*, *11*, 035014.

Metzler, R., and J. Klafter (2000), The random walk's guide to anomalous diffusion: a fractional dynamics approach, *Physics reports*, *339*, 1-77.

Meysman, F. J., J. J. Middelburg, and C. H. Heip (2006), Bioturbation: a fresh look at Darwin's last idea, *Trends in Ecology & Evolution*, *21*, 688-695.

Meysman, F. J., B. P. Boudreau, and J. J. Middelburg (2010), When and why does bioturbation lead to diffusive mixing?, *Journal of Marine Research*, *68*, 881-920.

Meysman, F. J., V. S. Malyuga, B. P. Boudreau, and J. J. Middelburg (2008a), A generalized stochastic approach to particle dispersal in soils and sediments, *Geochimica et Cosmochimica Acta*, *72*, 3460-3478.

Meysman, F. J., V. Malyuga, B. P. Boudreau, and J. Middelburg (2008b), Quantifying particle dispersal in aquatic sediments at short time scales: model selection, *Aquatic Biology*, *2*.

Millward, R. N., T. S. Bridges, U. Ghosh, J. R. Zimmerman, and R. G. Luthy (2005), Addition of Activated Carbon to Sediments to Reduce PCB Bioaccumulation by a Polychaete (Neanthes arenaceodentata) and an Amphipod (Leptocheirus plumulosus), *Environmental Science & Technology*, *39*, 2880-2887. doi: 10.1021/es048768x.

Montgomery, D. C., and G. C. Runger (2010), *Applied statistics and probability for engineers*, John Wiley & Sons.

Morales, C. F. L., M. Strathmann, and H.-C. Flemming (2007), Influence of biofilms on the movement of colloids in porous media. Implications for colloid facilitated transport in subsurface environments, *Water Research*, *41*, 2059-2068.

Morgenroth, E., and K. Milferstedt (2009), Biofilm engineering: linking biofilm development at different length and time scales, *Reviews in Environmental Science and Bio/Technology*, *8*, 203-208.

Murray, A. B., M. A. F. Knaapen, M. Tal, and M. L. Kirwan (2008), Biomorphodynamics: Physical-biological feedbacks that shape landscapes, *Water Resources Research*, *44*, W11301. doi: 10.1029/2007WR006410.

Nagaoka, H., and S. Ohgaki (1990), Mass transfer mechanism in a porous riverbed, *Water Research*, *24*, 417-425.

Nepf, H., M. Ghisalberti, B. White, and E. Murphy (2007), Retention time and dispersion associated with submerged aquatic canopies, *Water Resources Research*, *43*, n/a-n/a. doi: 10.1029/2006WR005362.

Newbold, J. D., J. W. Elwood, R. V. Oneill, and W. Vanwinkle (1981), Measuring Nutrient Spiralling in Streams, *Canadian Journal of Fisheries and Aquatic Sciences*, *38*, 860-863.

Newbold, J. D., T. L. Bott, L. A. Kaplan, B. W. Sweeney, and R. L. Vannote (1997), Organic Matter Dynamics in White Clay Creek, Pennsylvania, USA, *Journal of the North American Benthological Society*, *16*, 46-50. doi: 10.2307/1468231.

Newbold, J. D., S. A. Thomas, G. W. Minshall, C. E. Cushing, and T. Georgian (2005), Deposition, benthic residence, and resuspension of fine organic particles in a mountain stream, *Limnology and Oceanography*, *50*, 1571-1580.

Niederdorfer, R., H. Peter, and T. J. Battin (2016), Attached biofilms and suspended aggregates are distinct microbial lifestyles emanating from differing hydraulics, *Nature Microbiology*, *1*, 16178.

Nikora, V. I. (2010), Hydrodynamics of aquatic ecosystems: An interface between ecology, biomechanics and environmental fluid mechanics, *River Research and Applications*, *26*, 367-384.

Nikora, V. I., D. G. Goring, and B. J. F. Biggs (2002), Some observations of the effects of micro-organisms growing on the bed of an open channel on the turbulence properties, *Journal of Fluid Mechanics*, *450*, 317-341.

Nikora, V. I., A. M. Suren, S. L. Brown, and B. J. Biggs (1998), The effects of the moss Fissidens rigidulus (Fissidentaceae: Musci) on near-bed flow structure in an experimental cobble bed flume, *Limnology and Oceanography*, *43*, 1321-1331.

Nikora, V. I., D. Goring, I. McEwan, and G. Griffiths (2001), Spatially averaged open-channel flow over rough bed, *Journal of Hydraulic Engineering*, *127*, 123-133.

Nikora, V. I., I. McEwan, S. McLean, S. Coleman, D. Pokrajac, and R. Walters (2007), Double-Averaging Concept for Rough-Bed Open-Channel and Overland Flows: Theoretical Background, *Journal of Hydraulic Engineering*, *133*, 873-883. doi: doi:10.1061/(ASCE)0733-9429(2007)133:8(873).

Niño, Y., F. Lopez, and M. Garcia (2003), Threshold for particle entrainment into suspension, *Sedimentology*, *50*, 247-263. doi: 10.1046/j.1365-3091.2003.00551.x.

Ninto, Y., and M. H. Garcia (1996), Experiments on particle—turbulence interactions in the near–wall region of an open channel flow: implications for sediment transport, *Journal of Fluid Mechanics*, *326*, 285-319. doi: doi:10.1017/S0022112096008324.

Nogaro, G., F. Mermillod-Blondin, F. FranÇOis- Carcaillet, J.-P. Gaudet, M. Lafont, and J. Gibert (2006), Invertebrate bioturbation can reduce the clogging of sediment: an experimental

study using infiltration sediment columns, *Freshwater Biology*, *51*, 1458-1473. doi: 10.1111/j.1365-2427.2006.01577.x.

O'Connor, B. L., and J. W. Harvey (2008), Scaling hyporheic exchange and its influence on biogeochemical reactions in aquatic ecosystems, *Water Resources Research*, *44*, n/a-n/a.

Okabe, S., T. Yasuda, and Y. Watanabe (1997), Uptake and release of inert fluorescence particles by mixed population biofilms, *Biotechnology and Bioengineering*, *53*, 459-469. doi: 10.1002/(SICI)1097-0290(19970305)53:5<459::AID-BIT3>3.0.CO;2-G.

Okabe, S., H. Kuroda, and Y. Watanabe (1998), Significance of biofilm structure on transport of inert particulates into biofilms, *Water Science and Technology*, *38*, 163-170.

Orr, C. H., J. J. Clark, P. R. Wilcock, J. C. Finlay, and M. W. Doyle (2009), Comparison of morphological and biological control of exchange with transient storage zones in a field-scale flume, *Journal of Geophysical Research: Biogeosciences*, *114*, n/a-n/a.

Packman, A. I. (1999), Scaling bedform-driven exchange between a stream and a finite stream bed, paper presented at 28th International Association for Hydraulic Research Congress, Graz, Austria.

Packman, A. I., and N. H. Brooks (2001), Hyporheic exchange of solutes and colloids with moving bed forms, *Water Resources Research*, *37*, 2591-2605. doi: Doi 10.1029/2001wr000477.

Packman, A. I., M. Salehin, and M. Zaramella (2004), Hyporheic Exchange with Gravel Beds: Basic Hydrodynamic Interactions and Bedform-Induced Advective Flows, *Journal of Hydraulic Engineering*, *130*, 647-656.

Paul, M. J., and R. O. Hall, Jr. (2002), Particle transport and transient storage along a stream-size gradient in the Hubbard Brook Experimental Forest, *Journal of the North American Benthological Society*, *21*, 195-205. doi: doi:10.2307/1468409.

Payn, R. A., M. N. Gooseff, D. A. Benson, O. A. Cirpka, J. P. Zarnetske, W. B. Bowden, J. P. McNamara, and J. H. Bradford (2008), Comparison of instantaneous and constant-rate stream

tracer experiments through non-parametric analysis of residence time distributions, *Water Resources Research*, *44*, n/a-n/a. doi: 10.1029/2007WR006274.

Phipps, G. L., G. T. Ankley, D. A. Benoit, and V. R. Mattson (1993), Use of the aquatic oligochaete Lumbriculus variegatus for assessing the toxicity and bioaccumulation of sediment-associated contaminants, *Environmental Toxicology and Chemistry*, *12*, 269-279.

Piot, A., A. Rochon, G. Stora, and G. Desrosiers (2008), Experimental study on the influence of bioturbation performed by Nephtys caeca (Fabricius) and Nereis virens (Sars) annelidae on the distribution of dinoflagellate cysts in the sediment, *Journal of Experimental Marine Biology and Ecology*, *359*, 92-101. doi: http://dx.doi.org/10.1016/j.jembe.2008.02.023.

Pischedda, L., J.-C. Poggiale, P. Cuny, and F. Gilbert (2008), Imaging oxygen distribution in marine sediments. The importance of bioturbation and sediment heterogeneity, *Acta biotheoretica*, *56*, 123-135.

Pizzuto, J., et al. (2014), Characteristic length scales and time-averaged transport velocities of suspended sediment in the mid-Atlantic Region, USA, *Water Resources Research*, *50*, 790-805. doi: 10.1002/2013WR014485.

Poggi, D., G. Katul, and J. Albertson (2006), Scalar dispersion within a model canopy: Measurements and three-dimensional Lagrangian models, *Advances in Water Resources*, *29*, 326-335. doi: https://doi.org/10.1016/j.advwatres.2004.12.017.

Pokrajac, D., C. Manes, and I. McEwan (2007), Peculiar mean velocity profiles within a porous bed of an open channel, *Physics of Fluids (1994-present)*, *19*, -.

Polyanin, A. D., and V. E. Nazaikinskii (2016), *Handbook of Linear Partial Differential Equations for Engineers and Scientists*, CRC press.

Powell, E. N. (1977), Particle size selection and sediment reworking in a funnel feeder, Leptosynapta tenuis (Holothuroidea, Synaptidae), *Internationale Revue der gesamten Hydrobiologie und Hydrographie*, *62*, 385-408. doi: 10.1002/iroh.1977.3510620305.

Power, M. E., and A. J. Stewart (1987), Disturbance and Recovery of an Algal Assemblage Following Flooding in an Oklahoma Stream, *The American Midland Naturalist*, *117*, 333-345. doi: 10.2307/2425975.

Preisser, E. L., D. I. Bolnick, and M. F. Benard (2005), Scared to Death? The Effects of Intimidation and Consumption in Predator–Prey Interactions, *Ecology*, *86*, 501-509. doi: 10.1890/04-0719.

Quinton, J. N., G. Govers, K. Van Oost, and R. D. Bardgett (2010), The impact of agricultural soil erosion on biogeochemical cycling, *Nature Geosci*, *3*, 311-314. doi: http://www.nature.com/ngeo/journal/v3/n5/suppinfo/ngeo838_S1.html.

R Development Core Team (2009), R: A Language and Environment for Statistical Computing, *R foundation for statistical computing*.

Raymond, P. A., et al. (2013), Global carbon dioxide emissions from inland waters, *Nature*, *503*, 355-359.

Remaili, T. M., S. L. Simpson, E. D. Amato, D. A. Spadaro, C. V. Jarolimek, and D. F. Jolley (2016), The impact of sediment bioturbation by secondary organisms on metal bioavailability, bioaccumulation and toxicity to target organisms in benthic bioassays: Implications for sediment quality assessment, *Environmental Pollution*, *208, Part B*, 590-599. doi: http://dx.doi.org/10.1016/j.envpol.2015.10.033.

Rhoads, D. (1974), Organism-sediment relations on the muddy sea floor. Oceanogr, *Mar. Biol. Ann. Rev.*, *12*, 263-300.

Richardson, C. P., and A. D. Parr (1988), Modified Fickian model for solute uptake by runoff, *Journal of environmental engineering*, *114*, 792-809.

Richardson, D. C., J. D. Newbold, A. K. Aufdenkampe, P. G. Taylor, and L. A. Kaplan (2013), Measuring heterotrophic respiration rates of suspended particulate organic carbon from stream ecosystems, *Limnol. Oceanogr.-Meth*, *11*, 247-261. doi: 10.4319/lom.2013.11.247.

Robbins, J. A. (1986), A model for particle-selective transport of tracers in sediments with conveyor belt deposit feeders, *Journal of Geophysical Research: Oceans (1978--2012)*, *91*, 8542-8558.

Robbins, J. A., P. L. McCall, J. B. Fisher, and J. R. Krezoski (1979), Effect of deposit feeders on migration of137Cs in lake sediments, *Earth and Planetary Science Letters*, *42*, 277-287. doi: http://dx.doi.org/10.1016/0012-821X(79)90035-9.

Roche, K. R., A. F. Aubeneau, M. Xie, T. Aquino, D. Bolster, and A. I. Packman (2016), An Integrated Experimental and Modeling Approach to Predict Sediment Mixing from Benthic Burrowing Behavior, *Environmental Science & Technology*, *50*, 10047-10054.

Rockstrom, J., et al. (2009), A safe operating space for humanity, *Nature*, *461*, 472-475.

Rodríguez-Iturbe, I., and A. Rinaldo (2001), *Fractal river basins: chance and self-organization*, Cambridge University Press.

Rouse, H. (1939), Experiments on the mechanics of sediment suspension.

Ruff, J., and L. Gelhar (1972), Turbulent shear flow in porous boundary, *J. Engrg. Mech*, *504*, 975.

Sardo, A. M., and A. M. V. M. Soares (2010), Can behavioural responses of Lumbriculus variegatus (Oligochaeta) assess sediment toxicity? A case study with sediments exposed to acid mine drainage, *Environmental Pollution*, *158*, 636-640. doi: http://dx.doi.org/10.1016/j.envpol.2009.08.015.

Sauter, G., and H. Güde (1996), Influence of grain size on the distribution of tubificid oligochaete species, *Hydrobiologia*, *334*, 97-101. doi: 10.1007/bf00017358.

Schindelin, J., et al. (2012), Fiji: an open-source platform for biological-image analysis, *Nature methods*, *9*, 676-682.

Schneider, C. A., W. S. Rasband, and K. W. Eliceiri (2012), NIH Image to ImageJ: 25 years of image analysis, *Nat methods*, *9*, 671-675.

Schumer, R., M. M. Meerschaert, and B. Baeumer (2009), Fractional advection-dispersion equations for modeling transport at the Earth surface, *Journal of Geophysical Research: Earth Surface (2003--2012)*, *114*.

Schumer, R., D. A. Benson, M. M. Meerschaert, and B. Baeumer (2003), Fractal mobile/immobile solute transport, *Water Resources Research*, *39*.

Searcy, K. E., A. I. Packman, E. R. Atwill, and T. Harter (2006), Capture and retention of Cryptosporidium parvum oocysts by Pseudomonas aeruginosa biofilms, *Applied and environmental microbiology*, *72*, 6242-6247.

Shimizu, Y., T. Tsujimoto, and H. Nakagawa (1990), Experiment and macroscopic modelling of flow in highly permeable porous medium under free-surface flow, *J. Hydrosci. Hydraul. Eng*, *8*, 69-78.

Simpson, S. L., D. Ward, D. Strom, and D. F. Jolley (2012), Oxidation of acid-volatile sulfide in surface sediments increases the release and toxicity of copper to the benthic amphipod Melita plumulosa, *Chemosphere*, *88*, 953-961.

Singer, G., K. Besemer, P. Schmitt-Kopplin, d. Hö, Iris, and T. J. Battin (2010), Physical heterogeneity increases biofilm resource use and its molecular diversity in stream mesocosms, *PLoS One*, *5*, e9988-e9988.

Smith, M. E., J. M. Lazorchak, L. E. Herrin, S. Brewer‐Swartz, and W. T. Thoeny (1997), A reformulated, reconstituted water for testing the freshwater amphipod, Hyalella azteca, *Environmental Toxicology and Chemistry*, *16*, 1229-1233

Soldati, A., and C. Marchioli (2009), Physics and modelling of turbulent particle deposition and entrainment: Review of a systematic study, *International Journal of Multiphase Flow*, *35*, 827-839.

Spencer, D. R. (1980), The Aquatic Oligochaeta of the St. Lawrence Great Lakes Region, in *Aquatic Oligochaete Biology*, edited by R. O. Brinkhurst and D. G. Cook, pp. 115-164, Springer US, Boston, MA.

Stoesser, T., J. Frohlich, and W. Rodi (2007), Turbulent open-channel flow over a permeable bed, paper presented at Proceedings of the Congress-International Association for Hydraulic Research.

Stonedahl, S. H., J. W. Harvey, A. Worman, M. Salehin, and A. I. Packman (2010), A multiscale model for integrating hyporheic exchange from ripples to meanders, *Water Resources Research*, *46*.

Stonedahl, S. H., J. W. Harvey, J. Detty, A. Aubeneau, and A. I. Packman (2012), Physical controls and predictability of stream hyporheic flow evaluated with a multiscale model, *Water Resources Research*, *W10513*.

Stoodley, P., Z. Lewandowski, J. D. Boyle, and H. M. Lappin-Scott (1999), Structural deformation of bacterial biofilms caused by short-term fluctuations in fluid shear: an in situ investigation of biofilm rheology, *Biotechnology and Bioengineering*, *65*, 83-92.

Stoodley, P., R. Cargo, C. Rupp, S. Wilson, and I. Klapper (2002), Biofilm material properties as related to shear-induced deformation and detachment phenomena, *Journal of Industrial Microbiology and Biotechnology*, *29*, 361-367.

Sund, N., D. Bolster, S. Mattis, and C. Dawson (2015), Pre-asymptotic Transport Upscaling in Inertial and Unsteady Flows Through Porous Media, *Transport in Porous Media*, *109*, 411-432.

Sundelin, B., and A.-K. Eriksson (2001), Mobility and bioavailability of trace metals in sulfidic coastal sediments, *Environmental Toxicology and Chemistry*, *20*, 748-756. doi: 10.1002/etc.5620200408.

Sutherland, I. W. (2001), The biofilm matrix--an immobilized but dynamic microbial environment, *Trends in Microbiology*, *9*, 222-227.

Taherzadeh, D., C. Picioreanu, and H. Horn (2012), Mass transfer enhancement in moving biofilm structures, *Biophysical journal*, *102*, 1483-1492.

Tank, J. L., E. J. Rosi-Marshall, N. A. Griffiths, S. A. Entrekin, and M. L. Stephen (2010), A review of allochthonous organic matter dynamics and metabolism in streams, *Journal of the North American Benthological Society*, *29*, pp. 118-146.

Tennekes, H., and J. L. Lumley (1972), *A first course in turbulence*, MIT press.

Thibodeaux, L. J., and J. Boyle (1987), Bedform-Generated Convective Transport in Bottom Seiment, *Nature*, *325*, 341-343.

Thibodeaux, L. J., and V. J. Bierman (2003), The bioturbation-driven chemical release process, *Environmental Science & Technology*, *37*, 252A-258A.

Thibodeaux, L. J., K. T. Valsaraj, and D. D. Reible (2001), Bioturbation-driven transport of hydrophobic organic contaminants from bed sediment, *Environmental engineering science*, *18*, 215-223.

Thomas, S. A., J. D. Newbold, M. T. Monaghan, G. W. Minshall, T. Georgian, and C. E. Cushing (2001), The influence of particle size on seston deposition in streams, *Limnology and Oceanography*, *46*, 1415-1424.

Thomsen, U., B. Thamdrup, D. A. Stahl, and D. E. Canfield (2004), Pathways of organic carbon oxidation in a deep lacustrine sediment, Lake Michigan, *Limnology and Oceanography*, *49*, 2046-2057.

Timm, T. (1980), Distribution of aquatic oligochaetes, in *Aquatic Oligochaete Biology*, edited, pp. 55-77, Springer.

Tonina, D., and J. M. Buffington (2007), Hyporheic exchange in gravel bed rivers with pool-riffle morphology: Laboratory experiments and three-dimensional modeling, *Water Resources Research*, *43*.

Tonina, D., and J. M. Buffington (2009), Hyporheic exchange in mountain rivers I: Mechanics and environmental effects, *Geography Compass*, *3*, 1063-1086.

Uijttewaal, W., D. Lehmann, and A. v. Mazijk (2001), Exchange Processes between a River and Its Groyne Fields: Model Experiments, *Journal of Hydraulic Engineering*, *127*, 928-936.

Vignaga, E., D. M. Sloan, X. Luo, H. Haynes, V. R. Phoenix, and W. T. Sloan (2013), Erosion of biofilm-bound fluvial sediments, *Nature Geoscience*, *6*, 770-774.

Voermans, J. J., M. Ghisalberti, and G. N. Ivey (2017), The variation of flow and turbulence across the sediment–water interface, *Journal of Fluid Mechanics*, *824*, 413-437. doi: 10.1017/jfm.2017.345.

Volkenborn, N., L. Polerecky, D. Wethey, and S. Woodin (2010), Oscillatory porewater bioadvection in marine sediments induced by hydraulic activities of Arenicola marina, *Limnology and oceanography*, *55*, 1231.

Vollmer, S., F. de los Santos Ramos, H. Daebel, and G. Kühn (2002), Micro scale exchange processes between surface and subsurface water, *Journal of Hydrology*, *269*, 3-10.

Wagner, M., D. Taherzadeh, C. Haisch, and H. Horn (2010), Investigation of the mesoscale structure and volumetric features of biofilms using optical coherence tomography, *Biotechnology and Bioengineering*, *107*, 844-853.

Wahl, T. L. (2000), Analyzing ADV Data Using WinADV, paper presented at Joint Conference on Water Resource Engineering and Water Resources Planning and Management, Minneapolis, MN, USA.

Wehrli, B. (2013), Biogeochemistry: Conduits of the carbon cycle, edited, pp. 346-347.

Weiss, N., T. G. van Leeuwen, and J. Kalkman (2013), Localized measurement of longitudinal and transverse flow velocities in colloidal suspensions using optical coherence tomography, *Physical Review E*, *88*, 042312.

White, B. L., and H. M. Nepf (2007), Shear instability and coherent structures in shallow flow adjacent to a porous layer, *Journal of Fluid Mechanics*, *593*, 1-32.

Workshop, S. S. (1990), Concepts and Methods for Assessing Solute Dynamics in Stream Ecosystems, *Journal of the North American Benthological Society*, *9*, pp. 95-119.

Xi, C., D. Marks, S. Schlachter, W. Luo, and S. A. Boppart (2006), High-resolution three-dimensional imaging of biofilm development using optical coherence tomography, *Journal of biomedical optics*, *11*, 034001-034006.

Xie, M., N. Wang, J.-F. Gaillard, and A. I. Packman (2016), Hydrodynamic Forcing Mobilizes Cu in Low-Permeability Estuarine Sediments, *Environmental Science & Technology*, *50*, 4615-4623. doi: 10.1021/acs.est.5b04576.

Xie, M. W., B. A. Jarrett, C. Da Silva-Cadoux, K. J. Fetters, G. A. Burton, J. F. Gaillard, and A. I. Packman (2015), Coupled Effects of Hydrodynamics and Biogeochemistry on Zn Mobility and Speciation in Highly Contaminated Sediments, *Environmental Science & Technology*, *49*, 5346-5353. doi: 10.1021/acs.est.5b00416.

Xu, L.-C., V. Vadillo-Rodriguez, and B. E. Logan (2005), Residence time, loading force, pH, and ionic strength affect adhesion forces between colloids and biopolymer-coated surfaces, *Langmuir*, *21*, 7491-7500.

Zagni, A. F., and K. V. Smith (1976), Channel flow over permeable beds of graded spheres, *Journal of the Hydraulics Division*, *102*, 207-222.

Zaramella, M., A. I. Packman, and A. Marion (2003), Application of the transient storage model to analyze advective hyporheic exchange with deep and shallow sediment beds, *Water Resources Research*, *39*, n/a-n/a. doi: 10.1029/2002WR001344.

Zarnetske, J. P., R. Haggerty, S. M. Wondzell, and M. A. Baker (2011), Dynamics of nitrate production and removal as a function of residence time in the hyporheic zone, *Journal of Geophysical Research: Biogeosciences (2005--2012)*, *116*.

Zhang, Y., and M. M. Meerschaert (2011), Gaussian setting time for solute transport in fluvial systems, *Water Resources Research*, *47*, n/a-n/a. doi: 10.1029/2010WR010102.

Zhang, Y., M. M. Meerschaert, and A. I. Packman (2012), Linking fluvial bed sediment transport across scales, *Geophysical Research Letters*, *39*, L20404. doi: 10.1029/2012gl053476.

Ziebis, W., S. Forster, M. Huettel, and B. Jørgensen (1996), Complex burrows of the mud shrimp Callianassa truncata and their geochemical impact in the sea bed, *Nature*, *382*, 619-622.

Zippe, H. J., and W. H. Graf (1983), Turbulent boundary-layer flow over permeable and non-permeable rough surfaces, *Journal of Hydraulic Research*, *21*, 51-65. doi: 10.1080/00221688309499450.